Master Thesis Mechanical Engineering

MANUFACTURING AND EVALUATION OF ACTIVATED CARBON ELECTRODES FOR DESALINATION PURPOSES VIA MULTI-CHANNEL CAPACITIVE DEIONIZATION

TU Delft

MANUFACTURING AND EVALUATION OF ACTIVATED CARBON ELECTRODES FOR DESALINATION PURPOSES VIA MULTI-CHANNEL CAPACITIVE DEIONIZATION

by

Wessel Adrianus Oud

to obtain the degree of Master of Science
at the Delft University of Technology,
to be defended publicly on Friday, April 9, 2021 at 10:00 AM.

Student number:	4492056	
Project duration:	February 3, 2020 – April 9, 2021	
Thesis committee:	Dr. N. Boon,	TU Delft, supervisor
	Dr. H. B. Eral,	TU Delft
	Dr. R. M. Hartkamp,	TU Delft
	Dr. L. Botto,	TU Delft
	Prof. dr. ir. J. T. Padding,	TU Delft

An electronic version of this thesis is available at `http://repository.tudelft.nl/`.

TU Delft

Abstract

Water scarcity is an increasing problem around the world due to growing population and more frequent weather extremities. Desalination, the process in which salt water is converted into freshwater, is a sensible option to expand the drinking water supply by accessing the vast salt water resources on Earth. Capacitive deionization (CDI) is a novel desalination technology that is based on separating salt ions from aqueous solutions in an electrical double layer. An electrostatic potential difference is applied between two high surface area electrodes, the two oppositely charged electrodes attract and adsorb salt ions onto the electrode surface, as such producing a purified stream of water. In time, the electrodes become saturated with ions. To regenerate the electrodes the applied potential is removed or reversed, producing a concentrated stream of water.

For brackish water, this new fundamental method of desalination has advantages over conventional desalination technologies. CDI can be operated with minimal energy requirement in ambient pressures and temperatures, delivering easy operable systems. This thesis investigates manufacturing of activated carbon electrodes purposed for multi-channel CDI (MC-CDI). Current CDI systems operate by desalinating one channel and concentrating the same channel periodically. MC-CDI operates a charging scheme, utilizing more than two electrodes, to desalinate one channel into another channel, circumventing the need to separate desalinated water from concentrated water downstream. Due to the different mode of separation are currently available CDI electrodes not tailored to, or not usable at all, in MC-CDI.

In this project six successful different types of electrodes are manufactured by dip coating. The coating compositions applied onto carbon fiber and glass fiber paper support structures are 80:10:10, 70:10:20 and 40:40:20 using activated carbon powder (ACP), carbon black and PVDF binder respectively. The in-house build electrodes are analyzed with cyclic voltammetry, desalination measurements and a surface and pore size analyzer. Two-dimensional electrosorption simulations are performed to explore the effect of electrode resistance, micropore porosity and electrode thickness.

The dip coated electrodes result in permeable smooth uniform electrodes. The ACP used is a typical microporous activated carbon with a specific surface area of 930 m^2/g. The electrodes with the most amount of ACP display largest capacitance and salt adsorption capacity. The best gravimetric performing electrode is the glass fiber paper electrode with high ACP coating, which can be characterized by a capacitance of 31.44 F/g and a salt adsorption capacity (SAC) of 2.8 mg/g. To compare the experimentally determined capacitance and SAC with the literature, the fact that part of the electrodes is covered by a rubber gasket is taken into account, this part is excluded to contribute to the electrosorption process. The active area adjusted capacitance and SAC for the glass fiber paper electrode with high ACP coating result in 49.37 F/g and 4.40 mg/g, and is in line with literature. It is shown that increasing the binder mass in the coating results in mechanically more stable electrodes, at the cost of blocking surface area from ion adsorption. Increasing the amount of carbon black in the electrode increases the electrical conductivity of the coating, at the cost of SAC. The carbon fiber electrodes have superior electrical conductivity compared to the glass fiber electrodes, however, the conductivity of the glass fiber electrodes does not under-perform dramatically and a non-conductive support structure can very well be used in CDI electrodes. The carbon fiber electrodes display more limited MC-CDI functionality, as the carbon fiber structure results in a more dense separation between the channels, potentially resulting in less efficient MC-CDI operation. Electrosorption simulations show that the process takes place in two distinct phases: fast initial micropore charging, followed by slow diffusion-limited uptake of salt from the gap. Increasing the electrode electrical resistance results in an impeding effect on electrosorption. Increasing the micropore porosity results in larger SAC. Thicker electrodes can adsorb more salt, however, the adsorption kinetics are more limited by the increase of the diffusion time scale. From these results, thin highly electrical conductive electrodes with large SAC can be derived to be preferable in MC-CDI operation.

Nomenclature

Abbreviation	Full Form	Abbreviation	Full Form
ACC	Activated Carbon Cloth	H_2	Hydrogen gas
ACF	Activated Carbon Fiber	H_2O_2	Hydrogen Peroxide
ACP	Activated Carbon Powder	H_2O	Water
AEM	Anion Exchange Membrane	i-CDI	Inverted Capacitive Deionization
AM	Active Material	KOH	Potassiom Hydroxide
BET	Brunauer-Emmett-Teller	MCDI	Membrane Capacitive Deionization
CA	Conductive Additive	MC-CDI	Multi-Channel Capacitive Deionization
CB	Carbon black		
CDI	Capacitive Deionization	mD	modified Donnan
CEM	Cation Exchange Membrane	MED	Multi-Effect Distillation
CF	Carbon Fiber	MSF	Multi-Stage Flash Distillation
Cl_2	Chlorine	Na^+	Sodium
Cl^-	Chloride	NaCl	Sodium Chloride
CNT	Carbon Nanotubes	O_2	Oxygen
MWCNT	Multi-walled Carbon Nanotubes	OH^-	Hydroxide
CO_2	Carbon Dioxide	-OH	Hydroxyl
CV	Cyclic Voltammetry	OMC	Ordered Mesoporous Carbon
DSS	Dynamic Steady State	PTFE	Polytetrafluoroethylene
ED	Electrodialysis	PVA	Polyvinyl Alcohol
EDL	Electrical Double Layer	PVDF	Polyvinylidene Fluoride
EIS	Electrochemical Impedance Spectroscopy	RO	Reverse Osmosis
fb-CDI	Flow-By Capacitive Deionization	SAM	Salt Adsorption Measurement
ft-CDI	Flow-Through Capacitive Deionization	SHE	Standard Hydrogen Electrode
Fe^{3+}	Iron (III)	TDS	Total Dissolved Solids
GCS	Gouy-Chapman-Stern	TOC	Total Organic Content
GF	Glass Fiber	WCF	Wood Carbon Framework
H^+	Hydrogen	WR	Water Recovery

Symbol	Definition	Unit
$\phi(x)$	Potential profile	V
λ_D	Debye length	nm
e	Euler's number	-
λ_B	Bjerrum length	nm
c_s	Concentration	$\frac{\text{particles}}{m^3}$
N_A	Avogadro's number	$\frac{\text{particles}}{\text{mol}}$
M	Molarity	$\frac{\text{mol}}{L}$
k	Boltzmann constant	$\frac{m^2 kg}{s^2 K}$
T	Temperature	K
$c_{m,i}$	Micropore concentration species i	mM
$c_{M,i}$	Macropore concentration species i	mM
z_i	Valence species i	-
ϕ_D	Donnan potential	V
V_T	Thermal voltage	V
$\overline{\mu}_{att,i}$	Nonelectrostatic adsorption potential	V
q_m	Micropore charge density	$\frac{C}{m^3}$
F	Faraday constant	$\frac{C}{\text{mol}}$
C_m	Effective specific capacitance of micropores	$\frac{F}{m^3}$
ϕ_m	Micropore potential	V
L_e	Electrode thickness	mm
L_s	Gap thickness	mm
L	Electrode length	mm
W	Electrode width	mm
I_{ext}	External current	A
V_{ext}	External potential	V
R_c	Resistive element	Ω
$\mathbf{u}$	Flow velocity field	$\frac{m}{s}$
c	Concentration	mM
p_m	Micropore porosity	-
p_M	Macropore porosity	-
D_i	Diffusion coefficient species i	$\frac{m^2}{s}$
D_e	Diffusion coefficient within electrode species i	$\frac{m^2}{s}$
$\mathbf{u}_{sup}$	Bulk flow velocity	$\frac{m}{s}$
w_m	Concentration in micropores	mM
ϕ_e	Electrode potential	V
$\mathbf{i}$	Macropore ionic current	A
Pe_e	Electrode Péclet number	-
h_{max}	Maximum film thickness	mm
r	Particle radius	m
G	Shear modulus	Pa
V_d	Volume diluted water	L
V_c	Volume concentrated water	L
Δt_d	Time interval in which the diluted water is collected	s
Δt_c	Time interval in which the concentrated water is collected	s
Q	Volumetric flow rate	$\frac{\text{mL}}{\text{min}}$
$\langle \Delta c \rangle$	Concentration reduction	mM
ΔN_d	Salt removed over one cycle	mol
ΔN_c	Salt added to the concentrate stream over one cycle	mol
c_{feed}	Feed concentration	mM
c_{out}	Effluent concentration	mM
E_v	Volumetric energy consumption	J/L
E_{in}	Energy input	J

Continued on next page

continued from previous page

Symbol	Definition	Unit
E_{out}	Energy output	J
I	Current	A
U	Applied voltage	V
Δt_{cycle}	Total DSS cycle time	s
P	Productivity	$\frac{L}{cm^2 h}$
E_{molar}	Molar energy consumption	$\frac{J}{\text{mol}}$
M_w	Molar mass of the salt	$\frac{g}{\text{mol}}$
m	Total mass of the electrodes	g
C	Capacitance	F
Λ_{cycle}	Charge efficiency	%
η_{coul}	Coulombic efficiency	%
q_{in}	Charge transferred at positive current	C
q_{out}	Charge transferred at negative current	C
R_s	Series resistance	Ω
R_{EER}	External electronic resistance	Ω
R_{sp}	Separator resistance	Ω
l_{sp}	Separator thickness	μm
τ_{sp}	Separator tortuosity	-
κ	Electrolyte conductivity	$\frac{mS}{cm}$
p_{sp}	Separator porosity	-
E_0	Shorting potential	V
E_{PZC}	Potential of zero charge	V
E^0	Redox potential	V
R_{el}	Ionic electrode resistance	Ω
ν	Cyclic voltammery voltage sweeprate	$\frac{mV}{s}$
A_{curve}	Area enclosed by cyclic voltammetry curve	W
U_1	Switching potential 1	V
U_2	Switching potential 2	V
$Area_p$	Area electrode that actively takes part in electrosorption process	cm^2
$Mass_c$	Mass of the electrode excluding the weight of the support structure	g
R_p	Parallel resistance in the Randles cell	Ω
$t_{1/2}$	Half-life time	s
c_0	Influent salt concentration	mM
U	Mean flow velocity	$\frac{m}{s}$

Contents

List of Tables

List of Figures

1 Introduction

Our planet, the 'Blue Planet', is covered for 71% with water [32]. Water is vital for all life on the planet. Unfortunately, even with all this water, more than 40% of the global population is affected by water scarcity [60]. How did we end up here?

To understand how water scarcity arises, it is important to note that only 2.5% of all water is fresh water. Considering most of that is stored as glaciers or deep groundwater, only a small portion is readily available for use. Water is a naturally circulating resource that is constantly recharged via global hydro-logical cycles powered by solar energy. Climate change is expected to accelerate water cycles and increase the available renewable freshwater resources. In contradiction, changes in seasonal patterns and increasing probability of extreme events may cause increasing spatial-temporal water scarcity [48].

To keep up with the increasing demand of a growing population and the varying effects of climate change society needs to adapt to avoid crippling water shortages. Even well developed countries like the USA and the Netherlands face challenges in providing clean fresh water to all of its regions. Future predictions show water stress will increase notably in central and southwest America [8] and earlier this year (2020) a prolonged period of drought within the Netherlands raised caution with the usage of available water [47]. However, in developing countries, like India, the increasing water scarcity is more problematic. In India groundwater makes up 40% of the supply and 21 Indian cities are expected to run out of groundwater by the end of this year. All while other water sources are depleting likewise, almost two-thirds of India's reservoirs are running below normal water levels [66].

Better water management should be in place to maintain or even increase the supply of safe accessible water. From an engineering perspective water scarcity is rather uncomplicated, techniques to treat water have been around for thousands of years. However, high-energy-demanding conventional technologies are often unsustainable and lose approval in a time of climate change and growing population. As most of earths bodies of water are saline, new improved desalination technology can help increase access to clean drinking water. This master thesis research is conducted into low-energy-demanding desalination technology, capacitive deionization (CDI). Activated carbon electrodes are build in-house with the aim to tailor the electrodes to a novel method of CDI operation.

1.1. Processing Water

The great majority of evident water-related health problems are the result of microbial contamination. Besides, an appreciable number of serious health concerns may occur as a result of the chemical contamination of drinking water [65]. Increasing population plus the growing complexity of municipal, agricultural and industrial activity originated the need for a systematic approach for treating water. To provide safe and accessible drinking water, water treatment methods have been applied since ancient times [17]. Means of treating water have improved to keep up with increasing drinking water quality standards. Drinking water today must meet criteria of microbial, radiological, inorganic and organic chemical aspects, and must be acceptable in terms of taste, odor and appearance.

Nowadays, a conventional water treatment process consists of screening, coagulation, flocculation, aeration, sedimentation, filtration and disinfection, as can be seen in Figure 1.1. Dependent on the source water quality additional treatment stages may need to be included. These additional stages can be pH adjustment,

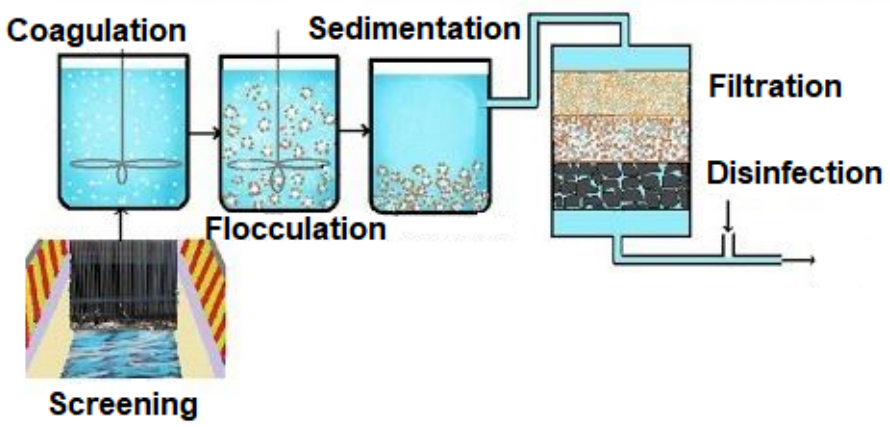

Figure 1.1: Five of the seven main steps taken in a conventional water processing plant. The steps left out are the screening of the intake and the aeration process after sedimentation.

membrane processes or adsorption processes [17]. As 97.5% of all water resources remain as salt or brackish water, it is desalination that provides a means for utilizing this vast water source. Desalination is the process of separating minerals and salts from saline water, producing water that can safely be used after conventional processing.

1.2. Current State of Desalination

Sea and brackish water are typically desalinated using two general types of water treatment technologies. The most common technology applied in desalination systems around the world is reverse osmosis (RO) membrane separation. The second technology used for desalination is thermal evaporation (distillation). In reverse osmosis desalination, fresh water is produced from saline source water by pressure-driven transport of water through semi-permeable membranes. The main driving force in RO desalination is pressure, which is needed to overcome the naturally occurring osmotic pressure. In thermal evaporation, fresh water is separated from the saline source by evaporation, utilizing heat as the driving force.

Next to thermal evaporation and RO membrane separation, two other mainstream technologies that are in use at present are electrodialysis (ED) and ion-exchange (IX). ED is electrically driven desalination in which salt ions are moved out of the source water through exposure to direct electric current. IX is the selective removal of salt ions from the water by adsorption onto ion-selective resin media. The driving force in this process is the ion charge of the IX resin, which can selectively attract and retain ions of the opposite charge contained in the saline source water. RO is most widely applied and can be found in 60% of the world's desalination plants. Thermal desalination facilities take up 34% of all facilities, 75% of these facilities are located in the Arabian Peninsula. There, they use the most saline bodies of water on the planet, making thermal evaporation a viable technology. ED and IX are only applied in a small number of plants [61]. Globally, RO and multi-stage flash distillation treat the same amount of volume [4].

Table 1.1: Desalination process applicability adopted from Desalination Engineering, Planning and Design [61].

Separation Process	**Range of Source Water TDS Concentration for Cost-Effective Application, $\frac{mg}{L}$**
Distillation	20,000 - 100,000
Reverse Osmosis Separation	50 - 46,000
Electrodialysis	200 - 3000
Ion Exchange	1 - 800

Table 1.1 shows a general indication of the range of source water salinity for which technology can be applied cost effectively for desalination. The salt content of water is usually measured by the water quality parameter total dissolved solids (TDS), in units of $\frac{mg}{L}$. The standard for safe drinking water only allows for

500 $\frac{mg}{L}$ TDS. Brackish water is classified as water with TDS between 500 and 15,000 $\frac{mg}{L}$. Water with TDS of 15,000 $\frac{mg}{L}$ or higher is generally referred to as seawater. For CDI brackish water seems most applicable, as the electrodes have a finite ion capacity and the applied voltage potential is limited, CDI can only deliver relatively small TDS reduction each step [7].

Conventional desalination technologies process the total source water feed, i.e, all water has to be transported through a membrane, or through a vapor phase. This ensures the desalination process to be highly energy-intensive. The three major thermal evaporation technologies in use are multi-stage flash distillation (MSF), multi-effect distillation (MED) and vaper compression (VC). These technologies require an energy input of 5.7 $\frac{kWh}{m^3}$ in the most favorable scenario up to a total of 15 $\frac{kWh}{m^3}$. The energy use for RO membrane separation ranges from 0.3 to 4.0 $\frac{kWh}{m^3}$, the high energy consumption of these technologies can be dedicated to the high temperatures and pressures needed to operate the processes.

In 1960 a novel process for desalination was first investigated. Utilizing electrostatic forces to separate salts directly from the saline feed, instead of treating whole feed streams. This fundamental difference could allow for immense advantages in energy usage. Yet, as little was known about the fundamentals of this process at the time, it did not gain much attention. This process, which remained poorly understood at the time, would later become known as capacitive deionization (CDI). However, in times of need for technological advancement, this technology has resurfaced in the field of scientific research. CDI offers a positive perspective on low-cost desalination and can be a part of the water management structure in the future.

1.3. Capacitive Deionization as an Alternative Desalination Technology

CDI is currently an emerging technology that is based on capturing charged ionic species from aqueous solutions in an electrical double layer (EDL), and is being widely explored for water desalination applications. In a typical CDI cell two electrodes are positioned opposite to each other, spaced by a non-conductive mesh. The aqueous solution is allowed to flow between the electrodes through the spacer. During operation a potential difference is applied between the electrodes and the solution is pumped through the cell. The oppositely charged electrodes capture the salt ions in the EDL formed in the electrodes, this process is called electrosorption. As the electrodes adsorbs more and more ions over time, the EDL reaches equilibrium and the electrodes become saturated, capturing a certain amount of ions in the EDL. Saturated electrodes can be replaced or regenerated. Regenerating the electrodes can be achieved by removing the applied potential, i.e, short-circuiting, or a reverse charge can be applied to repel the captured ions. Ions are adsorped during charging of the CDI cell and desorbed during discharge, by correctly phasing these steps the cell can generate a purified and concentrated effluent [2, 4, 30, 53, 58]. A graphical overview of CDI operation is shown in Figure 1.2, along with a magnified part of the electrode material displaying a porous material structure and EDL formation.

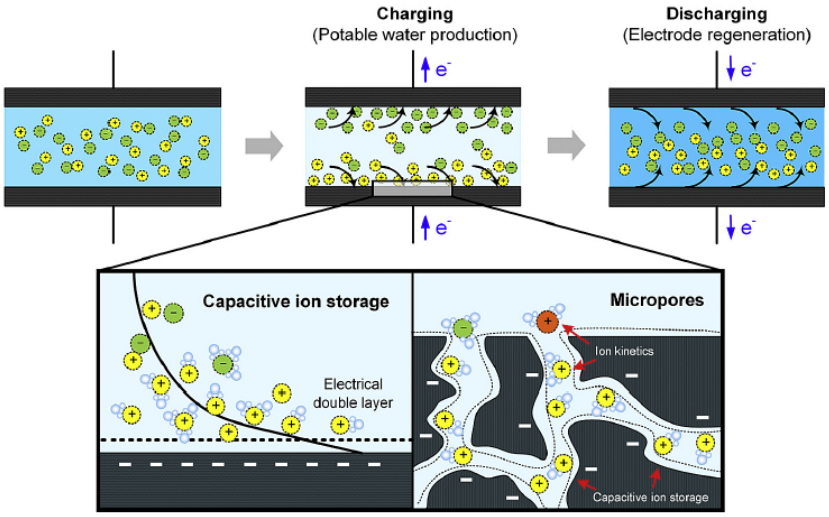

Figure 1.2: Overview of CDI operation and non-faradaic capacitive processes in CDI, adopted from Zhang *et al.* [68]. The top left picture displays two electrodes enclosing a concentrated stream of positive and negative ions. During charging the ions are adsorbed onto the electrodes. During discharging the ions are released back in the gap. The magnified part of the electrode surface depicts the EDL formed (left) and the porous structure of the carbon electrode (right).

As a salt ion removal technology, the working principle of CDI provides three unique advantages. Firstly, CDI operates at low pressures and room temperatures, which is energetically favorable. Moreover, the applied voltage difference is low and the magnitude of the electrical current is dependent on the system size. All in all a working CDI system is easy operable with minimal energy input requirement. Second, in CDI the few salt ions are directly separated out of the feed water. This can allow for potentially higher energy efficient desalination of low salinity source waters, such as brackish water. Thirdly, the CDI cell operates with many features like an electrochemical supercapacitor, the CDI cell has the ability to store energy during charging and the option to recover some of this energy when discharging [58].

The EDL is formed due to electrosorption at the interface between the electrode and electrolyte. The electrode is the solid part of the CDI cell that stores the electrodes and the electrolyte is the solution that contains ions. The interface between electrode and electrolyte can be very large for electrode materials with a high number of micropores, exceeding 1000 $\frac{m^2}{g}$. Across the interface charge separation occurs, with excess charge in one phase and locally charge-compensated by charge in the other phase. These two layers summed result in zero charge with electronic charge in the electrode is locally compensated by opposite ionic charge in the aqueous phase. The most simple EDL model is the Helmholtz model, in this model ions with opposite charge are adsorbed onto the electrode surface and condensed into one dense uniform layer onto the surface of the electrode, which enables the electrodes to store large charge densities at relatively low voltages, see Figure 1.3.

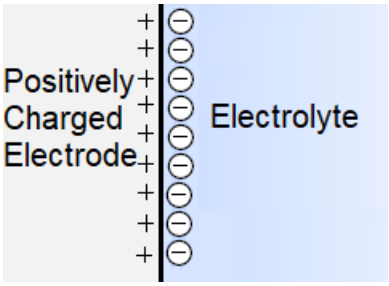

Figure 1.3: The Helmholtz model for describing the EDL.

In practice, the Helmholtz-model does not describe the electrosorption mechanics sufficiently enough and more complex models need to be incorporated [53]. Nonetheless, it yields important introductionary insight into the relation between electrosorption capacity and surface area. More area means more capacity for ion storage. Consequently, the quality of CDI operation depends greatly on microscopic material structure. Ideal electrode properties are recognized from the working principle and EDL model. Accordingly, the electrode material should be of large specific surface area, have high electrical conductivity, good wettability, be mechanically stable and of low cost [30].

Carbon based electrodes contain many of the proposed ideal properties and so exhibit excellent CDI performance. The application of porous carbon electrodes for water desalination was first investigated back in 1960. At that time little was know about the working principle of CDI as the theory of the EDL was only first formulated in 1970. After the breakthrough of the EDL theory the majority of research on porous carbon electrodes became dedicated to capacitive energy strorage applications, and CDI got overlooked. Research into porous carbon electrodes for CDI application started to gain more traction as new carbon materials were developed. In 1995 carbon aerogel was first applied, followed by multiwall carbon nanotubes in 2005.

For CDI to be competitive, CDI must compare favourably with the conventional desalination technologies both in terms of capital and operational costs. As more than 90% of desalination plants apply RO and MSF methods, CDI will be compared to these technologies. Furthermore, ED should be compared to CDI. While ED is a membrane process like RO, the driving force is an applied potential between two electrodes, just like CDI.

The minimum energy required to separate ions from a solution is around 1.1 $\frac{kWh}{m^3}$ for seawater and 0.12 $\frac{kWh}{m^3}$ for brackish water [56]. Do note that these values depend on water recovery and input-output flow concentration ratio. As stated before RO is more cost effective than MSF desalinating seawater, 2.9-3.7 vs. 4.0 $\frac{kWh}{m^3}$. The energy use of 4.0 $\frac{kWh}{m^3}$ for MSF is only true in case MSF is cited with a working power plant to reduce the heat required to drive the distillation process [4]. In 2013 a portable prototype CDI unit was used to desalinate inland brackish water. This unit treated at its highest energy efficiency 7 $\frac{L}{min}$ at an energy

consumption of 1.89 $\frac{kWh}{m^3}$ with a recovery rate between 75% and 80% [45]. CDI has the ability to achieve high water recovery, up to 90%, while RO normally has a recovery rate of 50% or less [64]. ED operation resembles very closely to that of CDI and is already commercially accepted for water treatment. The transport phenomena in ED and CDI are very similar and in both technologies anion and cation membranes can or are incorporated. These membranes contribute to a high cost for ED. In case CDI is able to preform adequately without membranes it can sure be competitive with respect to ED.

At this day, with the increasing need for efficient desalination technologies, and many other promising finds in the field of CDI, research into CDI has picked up momentum and several companies have started marketing commercial CDI technologies. Companies that someway or another have survived for more than a couple of years are ecoEWP, Atlantis Technologies and Voltea, all operating from the USA [53, 64]. Voltea claims their CapDI© technology delivers tunable salt removal (25%-90%) at less than 0.5 $\frac{kWh}{m^3}$, with low/no chemical costs and up to 90% water recovery. EcoEWP is adapting CDI technology to Indian water conditions and started site testing in 2016. EcoEWP supplies purifiers able to desalinate 1 mg/L at 80% water recovery rate. Atlantis Technologies provides radial deionization (RDI^{TM}) technology able to desalinate up to 100 mg/L at a water recovery of 95%. These products usually provide relatively low through put.

As these products are being brought to market there remains much to be investigated in the field of CDI. To increase and further the implementation of CDI technology into industry the robustness of CDI technology to various source water qualities needs to be increased and the behavior over time needs to be detailed and enhanced. To enlarge industrial implementation the design and operation of CDI systems need to be better understood and elaborated upon.

1.4. Research Objectives

Current research at the Technical University Delft is focused on developing a novel CDI design and operation, multi-channel capacitive deionization (MC-CDI). This new design incorporates more than two electrodes in one CDI cell. This way more than one channel is configurated in one cell. The idea behind the novel design is to develop a continuous operating CDI unit without the need to redirect effluent streams during operation in order to separate product form concentrate within the effluent, but instead utilizing the change in potential distribution of the electrodes to allow for ion transport between the different channels, see Figure 1.4. In the first transition step (**1**) of the MC-CDI cell the electrodes enclosing the concentrated stream are being charged. In the second transition (**2**) the middle electrode is being shorted as the top electrode is being charged. As the middle electrode is reaching zero potential the electrode is reversely polarized while the bottom electrode is being shorted or reversely being polarized as well in order to move the adsorbed species towards the middle electrode. In the third transition (**3**) the electrodes are shorted and so releasing the ions. As every other method of CDI operation functions using only one channel many developed electrodes are build using metal foil. In MC-CDI the electrodes need to be able to permeate water as the salt ions diffuse through the water. To allow for MC-CDI to operate optimally in the future the electrodes need to be tailored to MC-CDI needs. In this thesis electrodes are build in-house with the aim to tailor them to MC-CDI operation. Literature is reviewed to gain understanding of the present CDI modes of operation, how CDI performance is measured, how this performance analysis relates to ideal properties for the electrode and how this information can be transformed into a MC-CDI electrode. Furthermore, simulations are completed to help interpret what and how parameters affect CDI performance.

Three research objectives are formulated in the aim of improving multi-channel capacitive deionization functioning.

1. Manufacture an electrode for multi-channel capacitive deionization purposes, able to capture and release ions; while in the process of releasing ions, the ions should be able to permeate the electrode fully with minimal water cross-over.

2. Evaluate the performance of the in-house build electrode in standard flow-by CDI and demonstrate functionality in multi-channel capacitive deionization, using synthetic NaCl solution.

3. Model electrosorption in 2D to explore parameter changes of electrode properties on desalination performance.

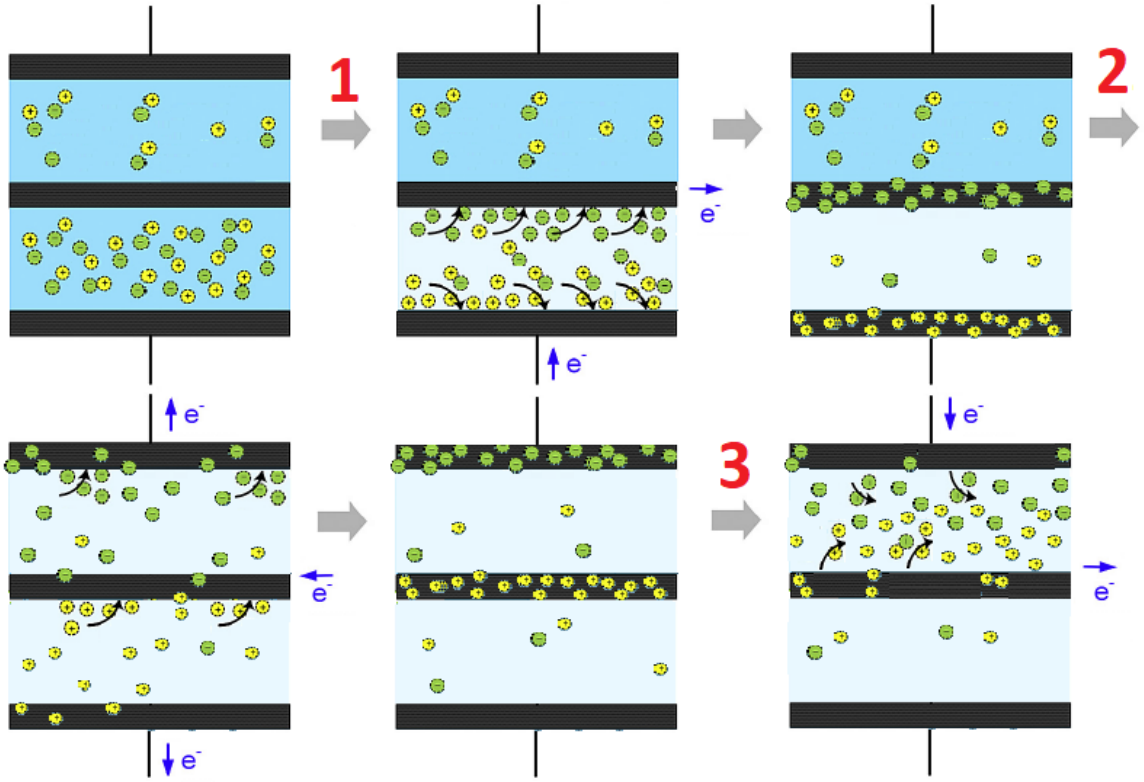

Figure 1.4: Overview of MC-CDI operation. Top left depicts three electrodes enclosing two channels, the channels are diluted and concentrated according to the amount of ions. In the first transition (1) the bottom two electrodes are charged until saturation. The second transition (2) shows the charging of the top electrode as at the same time the middle electrode releases its ion content. This causes for the ions to be moved to the upper electrode. As the middle electrode approaches short-circuit potential it is reversely charged, meanwhile the bottom electrode is reversely polarized. This drives the ions toward the middle electrode. In the third transition (3) the top two electrodes are shorted and the ions are released in the top channel.

2

Literature Review

To complete the research objectives appropriately, the scientific literature is reviewed and compiled into a solid methodology. The structure of the review starts with reiterating the process of CDI. From the process the performance metrics and performance indicators for the CDI process are formulated. In the third section several relevant parameters involving CDI are elaborated upon. From the performance metrics and indicators in combination with the relevant parameters the ideal electrode properties, electrode materials and electrode manufacturing are discussed. In Section 2.6 apparent degradation of CDI performance is briefly mentioned. The literature review is concluded with modelling electrosorption.

2.1. Process of Capacitive Deionization

In CDI processes an electric field is used to separate ions from the solution. The electric field is generated by an electrostatic potential difference between two oppositely charged electrodes, inducing an electrochemical potential gradient that drives the ions towards the electrodes [2, 4, 30, 53, 58]. Cations are driven towards the cathode and the anions towards the anode. One electrode is charged positively, thus adsorbing anions, and one electrode is charged negatively, thus adsorbing cations. The electric charge and the adsorbed ions together form the EDL. In time, the EDL grows, adsorbing more and more ions until the electrodes become saturated. The saturated electrodes can be regenerated by removing the applied potential. Regeneration of the electrodes is the release of adsorbed ions such that a new adsorption phase can follow. During regeneration it is possible to exploit the capacitor-like features of the CDI system, and so recover a large part of the invested energy.

There are three fundamental mechanisms for compensating electric charge: co-ion expulsion, ion swapping and counterion adsorption, see Figure 2.1. Upon increasing electric charge in the electrode can be compensated by co-ion expulsion, ions of the same charge as the electrode are repelled from the electrode surface. Co-ion expulsion can also be accompanied by the adsorption of a counterion, this is then called ion-swapping. As soon as all co-ions are removed from the surface the process of counterion adsorption starts. Here, all increased electrode charge is compensated by the adsorption of counterions. It is the mechanism of counterion adsorption that is sought after in CDI operation [58].

The electric charge in the electrode can be introduced via constant current or constant voltage operation, respectively keeping the applied potential or current constant. It has been shown that the advantage in energy or kinetic efficiency of one charging mode over that of the other is relatively small in most situations [62]. The benefit of constant current over constant voltage is that a steady effluent concentration can be maintained and a minimal over potential is realized, minimizing Faradaic reaction losses. Constant voltage provides the fastest kinetics in CDI operation.

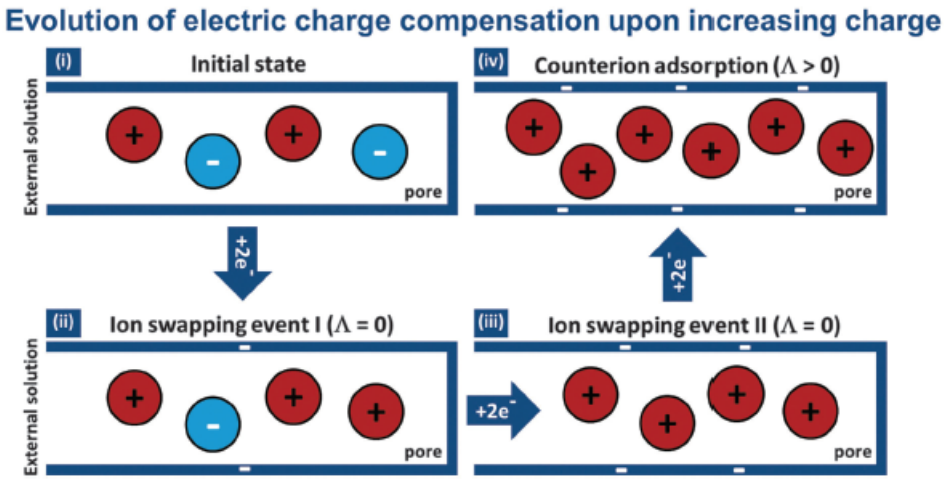

Figure 2.1: The evolution of electric charge compensation upon increasing electrode charge, where two subsequent ion swapping events (ii) and (iii) are followed by counterion adsorption (iv). Adopted from Suss *et al.* [58]

Electrosorption enables salt removal at low pressures and room temperatures, with the primary input being a small cell voltage and an electric current whose magnitude is dependent on the system size. Operating a CDI unit is thus relatively easy. Adsorbing the ions out of the feed directly, instead of treating the total body of water to desalinate the feed, and the possibility of recovering the invested energy during charging in the discharging step, make the energy requirement for CDI minimal. The minimal amount of energy input does, however, make energy losses significant in relation to the thermodynamic efficiency. The thermodynamic efficiency of current experimental CDI systems is currently very low, around 1% for most existing systems [25].

Alternating between charge and discharge phases enables batch wise separation. In recent years different CDI cell architectures have been developed providing unique features and functionality to CDI operation. Architectures that manifested in the field are flow-by and flow-through CDI, membrane CDI, flow-electrode CDI and inverted CDI, see Figure 2.2.

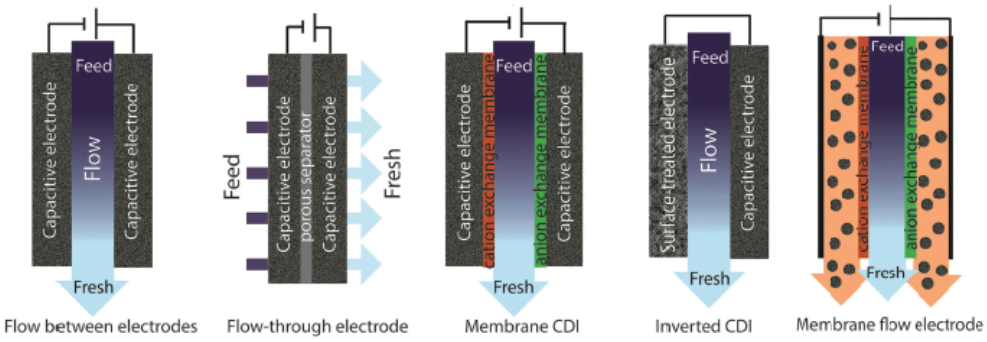

Figure 2.2: Overview of manifested CDI architectures, adopted from Suss *et al.* [58]

2.1.1. Flow-by and Flow-through Capacitive Deionization

The first and most used cell architecture is flow-by CDI (fb-CDI). Here the feed flow is directed between the electrodes perpendicular to the applied electric field. In flow-through CDI (ft-CDI), on the other hand, the feed flow is directed parallel with the applied electric field. It was noted that the ft-CDI architecture allows for faster charging times compared to fb-CDI. Operating in ft-CDI mode also eliminates the need for relative large spacing between the electrodes, as the spacer does not function as the feed flow channel anymore. Thus, the spacing between electrodes can be reduced from 200-500 μm to 10 μm [58]. The reduced spacing can allow for more compact systems with lower ionic resistance and potential faster desalination as the redirected flow reduced the diffusion time scale governing ion removal from between the electrodes. However, in ft-

CDI different components, like oxygen for instance, are forced through the electrodes at higher rates than compared to fb-CDI. This ensures for increased degradation over time.

2.1.2. Membrane Capacitive Deionization

The most used major adaptation of the basic architecture of two electrodes spaced by a separator material occurred with the development of membrane CDI (MCDI). MCDI utilizes ion-exchange membranes positioned between the electrode and spacer. An anion-exchange membrane (AEM) covers the anode and the cathode is shielded by a cation-exchange membrane (CEM). The most important benefit of the added membranes is the increase in charge efficiency [40], which is a parameter we will discuss later. The membranes prevent co-ion expulsion and ion swapping and so increase the ion capacity in electrode macropores. Another benefit of MCDI is the possibility to tailor the membranes to be selective for specific ions of the same charge sign, such that CDI can gain tunability and potentially be more robust with complex multi-ion systems.

2.1.3. Flow-Electrode Capacitive Deionization

The regeneration of the electrodes can be done in two ways, i.e., removing or reversing the applied electric potential or replacing the electrode as a whole. The latter originated the idea to implement Flow-Electrode CDI (FCDI). In FCDI the static electrode is replaced by a slurry of electrode material that can be pumped through the CDI cell, effectively replacing electrode material that has become saturated within the cell [58]. Using this architecture CDI can be continuously operated, as the regeneration of the electrode material can be completed in a separate system. As the electrode material is continuously replenished it increases the capacitance available for desalination as compared to static electrodes. This second advantage yields that FCDI can be used to desalinate higher salinity feeds.

2.1.4. Inverted Capacitive Deionization

Inverted CDI (i-CDI) utilizes electrodes with inherent charge, this permanent charge is manufactured via a chemical surface treatment. When operating i-CDI the behavior is exactly opposite from normal CDI operation, during *charging* of the cell ions are desorbed and the ions are adsorbed during *discharging*. The main advantage of i-CDI is the improved lifetime stability of CDI operation [58].

2.2. Modelling Electrosorption

Modelling can offer a deeper understanding of CDI. There have been several simulating studies in this respect with various levels of complexity. As the current project aims on advancing MC-CDI systems the model should enable the aforementioned charge transport mechanisms in systems with three or more electrodes.

2.2.1. Electical Double Layer Theory

Electrosorption is the process of ion adsorption and charge storage within the EDL. There have been multiple models developed to model this EDL. The first EDL model was developed by Helmholtz, who stated that all surface charge was directly charge-compensated by countercharge adsorbed in one dense layer on the electrode surface. If the Helmholtz model would hold, this would be the ideal situation for CDI operation. As for every electron transfer, two salt ions would be adsorbed, and the charge efficiency would be unity. Experiments showed, however, that charge efficiency is never unity and an improved EDL model was needed.

A new model stated that instead of dense layer adsorption, the ions would adsorb in a diffusely distributed layer close to the surface. This layer is called the Gouy-Chapman layer. Soon after Gouy and Chapman, Stern would add the charge-less, closest approach layer for the ions, updating the model into the well know Gouy-Chapman-Stern model (GCS). The EDL according to GCS can be seen in Figure 2.3. The carbon matrix holds all electric charge and from the surface the potential starts to drop. The stern plane indicates the closest approach for the ionic charge. This distance is kept by finite ion size and hydration shells. The potential has dropped already considerably as it crosses this plane. At the stern plane the ion concentration manifests itself according to the potential profile ($\phi(x)$).

In the GSC model the Debye length λ_D is a characteristic distance for the ion concentration and electrostatic potential to decay by a factor of e [53]. The Debye lenght for a symmetric monovalent electrolyte is defined as

$$\lambda_D = \frac{1}{\sqrt{8\pi\lambda_B c_s}}, \tag{2.1}$$

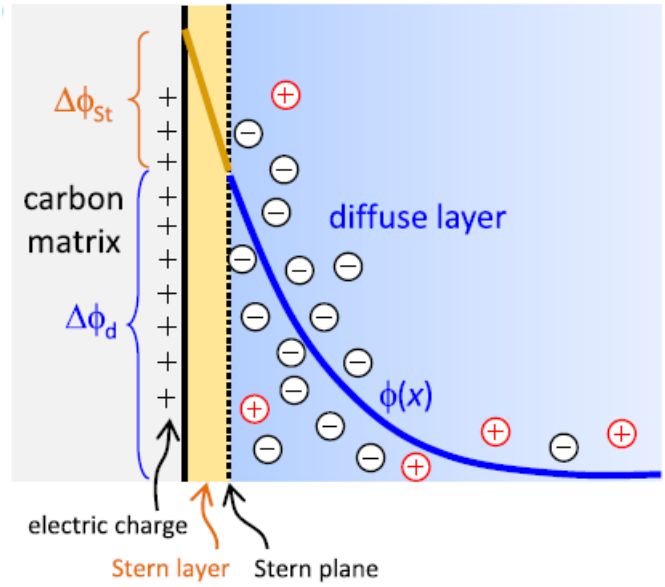

Figure 2.3: Stucture of the EDL according to the Gouy-Chapman-Stern theory for a single planar EDL. Adopted from Porada *et al.* [53].

where N_A is Avogadro's number, λ_B is the Bjerrum length and c_s is the electrolyte concentation in particles per volume. The Bjerrum length in water at room temperature is ≈ 0.7 nm and c_s can be calculated as $1000MN_A$, with M the molarity. The Bjerrum length is the separation at which the electrostatic interaction between two elementary charges is comparable in magnitude to the thermal energy scale kT.

As a rule of thumb, it can be considered that the diffuse layer ends after two to three times the Debye length. For a NaCl solution of 10 mM at $20°C$, the Debye length is approximately 3.1 nm [53]. This indicates that in the micropores of activated carbon (< 2 nm) the EDLs overlap, the situation of overlapping EDLs is not taken into account for the GCS model. In this area the modified Donnan model (mD) is applied. The mD-approach is valid in the limit of strongly overlapped EDLs, and was shown to work well to describe many data sets for salt adsorption and charge storage in CDI. The math of the mD model is detailed as part of the 2D CDI model in the next section. In short, the pores with a small diameter start to act as a potential well, which is more effective in capturing ions compared to a simple surface, i.e. the pore volume is utilized rather than only the surface, see Figure 2.4.

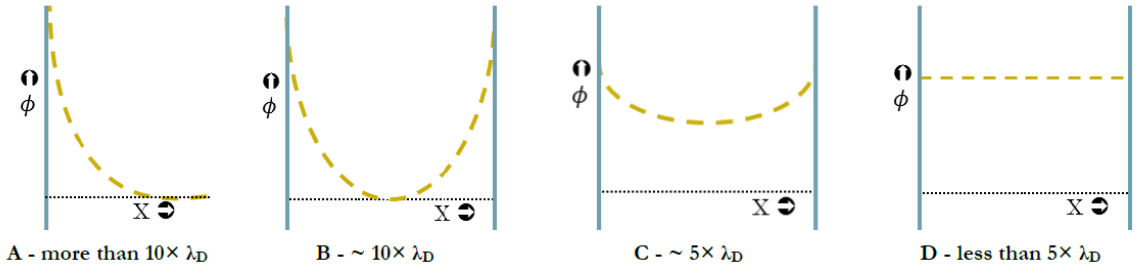

Figure 2.4: Effect of overlapping EDLs on the potential profile. The four sketches show the effect of decreasing distance between two surfaces. Analogous to the shape and behaviour or the potential profile is the concentration profile. Adopted from Boktor [6].

2.2.2. 2D Porous Electrode Model

The first theoretical study that solves coupled axial and transverse transports was developed by Hemmatifar *et al.*[24]. Their model considers coupled mass transport, ionic and electronic transport, including an external, purely resistive parasitic resistance. The model includes three free parameters. The first is a non-electrostatic adsorption parameter which captures experimentally observed adsorption of salt in the absence of external voltage. The second is a lumped parameter which captures volumetric ionic charge capacitance of the electrodes. The third is the micropore porosity, meaning the volume fraction of the pores contributing

to ion adsorption. Calibration experiments consist of charging discharging steps in order to measure total absorbed salt and cumulative electric charge, these integral measures can be used to fit the model.

The EDL model used is the mD model, which can be formulated as in Equation 2.2. At chemical equilibrium, there is no electrochemical potential gradient between micro- and macropores. Hence, an extended Boltzmann distribution can be used to relate the micro- and macropore concentration of each species i

$$c_{m,i} = c_{M,i} \quad \exp\left(-z_i \frac{\Delta\phi_D}{V_T} + \overline{\mu}_{att,i}\right), \tag{2.2}$$

where $c_{m,i}$ and $c_{M,i}$ are concentration of species i, m for micro and M for macro. z_i is the species valence. $V_T = kT/e$ is the thermal voltage with k and T and e being the Boltzmann constant, temperature and the elementary charge. ϕ_D is the Donnan (or equilibrium) potential, and parameter $\overline{\mu}_{att,i} = (\overline{\mu}_{M,att,i} - \overline{\mu}_{m,att,i})/kT$ accounts for a nonelectrostatic adsorption potential of ions into micropores. Positive $\overline{\mu}_{att,i}$ may be described as a macro- to micropore chemical potential difference normalized by kT energy, and is one of the free parameters within the model.

Next, volumetric charge density stored in the micropores $2q_m$ and micropore potential drop $\Delta\phi_m$ can be related to micropore capacitance as

$$2q_m F = -C_m \Delta\phi_m, \tag{2.3}$$

where F is the Faraday constant (96485 C/mol). C_m is defined as the effective volume specific capacitance of micropores. C_m can be interpreted as the total charge capacitance per unit volume of micropores and includes all EDL structures including stern layers and/or overlapped diffuse charge layers. This is the second free parameter. Equations 2.2 and 2.3 describe the EDL model used, in this model finite ion size, surface condition and Faradaic reactions are neglected. Here, $\Delta\phi_m$ is the potential drop between the electrode surface and the center of the micropore.

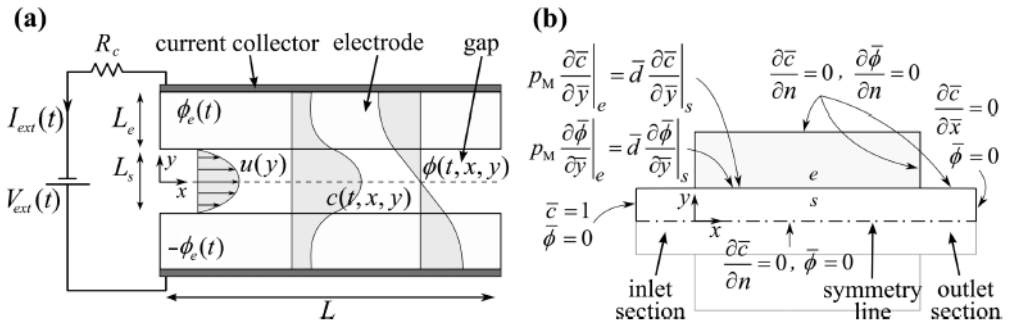

Figure 2.5: (a) Schematic of elements of the 2D adsorption-desorption and flow model for an flow-by CDI cell. Two porous carbon electrodes of thickness L_e are sandwiched between two current collectors. Electrodes are separated by a distance L_s to provide space for flow of water. Contact resistances are lumped into a purely resistive element R_c. (b) Schematic of computational domain and boundary and interface conditions in nondimensional form. The dash-dot-dash line denotes the geometric symmetry line. The computational domain includes inlet and outlet regions for the flow of length $L/8$. Adopted from Hemmatifar *et al.* [24].

To complete the 2D porous electrode model the transport equations are formulated on a volume average basis. The schematic of the 2D flow-by CDI cell is shown in Figure 2.5, alongside with the boundary and interface conditions in nondimensional form. The cell consists of two porous carbon electrodes sandwiched between two current collector plates. The feed water flows in the gap between the electrodes. The gap thickness L_s is much smaller than the electrode width, this allows us to approximate the flow within the gap as Poiseuille-like. It is assumed that the gap and the electrodes are completely filled with water. The general form of mass transport without reaction for species i is

$$\frac{\partial c_i}{\partial t} + \nabla \bullet \mathbf{j_i} = 0, \tag{2.4}$$

where c_i is the concentration of species i and $\mathbf{j_i}$ its associated molar flux vector. This flux includes advection, electromigration and diffusion contributions as

$$\mathbf{j_i} = c_i\,\mathbf{u} - \frac{z_i D_i}{V_T} c_i \nabla\phi - D_i \nabla\phi, \tag{2.5}$$

where $\mathbf{u}$ is the bulk velocity vector, D_i is the diffusion coefficient of species i, and ϕ is the local potential. Within the gap Poiseuille flow is assumed, further assumptions are dilute, binary, symmetric, and univalent electrolyte and thus equal diffusion coefficients. In the pore structure of the electrode, ion transport in macropores is

$$\frac{\partial}{\partial t}\Big(p_M c_{M,i} + p_m c_{m,i}\Big) + \nabla \bullet \Big[c_{M,i}\,\mathbf{u}_{\,sup} - p_M D_{e,i}\Big(\nabla c_{M,i} + \frac{z_i}{V_T} c_{M,i}\nabla\phi\Big)\Big] = 0, \tag{2.6}$$

where p_m and p_M are the porosity of micro- and macropores related to total electrode porosity p as $p_m + p_M = p$, $D_{e,i}$ is the diffusion coefficient within the electrode for species i. In the macropores electroneutrality holds, in the micropores the difference between co- and counter-ion concentrations is balanced by electrode charge density. For simplicity it is assumed that the ratio of $\frac{D_{e,i}}{D_i} = 0.5$. In the macropores $\mathbf{u}_{\,sup} = 0$, as bulk (advective) flow is not important here. Furthermore electroosmotic flow is neglected, because the electrode as a whole is a constant-potential surface. With these assumptions, the governing equations for salt and charge balance, derived from Equation 2.6 by adding and subtracting equations for $i = \pm 1$ can be described as

$$\frac{\partial c}{\partial t} = D_e \nabla^2 c - \frac{p_m}{p - p_m}\frac{\partial w_m}{\partial t} \tag{2.7}$$

$$\nabla \bullet (c\nabla\phi) = \frac{p_m}{p - p_m}\frac{V_T}{D_e}\frac{\partial q_m}{\partial t}, \tag{2.8}$$

where $2w_m = c_m^+ + c_m^-$ is the volumetric ions concentration and $2q_m = c_m^+ - c_m^-$ is the charge density in micropores.

Cation expulsion in the micropores of positive electrode leads to an electric potential mismatch between macro- and micropores. This potential difference is know as the Donnan potential ϕ_D. The potential difference between electrode matrix and pore solution is related to micropore potential drop $\Delta\phi_m$ and Donnan potential as

$$\phi_e - \phi = \Delta\phi_m + \Delta\phi_D, \tag{2.9}$$

where ϕ_e is the time varying but spatially uniform potential of the upper electrode. Due to symmetry, the other electrode has potential $-\phi_e$, as such the cell voltage can be written as $V_{\text{cell}} = 2\phi_e$.

The model includes inlet and outlet domains sufficiently far from the electrode edges. The concentration at the inlet is set uniform and zero gradient is set at the outlet. At both the inlet and outlet zero electric potential is assumed. Other boundary and interface conditions are zero mass and current flux across side walls of the inlet and outlet and across the outer boundaries of the electrodes, advective boundary condition for concentration at the outlet, continuity of concentration and potential as well as salt flux and electric current at the electrode solution interface. The interface conditions for salt flux and electric current at the solution side are multiplied by p_M to correct for the effect of macropore porosity. Furthermore, the assumptions of a binary, symmetric electrolyte allows us to use a symmetry boundary condition for spatiotemporal concentration fields and an anti-symmetry boundary condition for potential.

Next, the desalination system is coupled to an external electrical power source through a contact resistance

$$V_{\text{cell}} = V_{\text{ext}} - R i_{\text{ext}}, \tag{2.10}$$

where R is the electrical resistance and i_{ext} is the external current.

To close the system of equations, a relation between i_{ext} and the flow of ions need to be established. Macropore ionic current $\mathbf{i} = Fz(\mathbf{j}_+ - \mathbf{j}_-)$, after correcting for porosities, can be related to micropore charge flux as $p_M \nabla \bullet \mathbf{i} = -2p_m F(\partial q_m/\partial t)$. External current I_{ext} can thus be found, equivalently, by integrating micropore charge flux over the entire electrode volume (Equation 2.11) or ionic current passing through the electrode-solution interface as

$$I_{ext} = \iint 2p_m F(\partial q_m/\partial t) W dx dy \tag{2.11}$$

$$= \int (2p_M F D_e/V_T)(c\partial\phi/\partial y) dx. \tag{2.12}$$

From the Equations 2.5, 2.7 and 2.8 three fundamental time scales associated with the fb-CDI cell can be identified. The first time scale is the diffusion time of ions across the electrode, L_e^2/D_e. The second is the resistive-capacitive time scale associated with micropore charging. This RC time scale helps interpret the time evolution of charge and salt adsorption within the electrode. It is possible to write the RC time scale as p_m/p_M normalized by the diffusion time scale. The third timescale is the ratio between the feed water flow and the diffusion time across the electrode. This compares the axial advection to the transverse diffusion. The advection time scale is usually written as $\alpha_e Pe_e$, where $\alpha_e = L_e/L$ and $Pe_e = UL_e/D_e$. These time scales will help us to interpret our data in the following chapters.

2.3. Electrode Materials and Manufacturing

This section lists the ideal electrode properties that have been identified from the analysis of performance parameters and performance indicators as well as the parameters affecting CDI operation. As carbon-based electrodes include many of these properties multiple carbon-based electrodes are listed in Table 2.1. Within the table the SAC values reached can be read accompanied by 3 separation conditions. Later this section, activated carbon powder electrodes are highlighted and the manufacturing process explored.

2.3.1. Ideal Electrode Properties

Studies into ideal properties for CDI electrodes showed that high surface area and electrical conductivity are most important [30]. Carbon materials are know to be able to attain high SSA and porous structures, which ensures plenty of available space for electrosorption. The microscopic structure of activated carbon also commonly contains a broad distribution of pore sizes, allowing for effectual electrosorption. Moreover, carbon electrodes have low electrical contact resistance, appropriate wetting behavior, low cost, good process-ability, desirable bio-inertness and chemical stability [2]. All of these properties of carbon material in its many forms made carbon electrodes to be most used in CDI cells. The various forms of carbon used are: activated carbon powder (ACP), activated carbon cloth (ACC), carbon aerogel, carbon nanotubes (CNT), carbide derived carbons and graphene [3, 15, 21, 26, 27, 29, 39, 73]. Metal oxides and carbon composites are used due to their enhanced electrochemical performance [12, 23]. CNT have become a material of special interest in many applications including CDI, however, CNT have been proven to drive carcinogenics and thus working with CNT should be approached carefully [13, 50].

2.3.2. Activated Carbon Powder Electrodes

Activated carbon refers to a wide range of carbonised materials with a high degree of porosity and high surface area. Activated carbon has many applications in industry and outside of industry utilizing their adsorption ability for the removal, retrieval, separation and modification of various compounds in both liquid and gas phase [23]. The production of activated carbon around the world is estimated to be around 100,000 tonnes, common sources of activated carbon are wood, charcoal, lignite, peat shells and coconut. Activated carbon powder is considered to be one of the most cost-effective materials used for CDI electrodes as it is available in bulk and inexpensive. Electrode cost estimated for ACP electrodes is around 0.89 $\$/m^2$, compared to 2.97 $\$/m^2$ for ACF and 450.01 $\$/m^2$ for CNT [10]. The BET SSA of ACP can range up to 3000 m^2/g [18]. To manufacture ACP into an CDI electrode the powder commonly is mixed with a polymeric binder and coated onto a current collector. Furthermore, to lower the material resistance of the ACP coating, a conductive additive (CA) can be added, such as carbon black (CB) [14].

Binders are primarily used to provide mechanical strength to the electrode, different binders are used as the electrode properties are affected by the binder. Polymeric binders used are polytetrafluoroethylene

Table 2.1: Compilation of desalination performance of electrode materials for CDI. Compiled from sources; [30],[34] and [52].

Electrode Material	**SSA (m^2/g)**	**Feed Salinity**	**Applied Voltage (V)**	**mSAC (mg/g)**	**Ref.**
ACP	968	51.2μ S/cm	1.2	0.25	[73]
	968	50.0μ S/cm	1.2	0.27	[72]
	984	117μ S/cm (0.002 M)	1.2	2.6	[26]
	1260	200 mg/L	1.5	-	[15]
	1153	100 mg/L	1.2	6.10	[11]
	"	200 mg/L	"	8.00	"
	"	500 mg/L	"	9.72	"
	"	1000 mg/L	"	10.8	"
	"	1500 mg/L	"	11.0	"
	"	2000 mg/L	"	11.76	"
	630	10 mM	1.2	4.1	[34]
	1095	"	"	6.2	"
	1705	"	"	7.0	"
	2266	"	"	13.6	"
	1707	290 mg/L	1.2	7.7	[52]
	1450	"	"	9.1	"
CWZ-22	-	"	"	5.3	"
Mast Carbon S-TE3	-	"	"	7.6	"
Mast Carbon S-TE11	-	"	"	8.5	"
ACC	1500	550 mg/L	1.1	10	[7]
	1980	5.85 mg/L	1	1.75	[54]
ACC/titania	1890	"	"	4.68	"
ACF	670	4000 mg/L	1.2	8.9	[28]
Carbon Aerogel	602	140 mg/L	1.2	4.51	[67]
	610	50 mg/L	1.5	2.81	[31]
	1500	2900 mg/L	1.25	9.6	[59]
OMC	844	51.2μ S/cm	1.2	0.68	[72]
OM SiC-CDC	2720	290 mg/L	1.2	12.8	[52]
CNT	153	1500μ S/cm	1.2	4.76	[63]
CNT/Graphene Aerogels	435	35000 mg/L	1.6	633.3	[57]
MWCNT	964	0.001 M	1.2	13.07	[27]
Polypyrrole/graphite	0.1407	1000 mg/L	1.4	78.73	[42]
WCF	839	100 mg/L	1.2	5.7	[41]

(PTFE), polyvinylidenefluoride (PVDF), polyvinylalocohol (PVA) and sulfosuccinic-acid [38, 69, 71]. PTFE- and PVDF-bonded electrodes can provide high mechanical strength, yet, capacitance of the electrode is reduced with the increase of binder content, presumably as a result of blocking of the micropores by the polymers [26]. PVA- and sulfosuccinic-bonded electrodes have stronger hydrophilicity and capacitive deionization performance, but less mechanical strength and thermal stability. A combination of PVA and sulfosuccinic-acid can improve desalination efficiency as this binder mixture can function as a cation exchange membrane. Anion and cation membranes help increase the charge efficiency during operation, as co-ion expulsion and ion swapping is restricted. Also PVDF has received much interest as it performs very well regarding mechanical strength, thermal stability and chemical resistance. PVDF-bonded electrodes can reach a capacitance of around 74.4-80.3 F/g, which is higher than those reached by PTFE-bonded electrodes 68.0-72.3 F/g. PVDF can also suppress the Faradaic reactions on the carbon surface [69]. Faradaic reaction remain to be discussed in Section 2.6.1.

2.3.3. Activated Carbon Powder Electrode Manufacturing

Electrodes are produced by coating ACP onto a current collector. The current collector is of high electrical conductivity and ensures all of the applied coating is taken into electrosorption functioning. Current collectors are frequently made from titanium or graphite foil as these materials provide the aforementioned requirements, while being resistant to oxidation or other surface reactions. A coating or slurry consisting of the ACP, CA and binder are mixed together in a suitable solvent and common methods for coating include roll coating, spray coating, evaporative casting and doctor blade casting, see Figure 2.6.

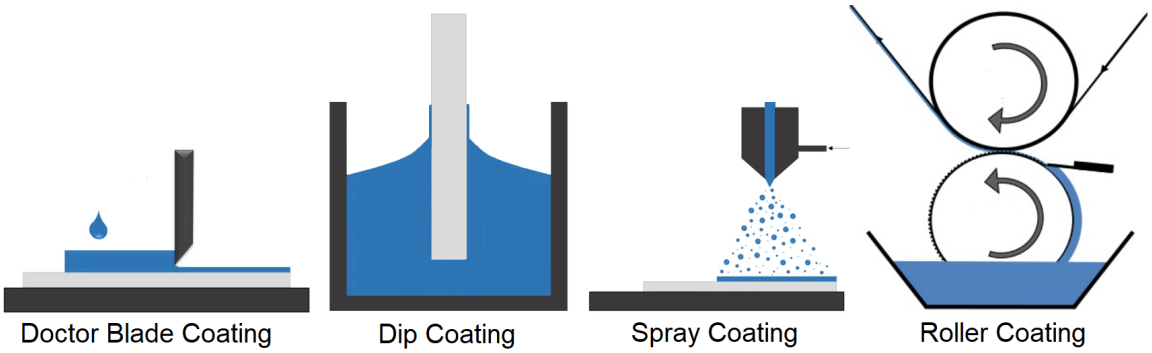

Figure 2.6: Four common methods for coating electrodes.

Roll coating utilizes two rollers that pull and compress the coating onto the current collector in order to form electrodes with uniform thickness. In spray coating the slurry is blown through a nozzle onto the current collector. In evaporative casting, a certain amount of slurry is casted onto the current collector and the solvent is allowed to evaporate. Docter blade casting coates the slurry onto the current collector at a specified wet coating thickness, usually around 300 μm [37]. The coating is then allowed to dry. The drying process can be accelerated by drying in vacuum or at increased temperature. A fast drying process is favorable as it increases the adhesion of the coating onto the current collector due to preventing in-homogeneity in binder distribution along the thickness of the electrode.

The choice of manufacturing affects the performance of the electrode. Roll coating and spray coating result in denser electrodes compared to evaporative casting [43]. The electrodes Lu manufactured using a modified evaporative casting method resulted in loose structure containing many cracks on the electrode surface, which reduce surface stresses, improved durability and increased electrode surface area and wettability.

Besides its application, also the preparation of the coating material should be optimized for optimal properties. Proper mixing should be in place to yield the favorable electrode morphology. The ideal morphology can be seen in Figure 2.7. Commercially-available ACP typically consists of 2-10 μm. These particles, however, stick together in aggregates. In the aggregates the particles are relatively strongly bonded together. Next to primary aggregate formation, the aggregates themselves bond together to from an agglomerate. Agglomerate and aggregate formation is present in both ACP and CA powders. To obtain the preferred properties for the coating these agglomerates need to be broken down into aggregates and the aggregates need to be broken down into individual particles. There are different options one can utilize: a hydrodynamic mixer, kneader, stirred ball mill, 3 roller mill or ultrasonic mixing.

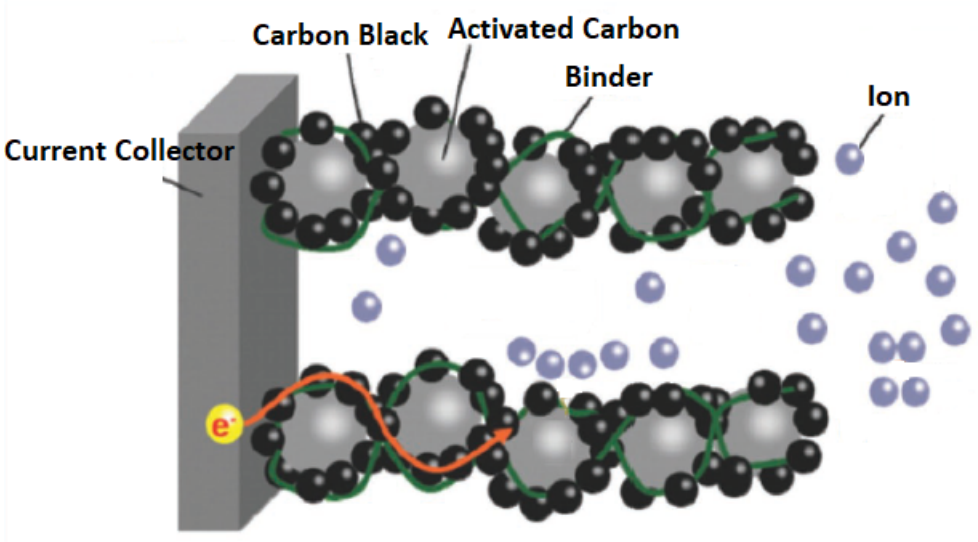

Figure 2.7: Schematics of the idealized activated carbon powder electrode, adopted and modified from Kraytsberg [37]. The ACP and CA are displayed as individual particles or small aggregates. The CA chains preferably around the ACP to form electron pathways lowering the electrical resistance of the coating. The ACP particles enclosed by CA are tied together by the binder. The interconnected particles are attached to the current collector and space is present between the interconnected chains to allow for ion transport.

Hydrodynamic shear mixing is controlled by flow shear rate, cluster cross-sectional are and the dynamic viscosity of the slurry. Cluster breakup takes place in the form of erosion, rupture and shattering. In a stirred ball mill the same processes take place except the intensified by the addition of small hardened balls. Stirred ball mixing results in a finely intermixed slurry, however, the ACP and CA particles morphology can be compromised [37]. This method is therefore not recommended as the particular morphology is suggested to be essential for electrode performance. Ultrasonic mixing has a mixing action at the micro-scale controlled by transient acoustic cavitation, yet it also initiates mixing on the macroscale due to bubbles forming around the sonic probe axis. Macroscale mixing is started as the concentration of bubbles formed decreases outward from the sonic probe axis. The bubbles diffuse towards areas with low bubble concentration, here the flow can be as high as 2 m/s [19]. This flow is often sufficient for smaller fluid volumes. The relatively low ultrasound frequencies, down to 20 kHz, are advantageous for slurry preparation. It must be mentioned that this method is in opening stages of development and therefore accurate comparison between other mixing methods is not available, generally ultrasonic mixing provides similar mixing quality as the hydro-dynamic-based mixing at substantially lower energy input conditions.

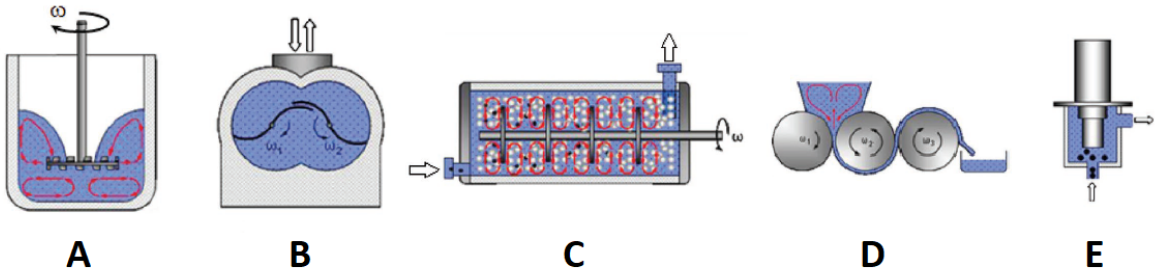

Figure 2.8: Schematics of the most common dispersing equipment: A) the most often employed hydrodynamic shear-based mixers, B) kneaders and C) stirred ball mills, D) 3-roller mills, E) ultrasonic homogenizers. Adopted and modified from Kraytsberg [37].

Next to the mixing method the sequence of steps taken to prepare the coating can be tailored as well to obtain more preferable results. Dispersing the ACP and CA in solvent separately form dispersing the binder in solvent and adding them together later resulted in a substantial more rigid electrode, the Youngs-modulus of the electrode turned out three times as high [70]. It is suggested that in case the binder is dispersed first the more viscous solvent could not penetrate properly into the ACP clusters and spread over all the ACP surface as the ACP was later added [37].

There is also an option to post-process activated carbon electrodes to increase their performance. Activated carbon electrodes can be immersed in potassium hydroxide (KOH) solution to improve the electrosorption capacity. Activation of carbon via KOH is a chemical way to activate carbon [23]. Treating the electrodes in 1 M KOH solution for 24 hours increases the capacity with 5.2% as compared to untreated electrodes [1, 26]. Furthermore metal oxide modification and surface coating can be applied to improve desalination performance [12, 40].

2.3.4. Crack Formation in Colloidal Films

In Section 2.3.3, it was mentioned that as the coating dries cracks can form. Crack formation is a heavenly studied field of research, with applications in the paint, coating and ceramics industries. Cracks often result of residual stress release from colloidal films made by the evaporation of colloidal droplets containing nano particles, see Figure 2.9. Cracks greatly increase the electrical resistance of the electrode made and thus should be prevented. There are sources that state that the presence of cracks could be beneficial for CDI operation as it opens up the electrode surface to the electrolyte , however, this can only be the case as there is a well conducting current collector incorporated in the electrode to accommodate the electron pathway largely [43]. Capillary pressures created by liquid menisci between colloidal carbon are responsible for cracking. Capillary pressures generate tensile stresses normal to the colloidal film. The critical cracking thickness (CCT) is determined by the maximum capillary pressure beyond which the liquid menisci recede into the porous colloidal film. The CCT is proportional to particle radius (r) and particle shear modulus (G) via $h_{\max} \propto r^{3/2} G^{1/2}$. Moreover, it is dependent on particle volume fraction. Cracks are observed to be thicker with wider spacing form each other at higher particle volume fractions. To reduce crack formation a polymer binder can be added to provide gelation-driven crack prevention [33].

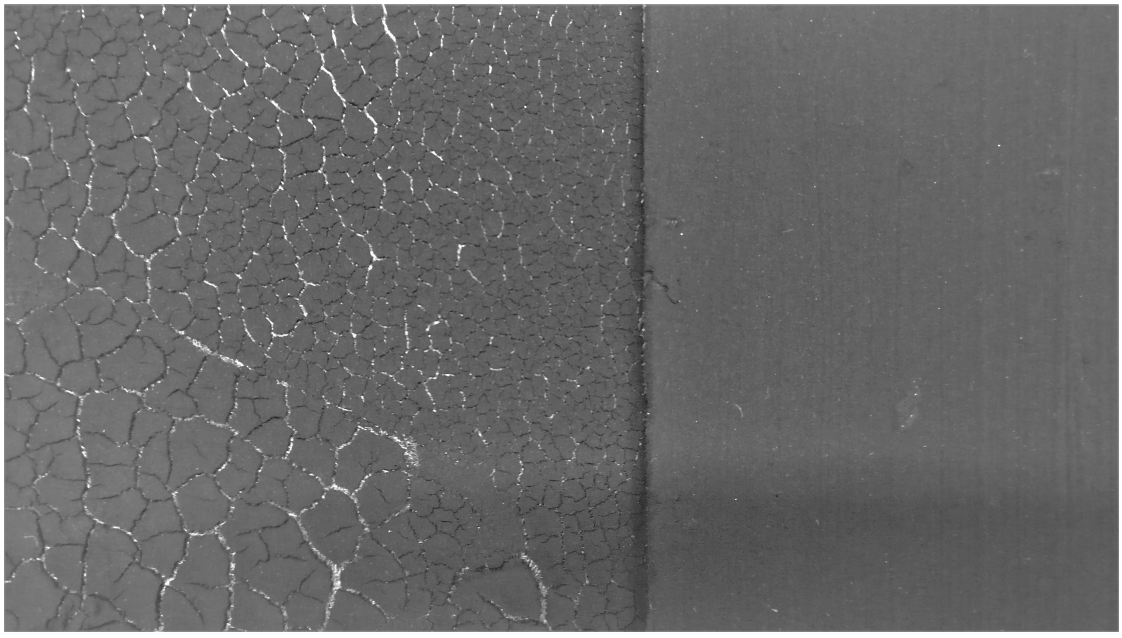

Figure 2.9: Carbon coated electrode surface appearance from a cracked electrode (left) next to a successfully coated electrode (right).

2.4. Performance Metrics

Given the broad range of CDI architectures, it is imperative to find out how CDI performance is measured. As the research field of CDI is growing, guidelines are established for evaluating, reporting and comparing device performance. Much research into CDI is focused on materials and methods to improve the efficiency and desalination capacity of the system, but many published studies are not easily comparable to one another. This is because either critical performance parameters are not reported, or the desalination conditions are substantially different. In other desalination methods, such as RO and ED, energy consumption per volume and volume throughput are commonly identified and reported. To be able to compare CDI performance to these metrics the water recovery, feed salinity, and total concentration reduction would have to be equal.

For example, energy consumption per volume and volume throughput are heavily dependent on the separation conditions. Extrapolating desalination performance from one condition to another set of conditions can not be straightforwardly done. In the absence of a framework for reporting deionization performance the field of CDI turned to a number of different metrics to compare desalination performance. Commonly used metrics are: the salt adsorption capacity (SAC, mg/g of electrodes), average salt adsorption rate (ASAR, in mg/min/cm^2), energy consumption per mole of salt removed (kJ/mol), energy normalized adsorbed salt (ENAS, μmol/J), and specific energy consumption (SEC^{-1}, mg/J). All these metrics are insightful for CDI processes, however, a minimal-necessary set of metrics should allow for better comparison between future studies. The following framework for comparing deionization performance is proposed by Hawks *et al.* [22]. This framework rank orders performance metrics in primary performance metrics, secondary performance metrics and performance indicators. The synopsis of the framework can be seen in Figure 2.10, displaying the most valuable desalination performance metrics and important separation conditions.

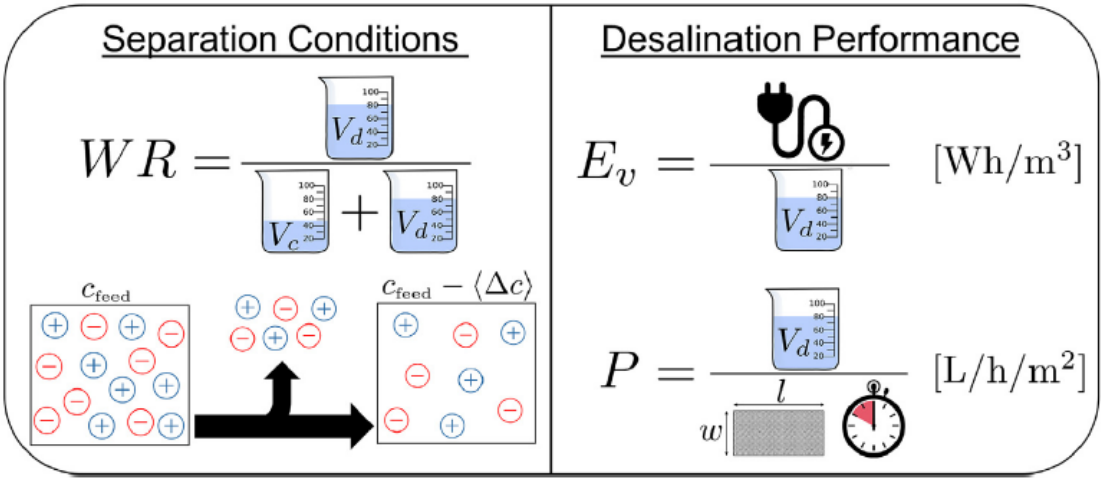

Figure 2.10: A pictogram illustrating how to objectively compare deionization performance. First, the separation conditions must be defined (water recovery, feed concentration, and concentration reduction), and then the desalination performance (energy consumption, throughput) can be compared. Adopted from Hawks *et al.* [22].

2.4.1. Primary Performance Metrics

For evaluating the economically relevant desalination performance of CDI the primary performance metrics are volumetric energy consumption (E_v, in Wh/m^3) and throughput or productivity (P, in $L/h/m^2$). In order for these metrics to be viable the target separation must be defined. The target separation includes: the feed salt concentration (c_{feed}), the concentration reduction ($\langle \Delta c \rangle$) and the water recovery (WR).

Water recovery measures the fraction of diluted water gained that, has a lower salinity relative to the feed stream. Water recovery (WR) is defined as

$$WR = \frac{V_d}{V_d + V_c}, \tag{2.13}$$

where Q is the volumetric flow rate through the cell, V_d is the volume of desalinated water (diluate) that, when mixed, has a lower salinity relative to the feed stream, V_c is the volume of concentrate that, when mixed, is enriched in salt relative to the feed stream. V_c and V_d are calculated as

$$V_d = \int_{\Delta t_d} Q \quad dt; \tag{2.14}$$

$$V_c = \int_{\Delta t_c} Q \quad dt, \tag{2.15}$$

where Δt_d is the time interval in which the desalinated water is collected and Δt_c is the time in which the concentrate stream is collected.

Concentration reduction measures the difference between the feed concentration and the concentration of dilute water,

$$\langle \Delta c \rangle = \frac{\Delta N_d}{V_d}, \tag{2.16}$$

where ΔN_d is the salt removed over one cycle relative to the feed stream as measured from the desalinated water (mol). Similarly, ΔN_c is the amount of salt added to the concentrate stream in one cycle,

$$\Delta N_d = \int_{\Delta t_d} Q(c_{\text{feed}} - c_{\text{out}}(t)) \quad dt; \tag{2.17}$$

$$\Delta N_c = \int_{\Delta t_c} Q(c_{\text{out}}(t) - c_{\text{feed}}) \quad dt, \tag{2.18}$$

where ΔN_c is the salt added to the concentrate stream over one cycle as measured by the effluent (mol), c_{out} is the effluent salt concentration (mM) and $\langle \Delta c \rangle$ is the average concentration reduction (mM).

The net volumetric energy consumption is the amount of energy supplied to the system, minus the amount of energy recovered from the system, per volume dilute water, e.g.,

$$E_v = \frac{E_{\text{in}} - \eta E_{\text{out}}}{V_d}, \tag{2.19}$$

where E_{in} is the energy input during the dynamic steady state (DSS) cycle (J), E_{out} is the total recoverable energy from the cell over DSS cycle (J) and η is the fraction of E_{out} actually recovered and reused to power another charging phase. The energy input and output are

$$E_{\text{in}} = \int_{\Delta t_{\text{cycle}}} IU \quad dt \quad \text{where} \quad IU > 0; \tag{2.20}$$

$$E_{\text{out}} = \int_{\Delta t_{\text{cycle}}} IU \quad dt \quad \text{where} \quad IU < 0, \tag{2.21}$$

where IU is the current-voltage product for a single electrode pair (W), Δt_{cycle} is the total dynamic steady state cycle time (s).

The productivity of a CDI system describes the volume of dilute water produced per unit time and electrode area. Productivity of the CDI system is defined as

$$P = \frac{V_d}{nA\Delta t_{\text{cycle}}}, \tag{2.22}$$

where n is the number of electrode pairs in the CDI stack, A is the projected face area (cm^2) of one cell.

2.4.2. Secondary Performance Metrics

Secondary performance metrics give more detailed information of the CDI system in question and can be used for comparing CDI systems to each other in more detail. These metrics can be used to compare CDI performance versus CDI performance. The secondary performance metrics are molar energy consumption, average salt adsorption rate and energy normalized adsorbed salt.

Molar energy consumption details the amount of energy used per mole salt removed, and is described as

$$E_{molar} = \frac{E_{\text{in}} - \eta E_{\text{out}}}{\Delta N_d}. \tag{2.23}$$

The average salt adsorption rate is used to describe the rate of salt removed over time, and is described as

$$ASAR = \frac{\Delta N_d}{nA\Delta t_{\text{cycle}}}. \tag{2.24}$$

Energy normalized adsorbed salt is a metric that details the amount of energy used per amount of salt adsorbed, and is described as

$$ENAS = \frac{\Delta N_d}{E_{\text{in}} - \eta E_{\text{out}}}. \tag{2.25}$$

2.4.3. Performance Metric Relationships

Productivity is the metric for describing how much dilute water is produced in a certain amount of time and using a certain amount of electrode surface. From Eq. 2.22 and 2.24 one observes that the two are related like,

$$P = \frac{ASAR}{\langle \Delta c \rangle}. \tag{2.26}$$

The volumetric energy (E_v) can be derived from ENAS and $\langle \Delta c \rangle$. In the case of low ENAS a higher level of energy is required per volume water desalinated, as can be seen from the relation

$$E_v = \frac{\langle \Delta c \rangle}{ENAS}. \tag{2.27}$$

A similar logical relation is found between molar energy and volumetric energy consumption. The molar energy consumption can also be defined as

$$E_{molar} = \frac{E_v}{\langle \Delta c \rangle}. \tag{2.28}$$

The energy used per time and electrode area can be determined by multiplying productivity with volumetric energy consumption, dividing ASAR with ENAS supplies the same result

$$PE_v = \frac{ASAR}{ENAS}. \tag{2.29}$$

2.4.4. Performance Indicators

The performance indicators are highly useful for understanding cell performance and material limitations, but are not performance metrics themselves. These parameters combined with the reported operational performance metrics above can help better understand which materials, cell architectures, and operation modes are suitable for CDI. If the primary goal of the study is to evaluate a novel electrode material, then such extra characterization is especially critical. Performance indicators are salt adsorption capacity, capacitance, point of zero charge (E_{PZC}), charge efficiency, coulombic efficiency and series resistance, as discussed below.

The SAC value details the amount of salt adsorbed in grams salt per grams electrode material. The mSAC value is the maximum amount of salt adsorbed in the electrode at a certain constant voltage. The mSAC value is usually measured at $U = 1.2V$ (with the discharge voltage typically set to zero), a salinity of 20 mM and using synthetic NaCl so that experiments can be compared between different studies [58]. SAC is defined as

$$SAC = \frac{M_w}{m} \Delta N_d, \tag{2.30}$$

where M_w is the molar mass of the salt, m is the total mass of the electrodes in the cell.

The electrical capacitance in response to an applied electrostatic potential is an important factor that underlies SAC. Capacitance indicates the ability of a system to store an electric charge. As the amount of excess electric charge needs to be compensated by an excess of ionic charge of the opposite sign, the capacitance data can be used to predict SAC values [35, 55]. Electrical capacitance can be calculated within the capacitive functioning area like

$$C = I\left(\frac{dU}{dt}\right)^{-1}, \tag{2.31}$$

where U is the cell voltage (V), I is the current (A) and C is the capacitance (F). The predicted salt adsorption capacity (SAC_p) can be determined using

$$SAC_p = \frac{1000CUM_w}{4F}, \tag{2.32}$$

where SAC_p is in units (mg/g), C (F/g) is the specific capacitance of a single electrode measured using galvanostatic charge/discharge tests, and M_w is the molecular weight of the ion in the feed solution (NaCl, 58.433 g/mol). Using Eq. 2.32 results in predicted SAC values that are shown to overestimate the actual adsorption capacity. For capacitance data acquired using 0.01 M NaCl the actual result will be within the range after factoring with 0.6 - 0.8. For capacitance data acquired using 1 M NaCl the actual result will be within the range after factoring 0.5 - 0.6. 60 - 80% and 50 - 60% of the charge capacity evaluated from capacitance were utilized in deionization.

The E_{PZC} is defined as the electric potential (w.r.t to the standard hydrogen electrode potential) at which the electrode surface has no excess charge. The E_{PZC} is relevant for CDI as electrosorption of counter-ions is accompanied by desorption of co-ions (co-ion expulsion), what can be considered as a parasitic capacitive process that reduces the charge efficiency of CDI. The E_{PZC} can be modified by chemical surface treatments, optimal efficiency is reached as E_{PZC} is the same as E_0 the shorting potential [2, 5]. If E_0 coincides with the E_{PZC} the electrode has no excess of adsorbed cations or anions before the electrosorption process begins and the largest capacity is available during CDI operation with symmetrical electrodes. The most common approach to measure the latter parameter is to determine the minimum of the differential capacity predicted by the Gouy-Chapman theory.

Charge efficiency depicts how well the electronic charge binds ionic charge within the electrode. Due to co-ion expulsion and ion swapping, charge efficiency is never 100%. A high charge efficiency boosts the desalination capacitiy as there is limited amount of co-ion expulsion and ion swapping taking place [28]. Coulombic efficiency relates the charge supplied to the system during charging to the charge released from the system during discharging. Differences between these values arise due to leakage currents or Faradaic reactions, as discussed below. Charge efficiency and Coulombic efficiency are defined as

$$\Lambda_{\text{cycle}} = \frac{F\Delta N_d}{q_{\text{in}}}; \tag{2.33}$$

$$\eta_{\text{coul}} = \frac{q_{\text{out}}}{q_{\text{in}}}, \tag{2.34}$$

where q_{in} is the charge transferred at positive current, q_{out} is the charge transferred at negative current. The charge in and the charge out are described as

$$q_{\text{in}} = \int_{\Delta t_{\text{cycle}}} I \quad dt \quad \text{when} \quad I > 0; \tag{2.35}$$

$$q_{\text{out}} = \int_{\Delta t_{\text{cycle}}} I \quad dt \quad \text{when} \quad I < 0. \tag{2.36}$$

The series resistance (R_s) can be used to calculate Joule heating within the CDI cell. R_s is the total of the external electronic resistance (R_{EER}) plus the separator resistance (R_{sp}). R_{sp} is an ionic resistance that can be calculated as

$$R_{sp} = \frac{l_{sp}\tau_{sp}}{A\kappa p_{sp}}, \tag{2.37}$$

where l_{sp} is the separator thickness (μm), τ_{sp} is the separator tortuosity, κ is the electrolyte conductivity in the separator (mS/cm) and p_{sp} is the separator porosity.

Note that besides Joule heating, energy loss can also occur via Faradaic reactions, which is not included in this equation. Faradaic redox reactions are chemical reactions that are undesired in CDI operation. These reactions will be discussed in Section 2.6.1.

2.5. Parameters Affecting CDI Performance

The different CDI architectures and the means to rank order the performance of these different architectures are now established. To add to the understanding for CDI functionality the relevant parameters affecting CDI performance are discussed in this section. Many factors influence the performance of CDI, yet the performance of the electrode material is paramount. Parameters such as surface area, pore size, pore distribution, applied electrical potential, concentration, type of ions, electrode resistance, electrode thickness and specific capacitance, all affect electrosorption.

2.5.1. Specific Surface Area

The specific surface area (SSA) quantifies the space for ions to be adsorbed onto the electrode surface. Thus, good SSA is essential for obtaining higher specific capacitance. SSA is frequently determined using Brunauer-Emmett-Teller (BET) theory [9]. From the simplified Helmholtz EDL model, which we discuss in more detail in Section 2.2, it is easily noted that large surface area improves CDI performance. This statement is correct even as the Helmholtz model alone is insufficient to describe the EDL. While it has been demonstrated that there is no direct relationship between SAC and BET SSA [52], it can be predicted by an additional analysis of the pore size distribution, considering that differently sized pores exhibit different electrosorption behaviour.

2.5.2. Pore Size and Distribution

Early research into the electrosorption process in porous materials showed that the average pore size had significant effect on the charging of the double layer. In porous materials the pores can be catagorized in macropores, mesopores and micropores with pore widths of > 50 nm, 50 > 2 nm and 2 > nm respectively. It was found that pores with a pore width smaller than 0.6 nm cannot hold any ion [30]. This lower limit is set by the finite size of the charged ions in water due to a hydration shell, effectively increasing its size, and preventing them to enter very small pores. As a result, in the micropores > 0.6 nm the highest electrosorption density can be found. Although the exact value will depend on the ion type. The increase in electrosorption density relative to the meso- and macropores can be explained by EDL overlapping, modifying adsorption behaviour [21]. EDL overlapping occurs as the surface where the EDL is formed onto is situated closely to an opposite surface onto which another same nature EDL is formed. As the EDLs are more and more closely together they influence each other more and more, increasing and modifying adsorption behaviour. EDL overlapping is discussed in more detail in Section 2.2. In the mesopores the electrosorption density decreases along with the resistance to ion transport and the increase in surface area. Thus, even as electrosorption density decreased the total amount of adorbed ions is largest in the mesopores. Macrosized pores act as ion-buffering reservoirs, allowing for shorter ion diffusion distances, facilitating rapid transport of ions from the bulk material into the interior. From these findings it is suggested that multi-porous fractal-structured electrodes with macropores ending in mesopores, and mesopores being the entries of micropores are preferred.

2.5.3. Applied Electrical Potential

Increasing the applied potential difference between the electrodes increases the electrosorption capacity [30]. Higher voltages also cause the EDL to be more compact, with higher applied potentials the EDL is condensed and the ion removal efficiency significantly improves. The potential that can be applied is limited and should never exceed 1.23 V, which is the standard potential for unwanted water electrolysis. Most desalination experiments are conducted at 1.2 V for this reason, as well as to be comparable to other studies.

2.5.4. Concentration and Ion Type

The shape of the EDL and thus electrosorption capacity are depended on concentration. Large ion concentration result in larger adsorption capacity and thinner EDLs at the same applied potential. Increasing the concentration, however, causes a decrease in charge efficiency. The mechanism allowing for this drop is likely the increase in need for ion-expulsion during charging [58]. A larger concentration also lowers the resistance of the electrolyte and lower resistance of the solution means faster kinetics. Another way for the concentration to influence the electrosorption process is via modifying the effective size of the ions. Very large ionic strength results in smaller hydration shells leading to easier transport of ions into the electrode pores [30], although it is unlikely that CDI experiments will be carried out in this regime.

The larger the valence of the ion the larger the hydrated radius will be, making the ion more resistant to transport into the electrode and less able to be adsorbed into the smallest pores. Due to the larger charge of the ion one could expect an easier adsorption behaviour, however, with the presence of the hydrated shell

this can actually be more of a hindrance.

2.5.5. Electrode Thickness and Symmetry

For symmetrical electrodes, research showed that the highest values for SAC are reached in case the opposite electrodes are of equal mass [51]. Symmetrical electrodes are usually referred to electrodes that adsorb cations and anions like-wise, assignment of the cathode and anode within the cell can be interchanged (e.g. by reversing the electrostatic potential). In the situation of mass asymmetry, meaning the mass of the anode is not equal to the mass of the cathode, it is found that as the asymmetry grows, the mSAC values gradually decrease, regardless if an excess of mass resides within the cathode or anode. This observation confirms that the EDL that is formed is independent of sign, and thus the statement of symmetrical electrodes holds. However, regarding adsorption values of the individual electrode, values increase for the minority electrode. As the applied electrostatic potential difference is distributed evenly between the two electrodes, the minority electrode experiences higher charge and salt adsorption densities. Using a thicker electrode is also an easy way to increase the salt adsorption capacity of the system .

2.6. Degradation and Long-Term Stability

Studies on long-term performance of CDI electrodes have shown a decrease in adsorption capacity compared to the normal adsorption/desorption cycles. Prolonged standard charge-discharge cycling can even start to exhibit a completely reverse adsorbance/desorbance. After significant degradation the electrode can start to release ions as the cell is charging and capture ions as the cell discharges, this is referred to as the 'inversion effect'. The process behind the degradation of the electrodes can be attributed to the oxidation at the positive electrode [16]. This degradation is the result of Faradaic reactions taking place during CDI operation.

In idealized CDI electrodes symmetry is often assumed, meaning that the electrodes ion in similar fashion regardless of the sign the electrode is polarized in. As the electrodes polarized their potentials below the electrolysis potentials of water it is frequently assumed only electrostatic reactions take place. The electrosorption/desorption behavior of such symmetrical cell is shown in Figure 2.11A, the explanation of how to read Figure 2.11 is shown in Figure 2.12. However, there are situations in which the positive electrodes are not ideally polarized because a parasitic oxidation process takes place in parallel to the electrostatic interactions. As a result three electrode properties are affected: the point of zero charge, the electrosorption capacity and the electrical resistance of the electrode.

The degradation of the positive electrode occurs in a couple stages following each other. First, the surface of the electrode may be oxidized, causing for a positive shift of the point of zero charge. This shift relocates the working potential domains, affecting the adsorption capacity, this stage of degradation is show in Figure 2.11B. Figure 2.11B represents the inversion point as this is the shift in point of zero charge for both electrodes to achieve equal adsorbtion/desorption of both ion types while charging. Now if the cycling continues the positive shift enlarges and oxidation has a significant affect on the electrode resistance. The increased difference in electrode resistance redistributes the applied potential unequally, according to Ohm's law. Figure 2.11C represents this scenario, it clearly shows the difference in working potential domains and it can be seen that as the positive electrode is charged a significant amount of ions are desorbed while charging while only a small amount is adsorbed, resulting in the inversion effect.

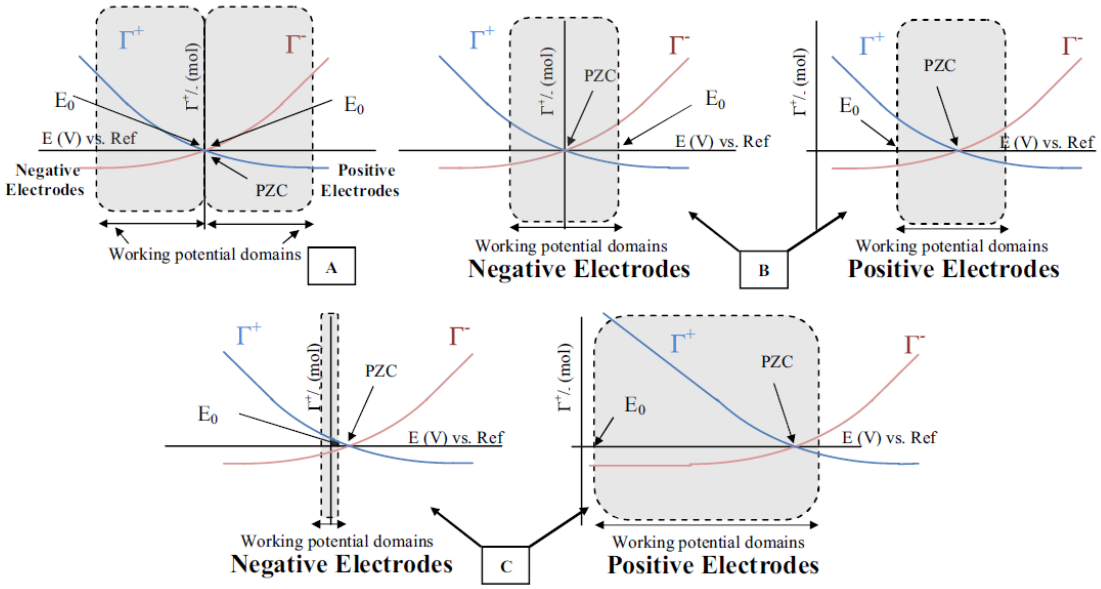

Figure 2.11: (A) Illustration of the operation of a symmetric CDI cell whose electrodes are shorted to 0 V upon discharge. (B) The inversion point – illustration of the operation of unsymmetrical CDI cells, which positive electrodes are oxidized and their E_{PZC} were positively shifted. (C) Illustration of the operation of unsymmetrical CDI cells, which positive electrodes are oxidized and have a high resistivity and a low surface area because of detrimental oxidation processes. The electrode's E_{PZC} and the potential of cell shorting, E_0, vs. a virtual reference electrode, are marked therein. A graphical explanation of how to read the Figure 2.11 illustrations is given by Figure 2.12, adopted from Cohen et al.[16]

2.6.1. Faradaic Reactions

The inversion effect shows that alongside electrostatic interactions Faradaic reactions take place. Faradaic reactions can have both negative and positive effects. The negative effects as described earlier can be a decrease in electrode performance, decreased energy efficiency, formation of chemical by-products, pH fluctuations and shortened electrode lifespan. However, some Faradaic reactions can also contribute to positive effects [68].

The Faradaic reactions can be split up in 3 types of reactions. Type I are the oxidation reactions that occur at the anode including carbon electrode oxidation, chloride oxidation, water oxidation and other contaminant oxidation reactions such as oxidation of inorganic ions and organic matters. Here the carbon oxidation reactions causes for the deterioration of CDI performance and the following inversion effect. Type II Faradaic reactions are the reactions occurring at the cathode. Most common is the oxygen reduction. H_2O_2 is the by-product of oxygen reduction that can open up possibility for use in disinfection of the produced water. Furthermore reduction reactions at the cathode can remove heavy metals by deposition on the electrode. Type III are reversible Faradaic reactions that provide pseudocapacitive/intercalation effects. A schematic presentation of the types of Faradaic reactions is shown in Figure 2.13.

The Faradaic reactions potentials are referenced to the Standard Hydrogen Electrode potential (SHE). The SHE forms the basis that is needed to calculate cell potentials using different electrodes or different concentrations, the value of the SHE is set to zero by definition. Using the SHE electrode as a reference electrode involves using hydrogen gas, therefore other stable electrodes are used as reference electrodes like the Ag/AgCl reference electrode which is much used in practice. Using a reference electrode allows the 1.2 V difference in electrostatic potential to be more precisely pinpointed as values for the absolute potential of the cathode and anode each. It should be noted that, in case the 1.2 V differential is not applied (e.g. shortcircuit), that the electrodes are not at zero absolute potential. However, they return to their intrinsic potential at rest, which is E_0. In case E_0 is vastly different from E_{PZC}, co-ion desorption can become a dominant process in the charging process.

The standard electrode potential for carbon oxidation is 0.21 V (vs. SHE), that is well within the operating window of CDI. Thus, during the desalination process the carbon electrode starts to incorporate oxygen containing groups and potentially being converted to CO_2. The direct oxidation processes that occur as the anode is polarized are shown in Equations 2.38, 2.38 and 2.40. Indirect oxidation can occur as a result of anodic generation of oxidants such as chlorine and hydroxyl radicals.

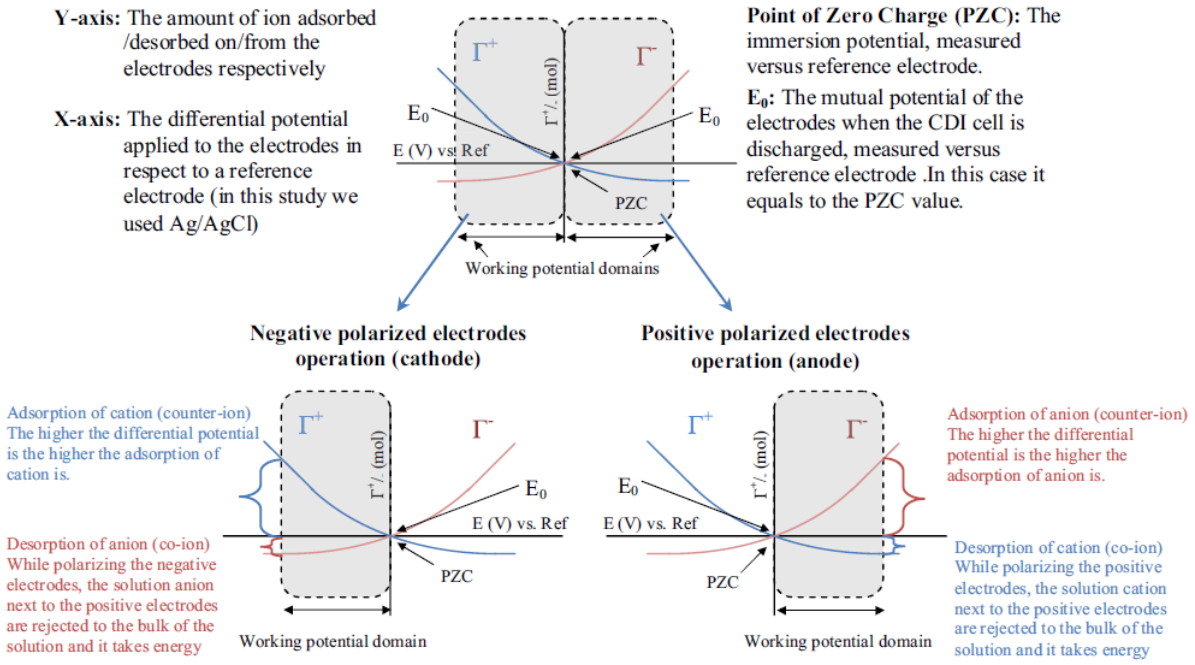

Figure 2.12: Illustration of typical ion adsorption/desorption behavior of symmetric identical electrodes in the CDI cell. Explanation about how to read Figure 2.11, adapted from Cohen *et al.* [16].

$$C + H_2O \rightarrow C{=}O + 2H^+ + 2e^- \tag{2.38}$$

$$C + H_2O \rightarrow C{-}OH + H^+ + e^- \tag{2.39}$$

$$C + 2H_2O \rightarrow CO_2 + 4H^+ + 4e^- \qquad E^0 = 0.21 \quad V \quad vs. \quad SHE \tag{2.40}$$

Anodic oxidations of Cl^- and H_2O may occur during CDI provided the potentials are sufficiently positive to drive these reactions. Anodic oxidation of Cl^- happens according to three steps, direct oxidation of Cl^- yields Cl_2, Cl_2 is rapidly hydrolyzed and disproportionates to form hypochlorous acid (HClO). HClO and its deprotonated form ClO^- can be further oxidized to chlorate (ClO_3^-). Additionally, direct oxidation of Cl^- to ClO_3^- can happen aswell.

Anodic water oxidation can occur as in Equation 2.46 and 2.47. To limit the amount of current leakage due to water electrolysis, the CDI process is operated at charging voltages below the limit of 1.23 V. An anodic potential sufficient to start oxidation of Cl^- to Cl_2 can be used to utilize the disinfection utility of Cl_2.

$$2Cl^- \rightarrow Cl_2 + 2e^- \qquad E^0 = 1.36 \quad V \quad vs. \quad SHE \tag{2.41}$$

$$Cl_2 + H_2O \rightarrow HClO + H^+ + Cl^- \tag{2.42}$$

$$HClO \rightarrow H^+ + ClO^- \tag{2.43}$$

$$6HClO + 3H_2O \rightarrow 2ClO_3^- + 4Cl^- + 12Cl^- + 3/2O_2 + 6e^- \qquad E^0 = 0.46 \quad V \quad vs. \quad SHE \tag{2.44}$$

$$Cl^- + 3H_2O \rightarrow ClO_3^- + 6H^+ + 6e^- \qquad E^0 = 1.45 \quad V \quad vs. \quad SHE \tag{2.45}$$

$$2H_2O \rightarrow O_2 + 4H^+ + 4e^- \qquad E^0 = 1.23 \quad V \quad vs. \quad SHE \tag{2.46}$$

$$H_2O \rightarrow OH^- + H^+ + e^- \qquad E^0 = 2.80 \quad V \quad vs. \quad SHE \tag{2.47}$$

Dissolved oxygen will be in CDI feed with certainty. As a result, oxygen reduction occur following Equations 2.48, 2.49 and 2.50. The cathodic reduction of oxygen most likely occurs via the two-electron transfer pathway.

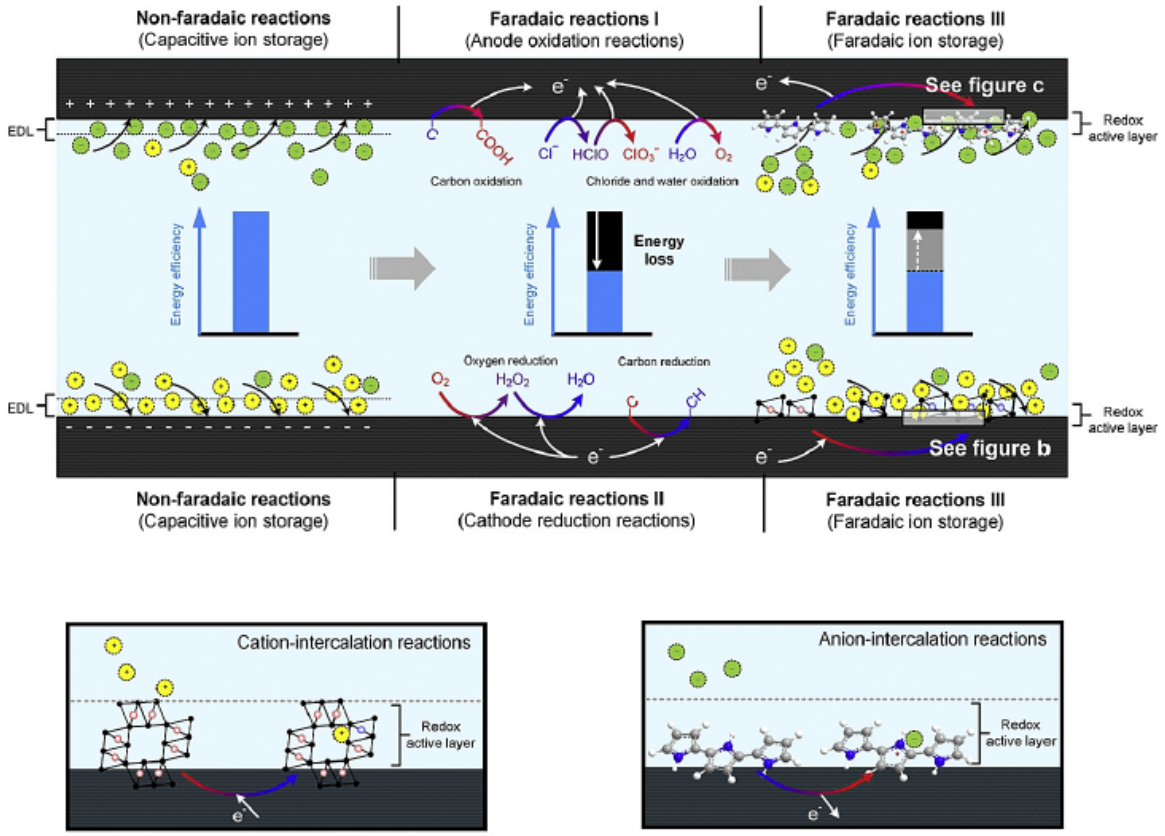

Figure 2.13: Schematic presentation of three types of Faradaic processes (anodic oxidation, cathodic reduction and Faradaic ion storage processes, adopted from Zhang [68].

$$O_2 + 2H^+ + 2e^- \rightarrow H_2O_2 \qquad E^0 = 0.69 \quad V \quad vs. \quad SHE \tag{2.48}$$

$$H_2O_2 + 2H^+ + 2e^- \rightarrow 2H_2O \qquad E^0 = 1.78 \quad V \quad vs. \quad SHE \tag{2.49}$$

$$O_2 + 4H^+ + 4e^- \rightarrow 2H_2O \qquad E^0 = 1.23 \quad V \quad vs. \quad SHE \tag{2.50}$$

Next to carbon oxidation at the anode, there is also carbon reduction going on at the cathode. Additional C – H groups are formed as a result. Whether this reaction actually takes place is not supported by evidence, however it is mentioned in studies [68].

$$C + H_2O + e^- = C - H + OH^- \tag{2.51}$$

Next to CDI performance degradation via Faradaic reactions, fouling and scaling can decrease performance. Fouling is the build-up of unwanted material on the electrode surface, blocking electrosorption. Scaling is a type of fouling caused by inorganic compounds, involving crystallization of solid salts, oxides, and hydroxides from solutions. Organic material is main source for fouling in CDI systems. Fouling results in a degradation of CDI performance with removal efficiency dropping from 86% to 70% after 30 hours of operation using 3.1 mg/L total organic content (TOC) in the feed. It was also found that Fe^3+ ions caused for scaling in CDI systems resulting in lower efficiency and flow rate. The problem of fouling can be alleviated by applying alkaline cleaning while scaling can be moderated by applying acid cleaning [44].

3

Methodology

3.1. Electrode Manufacturing

To develop electrodes that are well suited for MC-CDI operation and scalable to be manufactured on an industrial scale, the electrodes are build based on activated carbon powder (DARCO®, Sigma-Aldrich) coated onto a support structure. ACP contains large specific surface area for ion adsorption, can conduct current, is mechanically and chemically stable and is already cost-efficiently produced in bulk. The conductivity of the coating is improved by addition of a carbon black (VULCAN XC-72, Cabot Corp.), and the coating is bound together by the polymeric binder (PVDF, Mw 534,000, Sigma-Aldrich). Before use, this binder is dissolved in dimethylsulfoxide (DMSO, Fisher Bioreagents). The coating is applied onto four different support structures: carbon fiber paper (Carbon fiber non-woven, 20 g/m^2, h = 0.17 mm, R&G Faserverbundwerkstoffe GmbH), carbon fiber (Carbon fabric, 160 g/m^2, h = 0.26 mm, R&G Faserverbundwerkstoffe GmbH), glass fiber paper (Glasvlies standaard 35gr, 35 g/m^2, h = 0.24 mm, GAMMA) and stainless steel mesh (RVS gaas, 685 g/m^2, h = 0.37 mm, Dutch-Rana). All four support structures can be seen in Figure 3.1.

Glass fiber paper is included as it contains better mechanical stability than the carbon fiber paper, while inexpensive and in a desirable porous sheet form. The drawback of glass fiber paper as a support structure is that it is non-conductive. Within this project the viability of incorporating a non-conductive support structure is investigated. The size of the produced electrodes is larger than what is common in other works (125 mm x 90 mm), so that the scale-ability of the manufacturing process can be addressed.

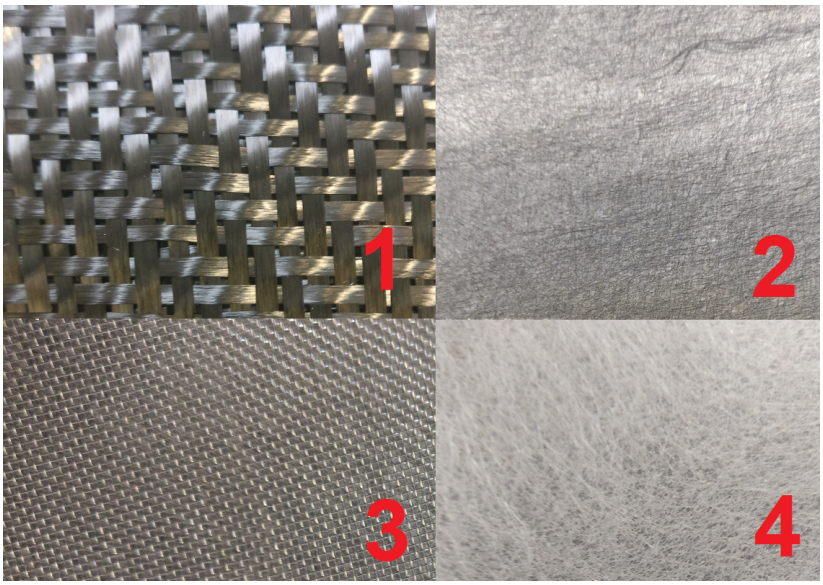

Figure 3.1: Surface appearance of the support structures used: carbon fiber (1), carbon fiber paper (2), stainless steel mesh (3), glass fiber paper (4).

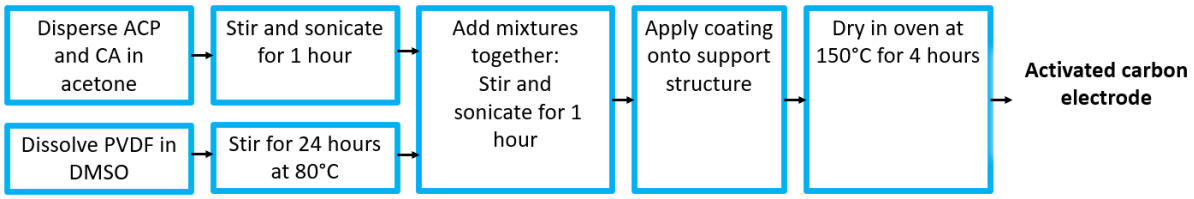

Figure 3.2: Flowchart of manufacturing process.

Figure 3.2 details the steps taken in the process of manufacturing the electrodes. The coating method applied is dip coating. Interestingly, dip coating is not mentioned in the literature as a method for producing activated carbon electrodes, however, it provides the advantage to coat uniform thickness onto both sides of the support structure at once and the thickness is easily controlled by dipping multiple times if necessary. As the electrodes will be tailored for MC-CDI operation, the aim of the production process is to achieve isotropic salt adsorption behavior. More specifically, we would like the electrodes to behave similar, irrespective of the side the salt approaches the electrode. Therefore, it is assumed coating both sides simultaneously is preferred.

Each batch of coating is prepared using 30 g of solid components and 320 ml of acetone and DMSO combined. This amount suffices to coating eight supports, which have already been cut in the right shape. To prepare the coating, the ACP and CA are dispersed in 200 ml acetone and sonicated (Cole-Parmer, Ultrasonic Processor) for one hour in order to break down any agglomerates and aggregates into individual particles. Separately, the PVDF is dissolved in 120 ml DMSO and stirred for 24 hours at 80°C to ensure homogeneity. Next, the mixtures are combined and stirred for 30 minutes and sonicated for another hour. After these steps the coating is ready for use and is poured into the coating bath, the support structures can then be submersed to apply the coating. After the coating has been applied, and left to dry to the air for 15 minutes, the electrodes are put in the oven to dry for 4 hours at 150°C to ensure all solvent is evaporated. In between dips, if necessary, the electrodes are dried in the oven for 30 minutes at 150°C.

The composition of the coating can differ per batch to deliver different coatings, thus different electrodes. The coating types used in this project are shown in Table 3.1. The proposed coating composition ratio by literature is 8:1:1, for ACP:CB:PVDF respectively, this coating is frequently used in fb-CDI. In this project it is tried to make an electrode with 5% binder, this is the mass percentage for the highest capacitance using PVDF as binder [71]. Next to these two coatings the 7:1:2 coating is applied to quantify the difference in using less ACP and more binder in respect to the 8:1:1 electrode. The coatings high in Vulcan XC-72 are investigated because it is assumed that for MC-CDI operation it is possible that the electrosorption process taking place on the outer surface of carbon particles can be beneficial for MC-CDI operation. The hypothesis is that the ions adsorbed onto the outer-surface areas, instead of inside-pore areas, are more easily desorbed into a specific direction.

Table 3.1: The coating compositions applied. Solid w% indicates the weight % of the component regarding the total solids weight used in the coating.

Coating Type	Solid w% ACP	Solid w% VULCAN XC-72	Solid w% PVDF
1	82.5	12.5	5
2	80	10	10
3	70	10	20
4	50	40	10
5	40	40	20

3.2. Experimental Methods

After manufacturing the electrodes, the performance is evaluated and compared amongst each other and literature. The electrodes are put in an in-house build CDI cell which is operated using an Arduino microcontroller that communicates with the pumps, an relay board as well as current-sensing modules. The electrodes are examined using cyclic voltammetry and salt adsorption measurements (SAM). The CV and SAM experiments are performed in a two electrode fb-CDI cell in order to best compare the results to literature and simulations. In addition to these measurements the functionality of the electrodes is displayed in MC-CDI operation. Moreover, to better characterize the electrodes build, a surface and pore size analyzer (Micromeritics Inc., TriStar II 3020) is used to obtain pore size distribution and specific surface area via the Brunauer-Emmett-Teller method.

3.2.1. fb-CDI Cell Design

The configuration of the two electrode fb-CDI cell is shown in Figure 3.3. Two plexiglass plates sandwich two electrodes together. The electrodes are spaced by the nylon spacer and rubber gasket, allowing for flow between the electrodes. Between the electrodes and the plexiglass a blind rubber gasket is positioned. Two titanium strips are sticked onto each blind gasket, functioning as current collectors. Around each electrode a plastic gasket is put, to accommodate part of the clamping force and preventing squashing of the electrode. The holes within the gaskets, electrodes and plexiglass allow for in- and outflow. The multitude of inlets and outlets enables to build a MC-CDI cell, in which the choice of the gasket allows for inflow of the solution at different levels of the cell. The configuration of the MC-CDI cell is shown next to the fb-CDI cell in Figure 3.3.

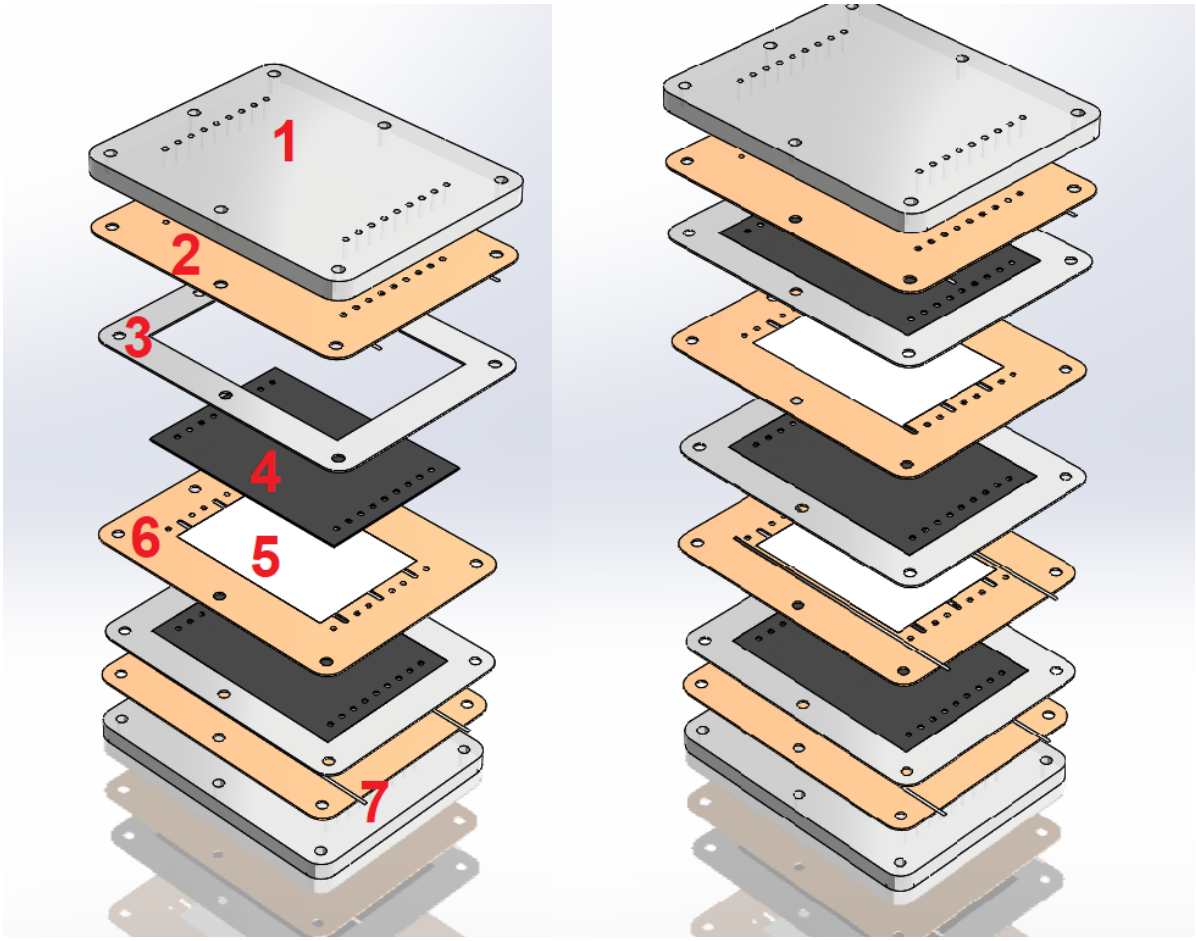

Figure 3.3: Exploded view of the fb-CDI cell (left) and the MC-CDI cell (right). Both cells are made from the same components, however note that the two rubber gaskets used in the MC-CDI cell are not the same. The components are: plexiglass (1), blind rubber gasket (2), plastic gasket (3), carbon electrode (4), nylon spacer (5), rubber gasket (6) and the titanium current collector (7).

3.2.2. Electrode Performance Evaluation

The salt adsorption measurements are performed using the setup shown in Figure 3.4, and is displayed as a flow diagram in Figure 3.5. The setup is operated in a closed loop, circulating the solution (1 liter) through the setup. The pathway of the solution starts in the storage vessel (1). From the storage vessel the solution is drawn into the CDI cell (2). The inlet of the cell can be seen at the top of the cell. The outlet is positioned at the bottom of the cell, therefore cannot be seen in the photo. After the CDI cell the solution is forced through the micro peristaltic pumps (Bartels mikrotechnik Quad kit, 3& 4), these are positioned behind the Arduino microcontroller and relay, therefore cannot be seen in the photo. The pumps pump the solution into the sample point (15). Within the sample point a conductivity sensor is put (Lutron CD-4307 Conductivity Meter, 14), allowing for effluent conductivity measurements. From the sample point the solution trickles back into the reservoir.

The charging/discharging process and the pumps are controlled by the Arduino microcontroller (6). The Arduino unit is powered from the net and the electrodes are powered using a power regulator (7). During the experiments the power supply is set to maintain a constant electrostatic potential difference of 1.2 V. The Arduino microcontroller operates a relay (8) to allow the electrodes to be charged in both polarities whenever desired. The current/voltage sensor (INA219,10) is used for current and voltage measurements with data collection in the SD-card (9).

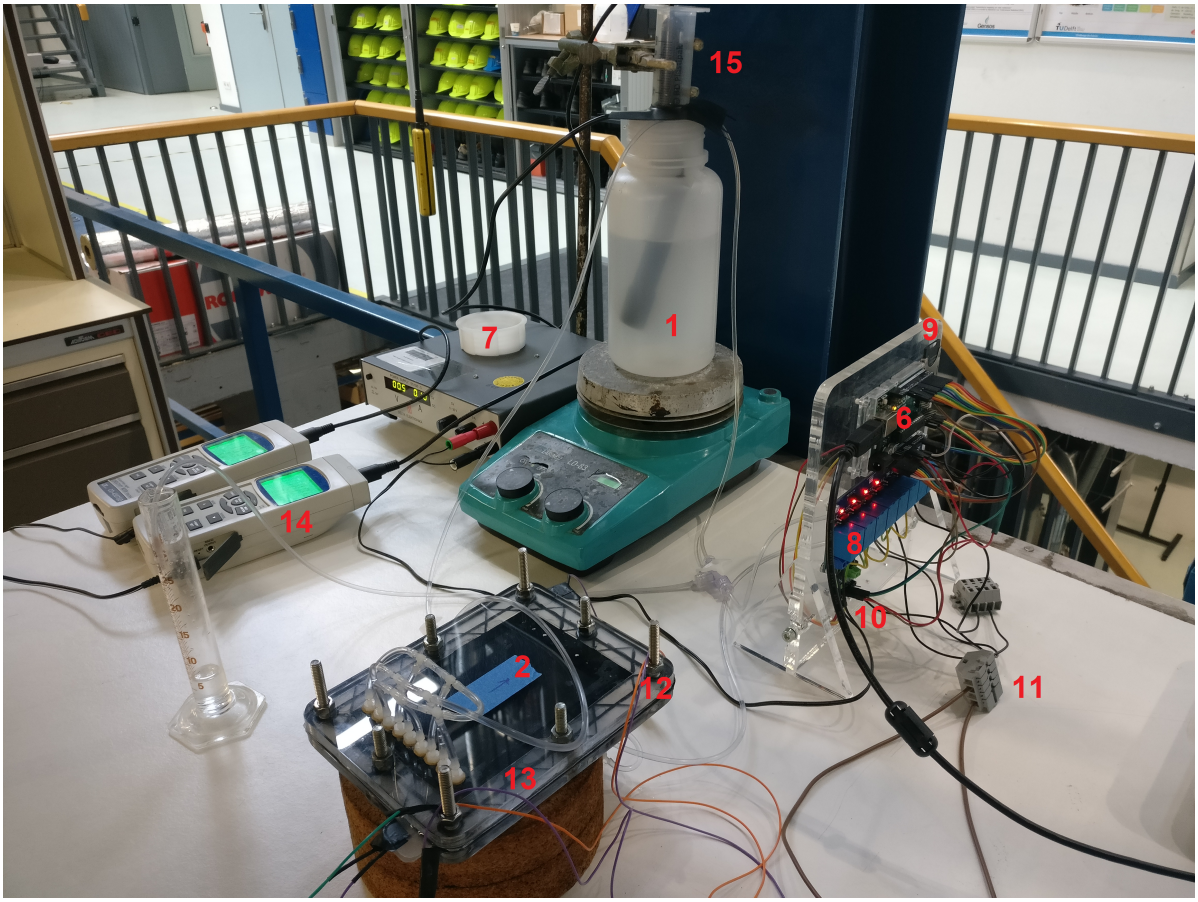

Figure 3.4: Experimental setup for completing salt adsorption measurements. The components are detailed in Figure 3.5.

Testing the salt permeability of the electrodes is completed using the setup in Figure 3.6. Here the MC-CDI cell using 3 electrodes is fed by two inlets. The sources to these inlets are two reservoirs with different salt concentrations. Each channel is connected to its own pump, the pump forces the solution through the cell back to its respective reservoir, circulating the solution. Before the solution enters the reservoir it first passes through the concentration sample point before it trickles back into the reservoir. This setup is used to measure the permeability of the electrodes. In this setup the electrodes are also subject to a MC-CDI charging protocol to demonstrate the MC-CDI functionality of the electrodes.

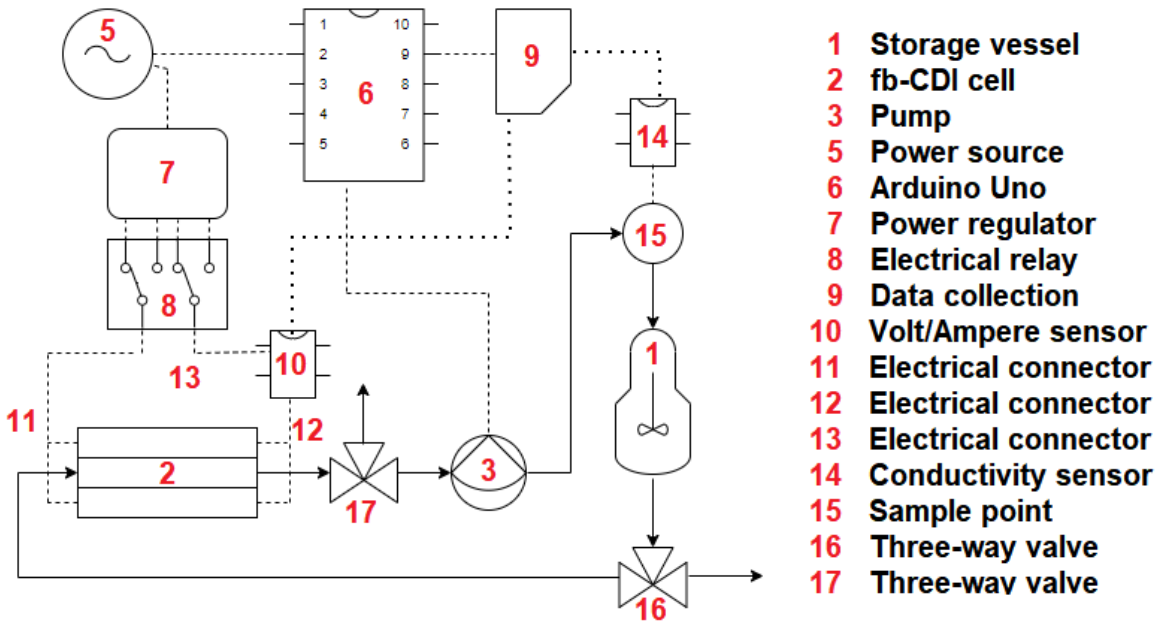

Figure 3.5: Flow diagram of the desalination experimental setup

CV measurements are completed with an inhouse-build potentiostat connected to the two electrode fb-CDI cell. During the CV measurement, one of the electrodes is to be evaluated, this electrode is called the working electrode. The other electrode within the cell functions as an electron reservoir, this electrode is the counter electrode. An Ag/AgCl reference electrode is used to pin down the voltage between the electrodes onto an absolute electrode potential, i.e., the voltage of the working electrode with respect to the standard hydrogen electrode. During the CV measurement a repeating triangular voltage ramp is applied to the working electrode. While the voltage changes in time the resulting current is measured. This current can be plotted versus the potential difference between the working electrode and reference electrode. The concentration within the fb-CDI cell during the CV measurements is 1.0 M NaCl to ensure enough ionic charge is present within the cell to allow for cycling a voltage range of 1.2 V [20]. The large concentration also decreases ohmic drop within the solution which allows the reference electrode to be positioned outside the fb-CDI cell. Most favourably, the reference electrode should be positioned closely to the working electrode, this way the ohmic drop due to ion currents in the water phase is minimized, thereby avoiding polarization of the reference electrode and hence keeping the applied potential distribution between the working electrode and reference electrode stable. Increasing the concentration of the solution is a secondary method of decreasing ohmic drop, allowing to circumvent incorporating the reference electrode within the fb-CDI cell.

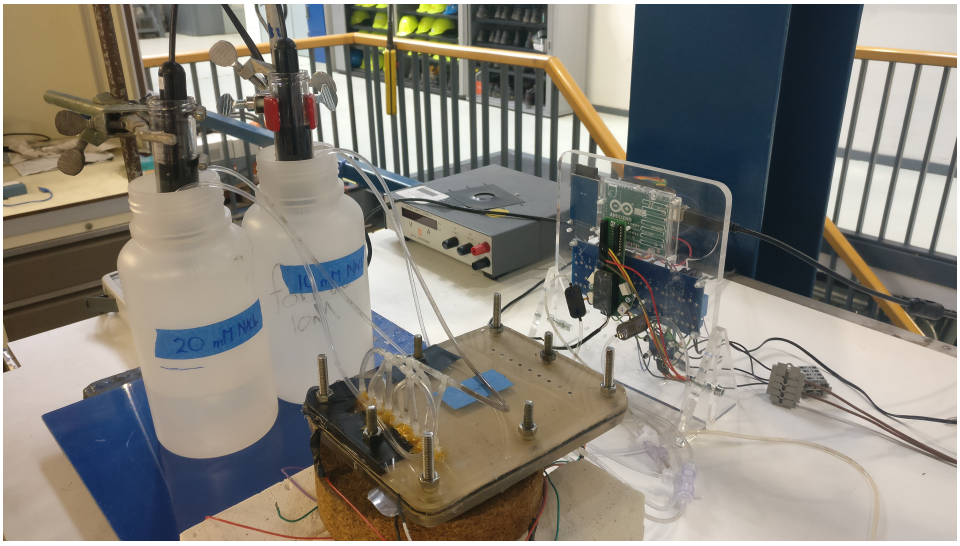

Figure 3.6: Experimental setup for testing electrode permeability in MC-CDI operation. Two different reservoirs are attached to a separate flow channel each. Each channel is provided its own pump that circulates the solution through the MC-CDI cell.

3.3. Modelling Electrosorption

The aim of computer simulations is to provide a deeper understanding of the effect of varying electrode properties, such as ACP content and thickness. The two-dimensional porous electrode model for CDI as formulated by Hemmatifar *et al.* is utilized [24]. This model includes coupled external electrical networks, charge conservation, and species conservation in bimodal pore structure electrodes. As a result of using the bimodal pore structure the electrode pore volume is split in macropores and micropores. In the micropores, the modified Donnan (mD) approach is employed to simulate the EDL structure and charge accumulation at the surface of the electrodes. The mD model allows for a robust treatment of porous electrode volumes, which include a significant amount of pores with a diameter in the order of, or smaller than, the Debye length and hence overlapped EDLs. The macropore volume is assumed to dominate ion transport throughout the porous electrode and electroneutrality is assumed, thus neglecting EDL formation.

The schematic of the 2D flow-by CDI cell is shown in Figure 2.5, alongside with the boundary and interface conditions in nondimensional form. The cell consists of two porous carbon electrodes sandwiched between two current collector plates. The feed water flows in the gap between the electrodes. The gap thickness L_s is much smaller than the electrode width, this allows us to approximate the flow within the gap as Poiseuille-like. It is assumed that the gap and the electrodes are completely filled with water. Further assumptions are dilute, binary, symmetric, and univalent electrolyte. The assumptions of a binary, symmetric electrolyte allows us to use a symmetry boundary condition for spatiotemporal concentration fields and an anti-symmetry boundary condition for potential.

The model includes inlet and outlet domains sufficiently far from the electrode edges. The concentration at the inlet is set uniform and zero gradient is set at the outlet. At both the inlet and outlet zero electric potential is assumed. Other boundary and interface conditions are zero mass and current flux across side walls of the inlet and outlet and across the outer boundaries of the electrodes, advective boundary condition for concentration at the outlet, continuity of concentration and potential as well as salt flux and electric current at the electrode solution interface. The interface conditions for salt flux and electric current at the solution side are multiplied by p_M to correct for the effect of macropore porosity. Furthermore, the assumptions of a binary, symmetric electrolyte allows us to use a symmetry boundary condition for spatiotemporal concentration fields and an anti-symmetry boundary condition for potential.

All simulations are performed in COMSOL Multiphysics. The model is implemented using transport of diluted species and equation-based modelling interfaces. The model contains three free parameters, a non-electrostatic adsorption parameter, the volumetric ionic charge capacitance of the electrodes and the micropore porosity. The micropore porosity is the volume fraction of the pores contributing to ion adsorption. These values are estimated by minimizing the error between experiments and model results. Using the fitted free parameters a number of parameter studies are completed. In this work values of micropore porosity, lumped electrical resistance and electrode thickness are varied.

4

Results & Discussion

4.1. Electrode Manufacturing

During this project 60 electrodes have been manufactured, comprising of 19 different types. Types of electrodes are distinguished by manufacturing method, coating composition and support structure. Only six of these types have been evaluated, the others failed to result in functional electrodes.

The six types of electrodes evaluated by means of cyclic voltammetry and salt adsorption measurements are indicated as GF811, GF712, GF442, CF811, CF712 and CF442. The first two letters refer to the support structure used within the electrode, as can be read, only two support structures result in usable electrodes, i.e., glass fiber paper and carbon fiber. The stainless steel mesh corroded during CDI operation and the carbon fiber paper disintegrated as the coating was applied. The number sequence in the electrode type refers to the ratio of coating composition applied onto the support structure. The first number represents the amount of activated charcoal, the second number indicates the amount of carbon black (Vulcan XC-72) and the third number declares the amount of binder used. The number sequence can thus be read as a ratio 8:1:1, 7:1:2 and 4:4:2.

The coating that only contains 5% binder results in a too mechanical unstable electrode and large parts of the coating exfoliate from the support structure. The coating containing 50 % carbon black results in electrodes with many cracks, as can be seen in Figure 4.2. In order for a electrode to be made using a large amount of CB, such as Vulcan XC-72, a weight percentage of 20% binder was utilized to provide gelation-driven crack prevention.

Structures before application of the slurry have a thickness of GF $\approx$ 0.26 mm and CF $\approx$ 0.24 mm. Practical active electrode layer thickness ranges from 40 μm to 300 μm, therefore the coating is applied with the aim to deliver 0.5 mm thick electrodes. The possibility to dip the electrode multiple times to increase the thickness is utilized to get to a thickness just over 0.5 mm. In all cases, except for GF442, this was reached with limited overshoot of approximately 0.06 mm. In the idealized world, GF442 should have been submersed one more time, unfortunately this did not happen. In retrospect, it would have been possible to submerse the latter electrodes one more time to approach the desired 0.5 mm. For future experimental studies it is therefore advisable to leave additional coating for possible use, later in the manufacturing process. Mean electrode thickness and mean electrode mass data can be seen in Table 4.1. The appearance of the CF712 and GF712 electrode can be seen in Figure 4.1, all other electrodes share similar appearances.

The dip-coated electrodes resulted in uniform crack free smooth electrode surfaces. It was observed that as the binder content increased the coating became more viscous. More surprisingly, a strong correlation between the weight fraction of carbon black and the viscosity can be observed. The significant increase in viscosity becomes most apparent after sonification. It may be speculated that after one hour of sonification all agglomerates are broken down into aggregates or individual particles. As the mean particle size decreases during the process the packing density changes. As the effective packing fraction of the loose particles increases when the aggregates brake up, this yields a more viscous suspension overall [49].

Table 4.1: The six electrodes build for evaluation, the amount of dips into the coating bath, mean thickness h (calculated from 8 separate measurements) and mean electrode mass m.

Electrode	w% ACP	w% VULCAN	w% PVDF	Number of Dips	h (mm)	m (g)
GF811	80	10	10	4	0.61	2.16
GF712	70	10	20	2	0.55	2.16
GF442	40	40	20	2	0.45	1.72
CF811	80	10	10	4	0.53	2.79
CF712	70	10	20	2	0.54	2.96
CF442	40	40	20	1	0.56	3.16

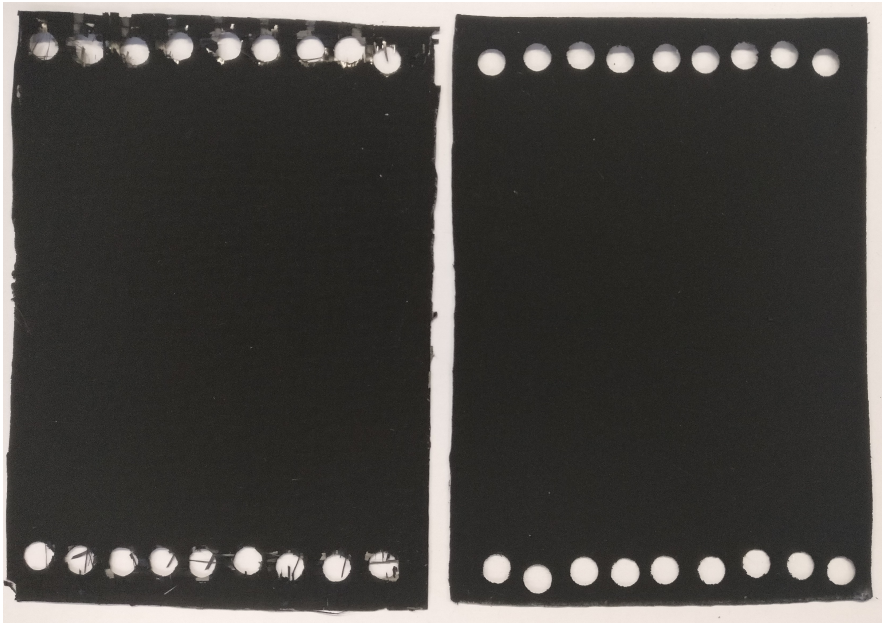

Figure 4.1: CF712 electrode (left) and GF712 electrode (right). The coating is applied onto the support structures and the electrodes have been dried for 4 hours at 150°C. The electrodes are shown to be very smooth and uniform. Manufacturing the holes in the electrodes show to have caused some minor exfoliation on the carbon fiber electrode.

4.2. BET Surface Analysis

During the BET measurements the sample is supplied with more and more nitrogen gas that it can adsorb, in steps. Each step the sample is supplied with a calculated amount of N_2 after which the pressure within the sample tube is observed. As the sample adsorbs the N_2, the pressure within the sample tube decreases. From this pressure change the amount of adsorbed N_2 is determined and a data point is created. During the BET measurements, a remarkable difference in time duration of the measurement was observed between the raw materials and electrode coating. The pressure decreasing process is what determines the measurement duration. In the case of the raw ACP the duration for the N_2 to be adsorbed in the sample was around a stable four minutes per data point. While comparing electrode material with its raw components, it turns out that this time is, now and then, approximately twice as large. The hinderance of N_2 in entering the pores can reflect the blockage of pores by the polymer binder.

Table 4.2 shows the BET surface analysis results of the raw activated charcoal and carbon black, together with four of the six manufactured electrodes. A BET SSA of 930 m^2/g is determined for the raw activated charcoal. This is relatively close to the value of 880 m^2/g as published in literature [46]. From this result it may be confirmed that the supplier provides a reasonable stable product. The surface area of Vulcan XC-72 is 230 m^2/g, which is a surface area that can be predominantly attributed to the outer area of all particles. On the other hand, it could also be confirmed that the carbon black contains a significant fraction of macropores. Here, the presence of macropores is assumed to be a reflection of the outer-surface area of the individual particles within agglomerates that is recognized as macropore surface area.

As the raw materials are bound together in the coating it can be seen that the remaining surface area is

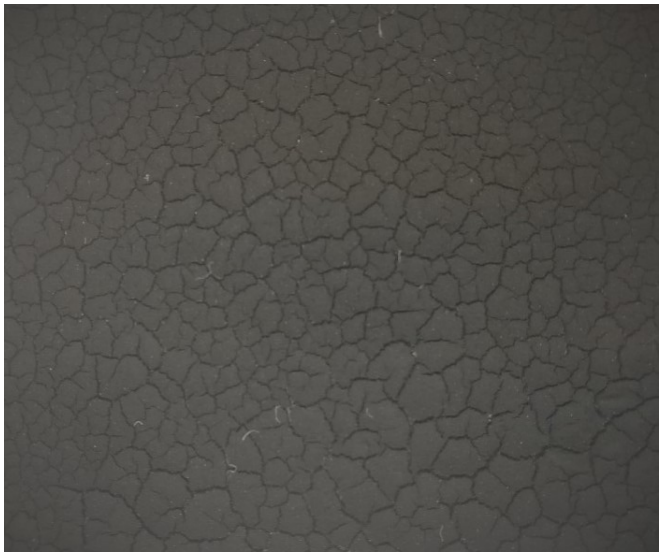

Figure 4.2: Cracked coating film of carbon electrode. Cracks result of residual stress release from colloidal films made by the evaporation of colloidal droplets containing nano particles. Capillary pressures generate tensile stresses normal to the coating film.

drastically reduced. The BET SSA of the GF811 electrode is determined at 390 m^2/g. This significant decrease can be explained through introduction of a support structure with extremely low surface area per unit mass as well as the blocking of pore openings by the PVDF-binder.

Upon analyzing the difference between the GF811 and the GF712 electrode, it can be seen that the 10% decrease in ACP and 10% increase in binder decreases the SSA to 330 m^2/g. Similarly, the BET surface is even further lowered as the coating composition changes to 4:4:2 (180 m^2/g). The BET surface of the CF712 is lowest of all measured electrodes due to the higher support structure mass density (140 m^2/g). In case the mass of the support structure is left out of the BET SSA determination it can be seen that the BET surface areas of the GF712 and the CF712 electrode approach each other much more closely, 410 m^2/g to 350 m^2/g.

Table 4.2: BET Surface Analysis of the raw carbon powders used and four of the in-house build electrodes, indicating that the activated carbon used is a typical commercial microporous carbon. The pore volume indicates the volume of pores between 1.7 nm and 300 nm, micropore volume indicates the amount of volume of pores smaller than 1.7 nm.

Electrode	**BET SSA, full electrode** (m^2/g)	**BET SSA, coating** (m^2/g)	**Micropore Volume** (cm^3/g)	**Pore Volume** (cm^3/g)
Activated Charcoal	930	-	0.29	0.48
Vulcan XC-72	230	-	0.04	0.41
GF811	390	480	0.11	0.28
GF712	330	410	0.10	0.23
GF442	180	240	0.05	0.19
CF712	140	350	0.04	0.11

Figure 4.3a shows the cumulative pore volume of pores from 1.7 nm to 100 nm. On the other hand, Figure 4.3b shows the gradient of the cumulative pore volume, which is a measure of the change in pore volume as larger and larger pores are included in the determination of the cumulative pore volume. From this curve the pore size distribution can be derived. From the observation that Figure 4.3b starts at its maximum for smallest pore widths, it can be deduced that micropores contribute significantly to the overall pore volume. Thus, as the micropores are small with little volume it can be said that there are a significant amount of micropores. The peak at 30 nm shows that the numbers of these pores increased a bit. After the peak it can be seen that the amount of pores with diameter larger than 30 nm drops significantly.

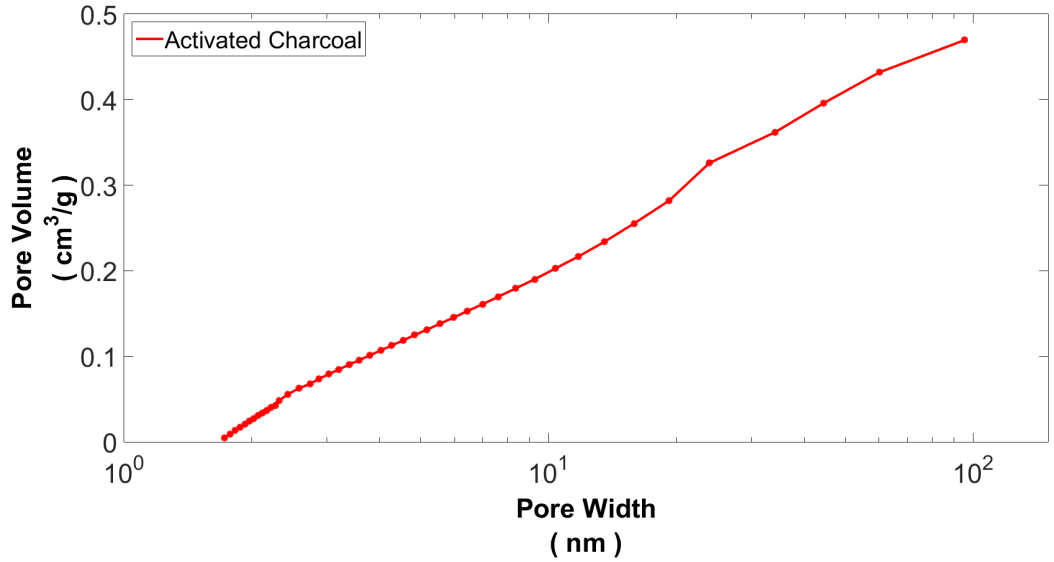

(a)

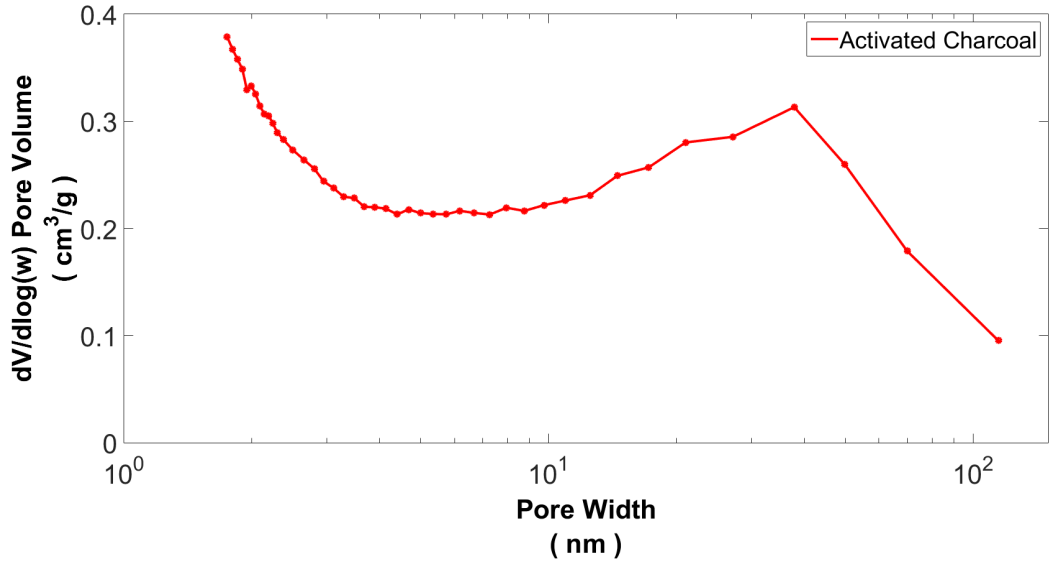

(b)

Figure 4.3: (a) Cumulative pore volume of pores between 1.7 nm and 100 nm of the activated charcoal used. (b) The curve is determined from the gradient of the cumulative pore volume and provides an indication of the pore size distribution.

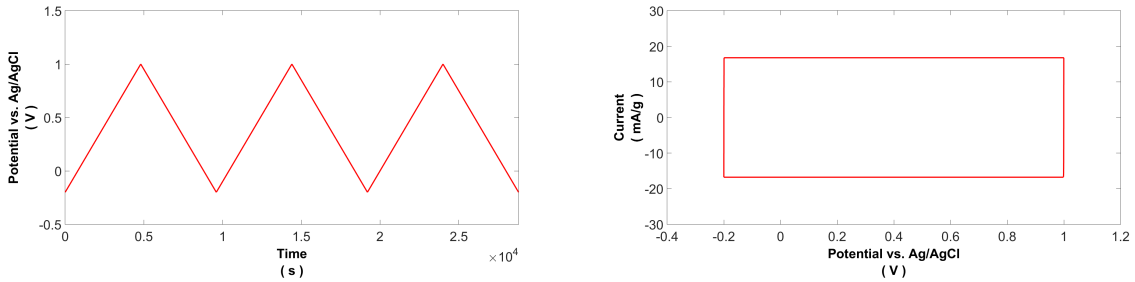

(a) (b)

Figure 4.4: (a) Potential profile applied to the working electrode during CV cycling. (b) Simulated current response for an ideal, frequency independent capacitor.

4.3. Cyclic Voltammetry

Cyclic voltammetry is completed to determine the capacitance of the electrodes. The capacitance is a performance indicator of CDI systems and is directly related to the functioning of the electrodes installed. Capacitance is a measure for the electric charge that can be stored in the electrode. This charge is one part of the electrical double layer, with the other part being the adsorbed ionic charge. The cyclic voltammetry setup is discussed in Chapter 3. During the CV measurement a repeating triangular voltage ramp is applied to the working electrode, see Figure 4.4a. While voltage changes in time the resulting current is measured. In case of an ideal circuit, the resulting current that is expected for an ideal, frequency independent capacitance can be derived from the relation of charge (Q), voltage (U) and capacitance (C) as

$$Q = CU. \tag{4.1}$$

Upon taking the time-derivative of the latter equation, it can be observed that the change of charge with time scales with the change in potential with time, $\dot{Q} = C\dot{U}$. $\dot{U}$ is constant as the triangular voltage ramp has a linear profile and only changes in sign at the switching potential. As $\dot{U}$ is constant, $\dot{Q}$ is constant and thus the current (I) remains constant, following from $Q = It$. Therefore, if the current is plotted versus the potential difference between the working and reference electrode, a rectangular shape is expected, see Figure 4.4b.

Figure 4.5a shows experimental CV data for the GF811 electrode, displaying the sweeprates 10 mV/s, 7.5 mV/s, 5 mV/s and 2.5 mV/s. Figure 4.5b displays slower sweeprates: 2.5 mV/s, 1.0 mV/s, 0.5 mV/s and 0.25 mV/s. The cycles start at 1.0 V and is linearly decreased to -0.2 V. At -0.2 V the sweep direction is reversed and linearly increased back to 1.0 V. The measured current of the lower sweeprates is smoothed by the use of a moving average filter.

It can be seen that the curves in Figure 4.5a are not rectangular shapes. Looking at the curves in the figure shows a gradual decrease in current measured as the electrode is swept down in potential and a gradual current increase is observed as the electrode is swept up in potential. The measured current does not instantly change sign upon reversing the voltage sweep direction, which is expected for an ideal frequency independent capacitor. Nonetheless,it is not problematic that the current response is not rectangular, as we are prepared for some non-idealities. In Figure 4.5b it can be seen that decreasing the potential sweeprate results in a more and more rectangular shape. Below, we will focus on the sweeprate of 0.25 mV/s, as at this slow sweep rate the current response is closest to rectangular. This curve is plotted separately in Figure 4.5c, where it can be more clearly reviewed.

The 0.25 mV/s curve is close to rectangular, however, the curve clearly does not align itself perfectly with the expected response. As the cycle is followed clockwise, starting from 1.0 V, it can be seen that as the sweep direction reverses the current does not instantly turn negative. The current gradually turns negative in a rounded slant. The same behaviour is observed at the switching potential of -0.2 V. Again the current does not instantly change sign, however, changes in a rounded gradual fashion. The slant that is observed can be explained by the charging resistance of the electrode. More specifically, the electrode is not an ideal capacitor and a series resistance is present (R_s). Looking at the difference between the different sweeprates, it can be seen that a larger sweeprate results in higher current densities. This is easily understood from Equation 4.1, the current is proportional to the sweeprate. Due to the higher current densities the slant due to resistance to charging becomes more pronounced as a larger current is disrupted by this resistance. It is therefore more

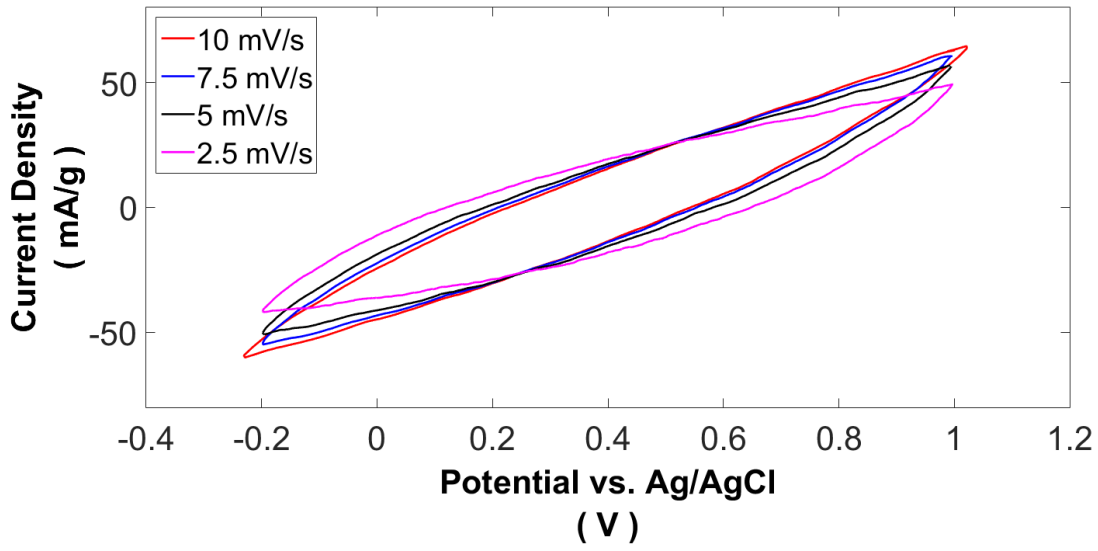

(a)

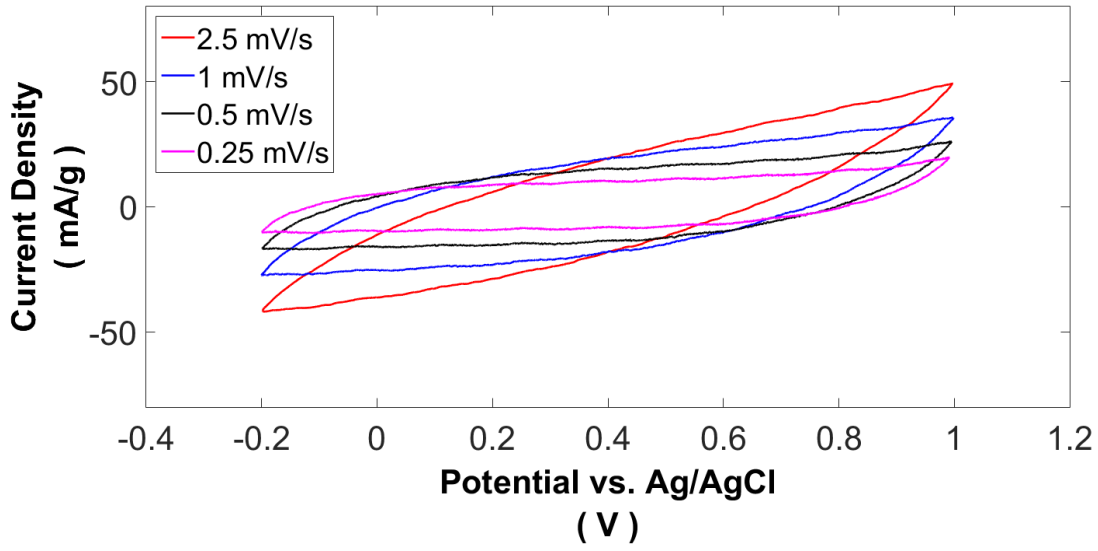

(b)

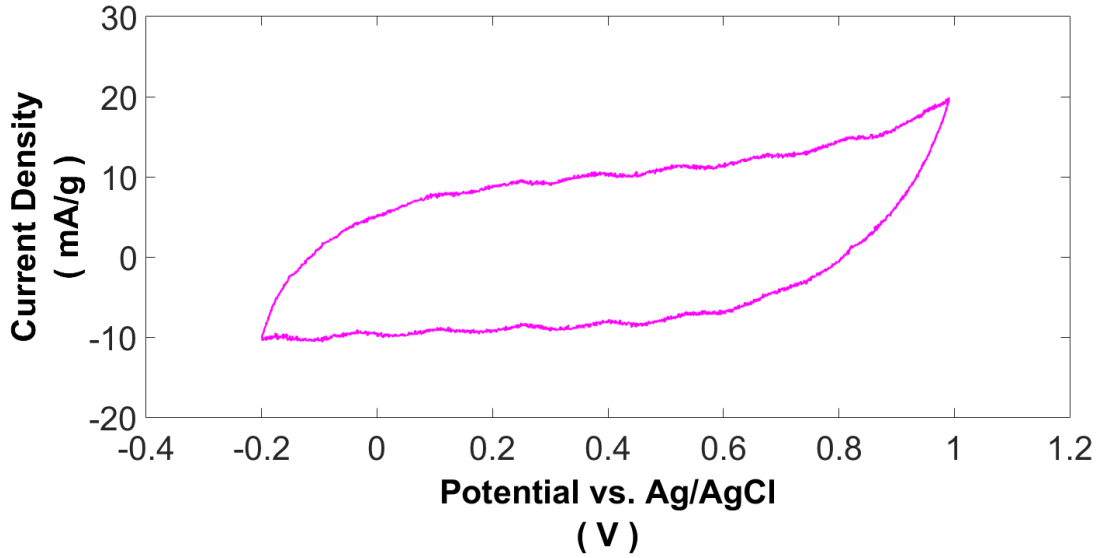

(c) CV data for the GF811 electrode in 1.0 M NaCl and 0.25 mV/s.

Figure 4.5: (a) CV data for the GF811 electrode in 1.0 M NaCl displaying the sweeprates: 10 mV/s, 7.5 mV/s, 5 mV/s and 2.5 mV/s. (b) CV data for the GF811 electrode displaying the sweeprates: 2.5 mV/s, 1.0 mV/s, 0.5 mV/s and 0.25 mV/s. (c) CV data for the GF811 electrode in 1.0 M NaCl and 0.25 mV/s.

useful to examine the electrodes using a slow sweeprate, as at a slow sweeprate the current behaviour is not fully dominated by this resistance to charging.

Next to the rounded features of the 0.25 mV/s curve, another major deviation from the ideal rectangular shape emerges as the current starts increasing towards the end of the oxidizing sweep, this is discussed in more detail further below.

In Figure 4.7a and Figure 4.7b compares different electrodes based on a sweep rate of 0.25 mV/s. Moving average current values are used in the calculations and graphs. The differential capacitance is calculated using

$$C = \frac{I}{\upsilon m}, \tag{4.2}$$

where υ is the sweeprate and m is the mass of the working electrode. All electrodes show a close to rectangular shape with resistance to charging and a peak at the end of the oxidization sweep. From the two graphs it can be seen that the area enclosed by the curves is larger for the glass fiber paper electrodes compared to the carbon fiber electrodes, indicating a larger specific capacitance. In order to determine the capacitance of the electrode the mean differential capacitance is calculated, this integral capacitance is calculated as

$$C = \frac{\mathrm{A_{curve}}}{2m\upsilon(U_2 - U_1)}, \tag{4.3}$$

where $\mathrm{A_{curve}}$ is the area enclosed by the CV curve in units AV and $U_2 - U_1$ is the total voltage range. The results for integral capacitance values are put in Table 4.3. In the second column the capacitance per total electrode mass is presented, which is the agreed upon convention. The calculated capacitance for the glass fiber paper electrodes resulted in 31.44 F/g, 26.88 F/g and 16.22 F/g, for the electrodes GF811, GF712 and GF442 respectively. The capacitances for the carbon fiber electrodes are determined to be 16.18 F/g, 15.62 F/g and 7.72 F/g, for the electrodes CF811, CF712 and CF442 respectively.

The largest capacitance for GF811 is in line with the largest fraction of activated charcoal and minimum amount of binder material. The activated charcoal provides more space for ion adsorption and the minimum amount of pores is blocked. Specifically, the difference of minus 10% ACP and an increase of 10% binder material results in a 5 F/g decrease in capacitance. The GF442 exhibits the lowest capacitance by far, which underscores the importance of ACP in achieving high capacitance values.

A similar relationship, as described above, is found between the carbon fiber electrodes, however, all the capacitance values are found to be significantly lower. The lower capacitance values can be explained by the large mass difference in support structure. This structure takes up only 20% of the total mass in the glass fiber paper electrodes, opposed to 60% within the carbon fiber electrodes. The larger support structure mass reduces the gravimetric capacitance. To enable a better comparison between both support materials, we continue by comparing the capacitances based on the mass of the coating only, which can be seen in Table 4.3, column Mass_c C. For all electrodes, except the 442 electrodes, it is even observed that the CF electrodes exhibit a higher capacitance per mass coating as compared to the GF electrodes. This is the benefit of more electrical conductive electrodes, when *only* the coating mass is considered. This is an immediate benefit of the electrically conductive support, which enables larger currents and, thus, larger sweeprate-dependent capacitances.

In literature PVDF-bonded electrodes are published reaching up to 80.3 F/g, much higher than the electrodes manufactured in this project. One explanation for the relatively low capacitance is the cell design used. More specifically, the electrode within the cell is covered by rubber for a significant part. Thus, not all area of the electrode can project itself onto the opposite electrode. Figure 4.6 displays the area that can most actively take part in electrosorption, this area is called the projected area (Area_p). To enable a better comparison between our capacitance values and the ones found in literature, we therefore proceed by calculating the capacitance using only this part of the electrodes results in Table 4.3, column Area_p C. Indeed, if both factors are considered together the values approach the numbers from literature much closer and therefore it seems reasonable that support mass and edge-area effect play a major part in the deviation from literature (Table 4.3, column Area_p & Mass_c C.).

Table 4.3: Electrode electrical capacitance values calculated from CV data. Here, the specific capacitance is calculated as the integral capacitance measured from the area enclosed by the cycle. The concentration of electrolyte was 1.0 M NaCl and the sweeprate of 0.25 mV/s. The error margins shown originate out of possible mass difference between working electrode and counter electrode. The capacitance values are determined using the mean of two electrodes installed in the CDI cell. The error margin is determined out of the use of minimum and maximum electrode mass, as it was not noted which electrode functioned as working electrode or counter electrode.

Electrode	**C (F/g)**	**Area$_P$ C (F/g)**	**Mass$_c$ C (F/g)**	**Area$_P$ & Mass$_c$ C (F/g)**	**C (F/cm^2)**	**Area$_P$ C (F/cm^2)**
GF811	31.44 ±0.81	49.37 ±1.27	38.99 ±1.00	61.23	0.60 ±0.15	0.94 ±0.02
GF712	26.88 ±1.12	42.21 ±1.75	33.34 ±1.39	52.35	0.52 ±0.02	0.81 ±0.03
GF442	16.22 ±0.41	25.47 ±0.65	21.42 ±0.55	33.64	0.25 ±0.006	0.40 ±0.01
CF811	16.18 ±0.64	25.41 ±1.01	43.64 ±1.74	68.53	0.40 ±0.016	0.62 ±0.03
CF712	15.62 ±0.37	24.52 ±0.58	38.27 ±0.90	60.10	0.41 ±0.01	0.65 ±0.02
CF442	7.72 ±0.19	12.12 ±0.19	17.35 ±0.42	27.24	0.21 ±0.005	0.34 ±0.01

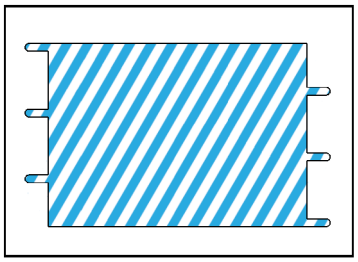

Figure 4.6: Graphical representation of the projected area of the electrode. The white area is used for current collectors and sealing the channel and is not used for ion absorption.

In an attempt to deduce more information, such as resistances, from our CV data, we have modeled the electrode as a simple RC circuit. Within Figure 4.9a and Figure 4.9b the CV curve for the GF811 electrode is plotted once again. In Figure 4.9a simulated RC circuit data is added to the plot. This data is generated using QUCS circuit simulator, here a simple RC circuit is implemented, see Figure 4.8b. The value of the capacitance is set to the determined value from the CV measurement. The resistance in the RC circuit can be used to demonstrate the effect of resistance on the charging behaviour.

The dependence of the resistance to charging on R_s is clearly visible. The smallest resistance approaches the rounding behaviour observed in the experiment and the larger resistances display a smaller current and larger curvature. It should be noted that, as the RC circuit is implemented with the capacitance measured from the experiments, the capacitance resulting from the RC circuit response is lowered by the added resistance. By adding the resistance to the measured capacitance the area of the curve got smaller. If the aim is to match the areas of the curves, an iterative process could have taken place in which also the capacitance of the effective RC circuit was varied. However, it can be assumed that the area enclosed by the black curves in Figure 4.9a and Figure 4.9b should be enlarged to some degree.

Figure 4.9a shows CV response data from a circuit that has no incorporated mechanism to include Faradaic processes. In the figure it can be seen that the current starts increasing towards the end of the oxidizing sweep. Here, at positive voltages it is assumed that Faradaic reactions start taking place. As the absolute potential of the electrode hits the Faradaic redox potential of a half cell reaction it could trigger an oxidation reaction, provided that all necessary components for the reaction to occur are present, Figure 4.9a pinpoints two suspect reactions, with carbon oxidation being the main suspect, occurring as

$$\begin{aligned} C + H_2O &\rightarrow C{=}O + 2H^+ + 2e^- \\ C + H_2O &\rightarrow C{-}OH + H^+ + e^- \\ C + 2H_2O &\rightarrow CO_2 + 4H^+ + 4e^- \qquad\qquad E^0 = 0.44 \quad V \quad vs. \quad Ag/AgCl. \end{aligned}$$

The second oxidation reaction that is possible to take place, however more unlikely, is the oxidation of chlorine following

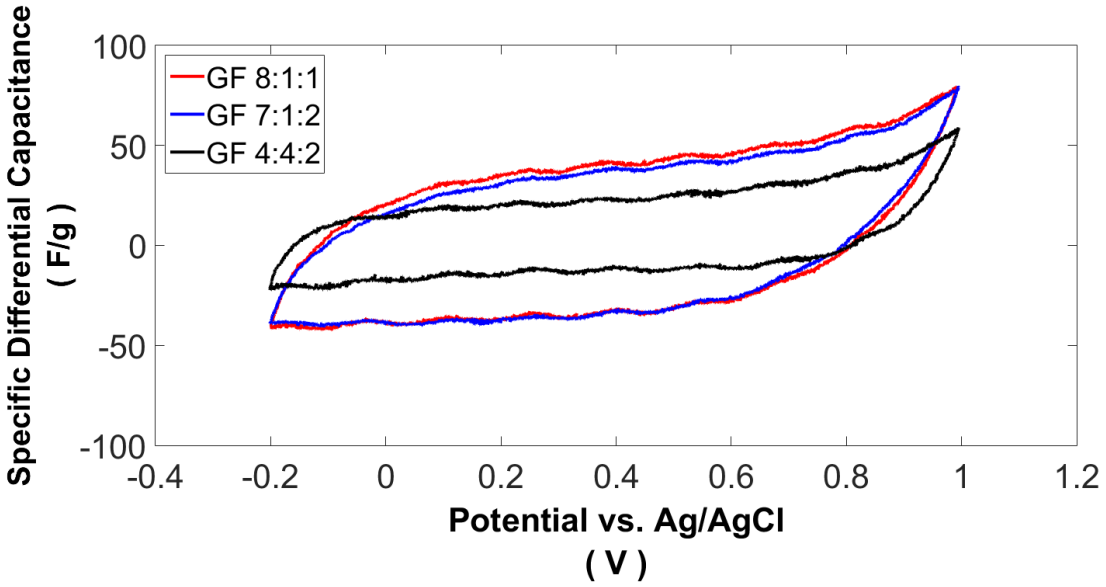

(a)

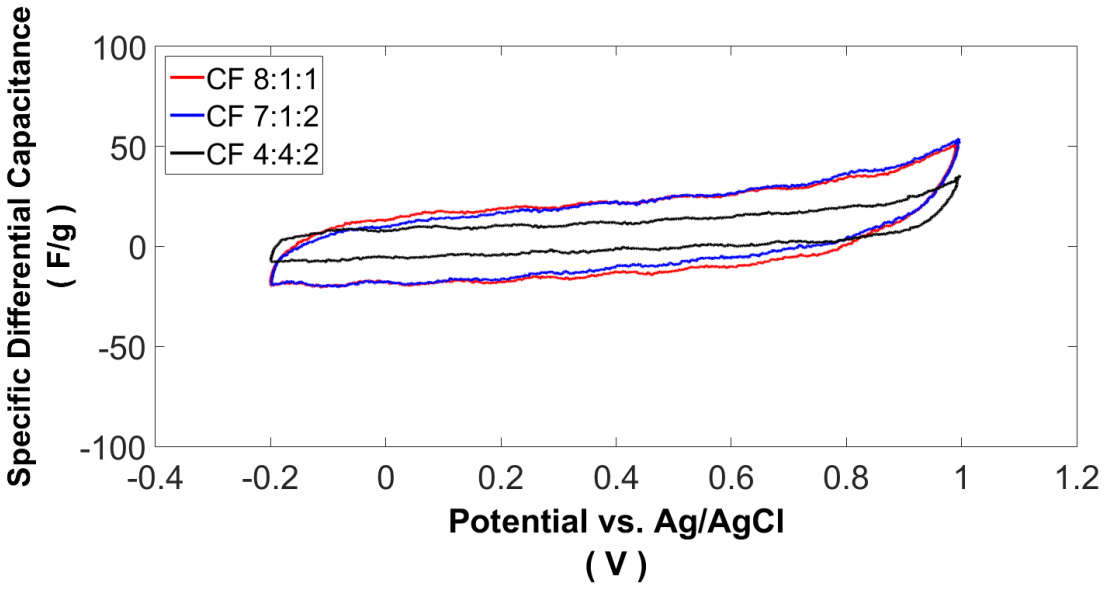

(b)

Figure 4.7: Cyclic voltammetry comparison between glass fiber and carbon fiber support materials, showing in (a) glass fiber electrodes and (b) carbon fiber electrodes. The CV measurement is executed in 1.0 M NaCl using 0.25 mV/s sweeprate.

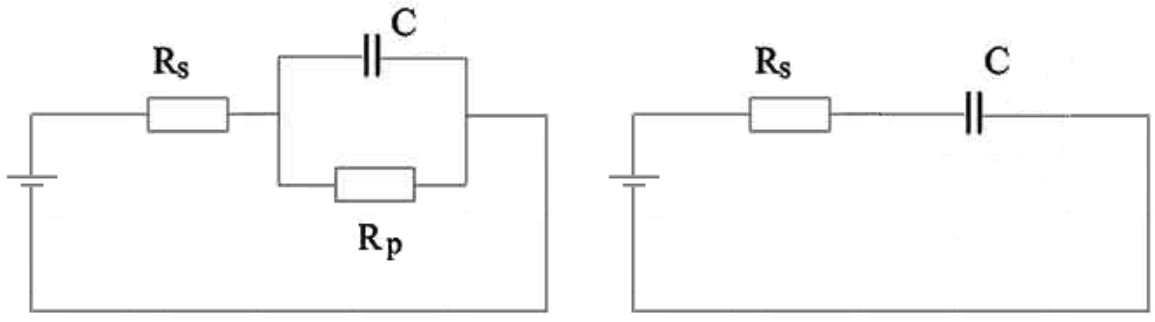

(a) (b)

Figure 4.8: Electrical circuit of the Randles cell (a) and the RC circuit (b).

$$
\begin{aligned}
2Cl^- &\rightarrow Cl_2 + 2e^- && E^0 = 1.59 \quad V \quad vs. \quad Ag/AgCl \\
Cl_2 + H_2O &\rightarrow HClO + H^+ + Cl^- \\
HClO &\rightarrow H^+ + ClO^- \\
6HClO + 3H_2O &\rightarrow 2ClO_3^- + 4Cl^- + 12Cl^- + 3/2O_2 + 6e^- && E^0 = 0.69 \quad V \quad vs. \quad Ag/AgCl.
\end{aligned}
$$

This reaction is unlikely to take place as the redox potential to produce free chlorine is not reached. The total amount of Faradaic current observed can thus be assumed to fully oxidize the carbon electrode.

The limited overshoot of the measured data as compared to the RC circuit data at the end of the reduction sweep can be attributed to insufficient fitting of the RC parameters, but possibly also Faradaic effects, in the form of

$$
\begin{aligned}
O_2 + 2H^+ + 2e^- &\rightarrow H_2O_2 && E^0 = 0.92 \quad V \quad vs. \quad Ag/AgCl \\
H_2O_2 + 2H^+ + 2e^- &\rightarrow 2H_2O && E^0 = 3.01 \quad V \quad vs. \quad Ag/AgCl \\
O_2 + 4H^+ + 4e^- &\rightarrow 2H_2O && E^0 = 1.46 \quad V \quad vs. \quad Ag/AgCl.
\end{aligned}
$$

By design, the effective RC circuit does not include effects such as Faradaic losses. The Randles cell is a circuit very similar to the RC circuit, however, has an extra parallel resistance (R_p) that can possibly account for Faradiac current. Figure 4.9b presents the experimental GF811 electrode CV data compared to simulated Randles cell data with a constant value of $R_s = 7.5\,\Omega$ and a varying parallel resistance. From the figure can be seen that the processes taking place in the activated carbon CDI electrode cannot simply be reconstructed using resistors and an ideal capacitor. Including a resistor parallel to the capacitor superpositions a linear current to the already present current response. The linear profile results from Ohm's law, however, the measured current grows non-linearly towards the end of the oxidation sweep.

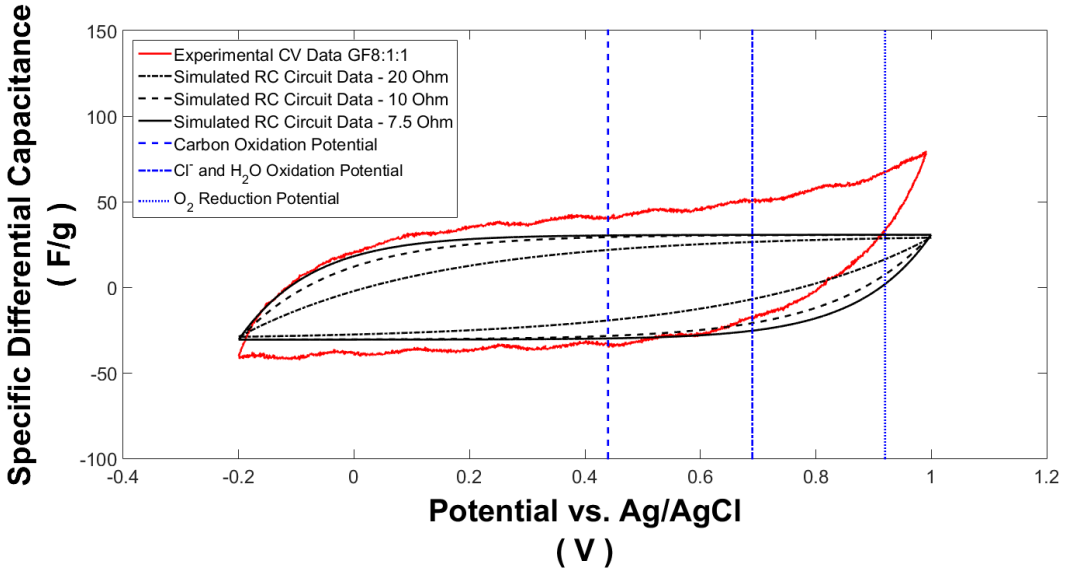

(a)

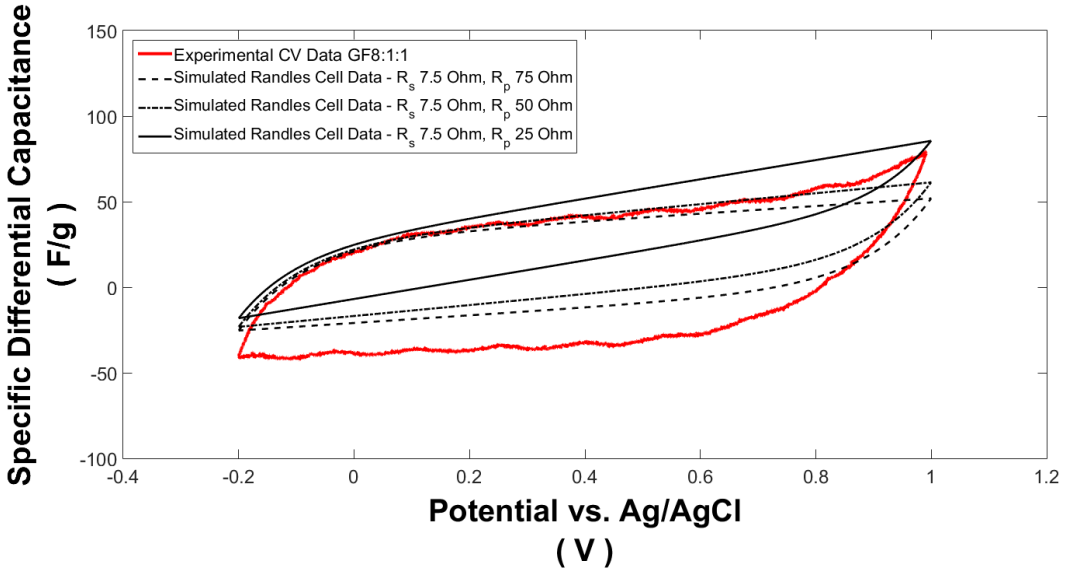

(b)

Figure 4.9: Comparison between the GF811 electrode CV curve and the simulated RC circuit data (a), using different values of R_s. The same experimental data is compared to the simulated Randles cell data in (b), using different values of R_p. The vertical blue lines are located at the redox potentials for carbon oxidation, Cl^- oxidation and O_2 reduction, corresponding to Eqs. 2.38 - 2.40,2.44 and 2.48.

4.4. Salt Adsorption Measurement

During the salt adsorption measurement the voltage between the electrodes is stepped to 1.2 V for half an hour. After this charging phase the applied electrostatic potential is removed and the electrodes regenerate by setting the voltage difference to zero, i.e., short-circuiting the electrodes. The applied voltage step and current response can be seen in Figure 4.10. The measured current spikes initially, but quickly drops off while the charging phase proceeds. Right after the change in applied voltage the driving force for electrosorption is at maximum and much of the ions already within the electrode are adsorbed, resulting in a peak current. As the current decays rapidly at first it can be seen that either all ions within the electrodes are adsorbed into the EDL or the EDL is becoming more and more saturated. After a half hour of charging the applied electrostatic potential is set to zero and an inverted current response is observed. The ionic charge that has built up in the electrode is allowed to move out of the electrode and these adsorbed ions are consequently released back into the solution.

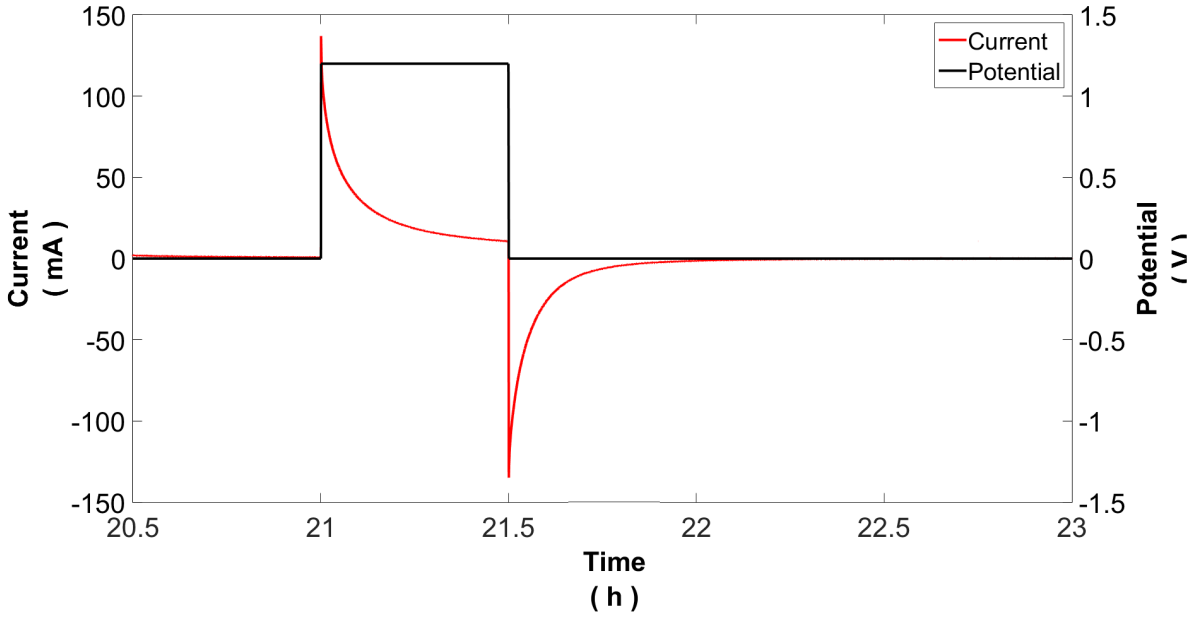

Figure 4.10: Applied potential and measured current signal during salt adsorption measurements.

In Figure 4.11a and Figure 4.11b the dynamic steady-state (DSS) that is attained after prolonged cycling. The activated carbon electrodes need time to fully develop their electrode-solution interface. For all electrodes the behaviour becomes stable after 15 hours of cycling, every cycle is close to the same. This DSS is necessary to correctly examine the manufactured electrodes. If the CF811 electrode is more closely examined in Figure 4.11b it can be seen that there are some differences between cycles, more precisely, the same behaviour is reoccurring every other cycle instead of every cycle. Here, it is hypothesized that there is some charge left locked in the CDI cell, from which cycling started. Polarizing the electrode around this shifted shorting potential could have resulted in such behaviour.

The electrode resistance was roughly measured after the electrode was installed in the fb-CDI cell using a multimeter, see Table 4.4. For the GF electrodes the resistance resulted in 92.5 Ω, 87.5 Ω and 70.23 Ω. The resistance measured here is not a very precise measurement and should only be considered as a rough indication for the resistance. It can be seen that the increased amount of conductive carbon significantly decreased the resistance of the electrode. However, the difference between the GF811 and the GF712 electrode cannot be differentiated easily. Looking at the CF electrodes, which show superior electrical conductivity, a significant difference can be observed between the CF electrodes themselves. This difference is the effect of wetting the electrode with an ionized solution. The CF811 and CF712 are measured after the desalination measurement as opposed to the others who were measured before wetting the electrodes. The wetted electrodes can accommodate current more easily as they can form the EDL in the electrodes.

Figure 4.12a shows the desalination performance of the manufactured glass fiber paper electrodes and

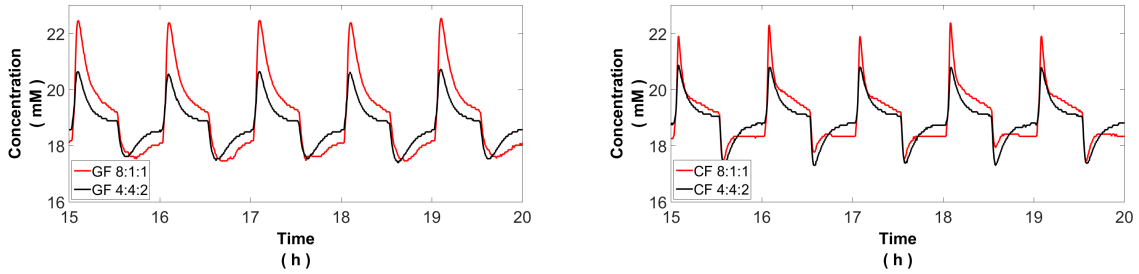

(a) (b)

Figure 4.11: Five adsorption/desorption cycles after 15 hours of operation, showcasing the level of dynamic steady-state reached for the GF811 and GF442 electrode (a) and the CF811 and CF442 electrode (b).

Figure 4.12b shows the performance of the carbon fiber electrodes. Each curve shows typical adsorption/desorption behaviour. Before this behaviour of interest is obtained the electrodes are cycled for 20 hours in order to obtain dynamic steady state. At 21 hours the cell is charged with 1.2 V and a sharp decrease in concentration is observed, analogous to the sharp increase in measured current. The charged ions are drawn to the oppositely polarized electrodes and stored in the pore structure. The deionized solution passes through the fb-CDI cell and once it exits the cell its conductivity is measured. It can be observed that after the initial decrease the effluent concentration slowly increases back to its initial value, due to the increasing saturation of the electrodes. At the end of the adsorption step it can be seen that the GF442 and the CF442 electrodes return closely to their initial concentration, meaning that the electrodes are very close to becoming fully saturated. The other electrodes are further removed from being fully saturated as compared to the 442 coated electrodes, and could have adsorbed more salt in case a longer cycle time was used. After a half hour of charging the electrodes are regenerated and a sharp increase in concentration is observed. All adsorbed ions are released from the electrodes and a concentrated brine is formed. As the time passes the concentration returns to its initial value and the electrodes are fully regenerated.

If a closer look is taken at the start of the charging step it can be seen that the CF electrodes all manage to reduce the concentration rapidly. The steep reduction in the solution concentration can be attributed to the higher conductivity of the CF electrodes. The carbon fibers in the electrode function as the electron pathway within the electrode, and therefore the conductivity of the CF electrodes is very similar. The GF electrodes have lower electrical conductivity as there is no designated electron pathway. In contrast, the electrons in the GF electrodes need to travel through the entirety of the coating. The lower electrical conductivity of the GF electrodes ensures a longer resistive-capacitive timescale, that allows slower micropore charging. Differences in the coating electrical resistances can be better differentiated in the GF electrodes.

The GF811 and GF442 electrodes seem to have the same behaviour initially and only the GF712 electrode is observed to respond differently straight from the beginning of the charging phase. It is very clear that the GF712 electrode has the most resistance to charging, this resistance can be explained by the low electrical conductivity of the coating and possibly higher ionic resistance as more of the electrode surface is blocked. The similarity between the GF811 and GF442 electrode ends as soon as the CF442 electrode becomes saturated more quickly. The high amount of carbon black in this electrode ensures a high electrical conductivity at the cost of electrosorption capacity. The steep concentration drop of the GF811 electrode can be explained by a lower electrical conductivity combined with an increased salt adsorption capacity.

After the initial decrease in conductivity the GF electrodes gradually grow their EDL until discharge. The CF electrodes show a steep associated concentration reduction followed by a more strong correction of the concentration, meaning the concentration increases back up rather swiftly for a part of the concentration drop. The steep reduction in concentration can be attributed to the low electrical resistance, thus short resistive-capacitive timescale, of the CF electrodes. The initial drive for the ions to be adsorbed is larger for the CF electrodes as compared to the GF electrodes.

After the applied potential is set to zero a sharp increase in concentration is observed. For the glass fiber electrodes, the sharpest increase can be observed for the GF811 electrode, followed by the GF712 and GF442 electrode respectively. The steepest concentration increase is expected as the GF811 electrode is assumed to have the largest ion capacity and so during the charging phase manages to adsorb/desorb most ions compared to the other two electrodes. The electrodes with more limited capacity lose the driving potential for electrosorption more rapidly due to saturation. For the carbon fiber electrodes surprisingly, the CF811 and

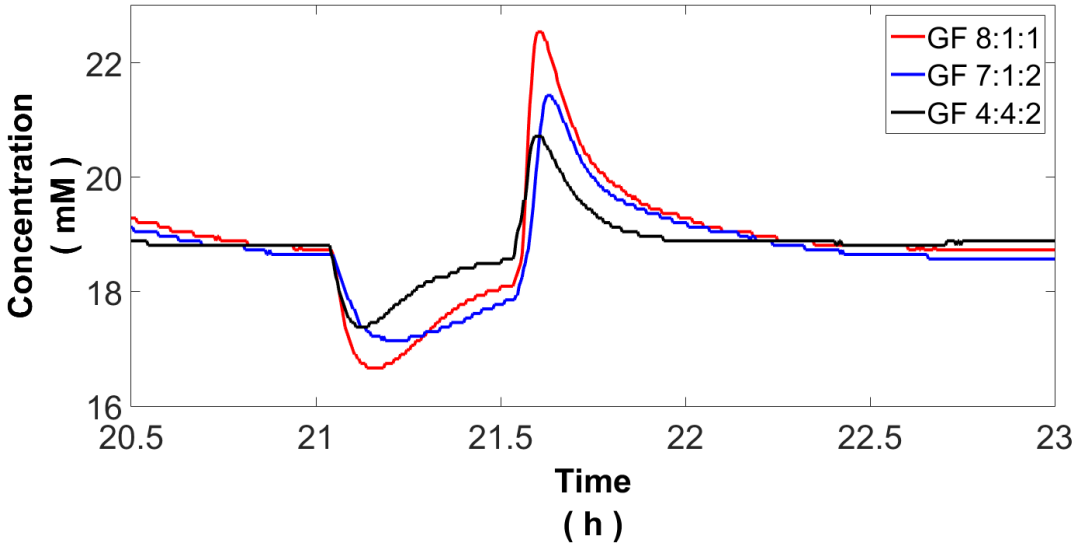

(a)

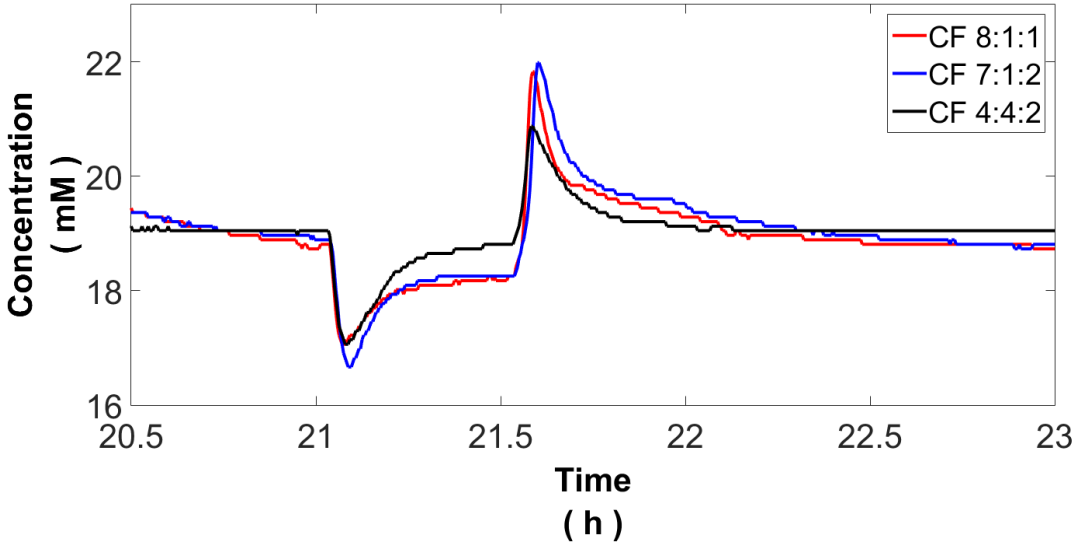

(b)

Figure 4.12: Salt adsorption measurement data for the electrodes: GF811, GF712 and GF442 (a). The salt adsorption measurement is executed at 5 ml/min flowrate and charged with 1.2 V. The measurement data for the electrodes: CF811, CF712 and CF442 are shown in b.

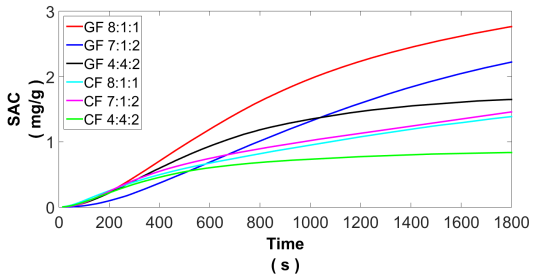

(a) SAC reached as a function of time for all manufactured electrodes, using 5 ml/min 19 mM NaCl feed and a charge potential of 1.2 V.

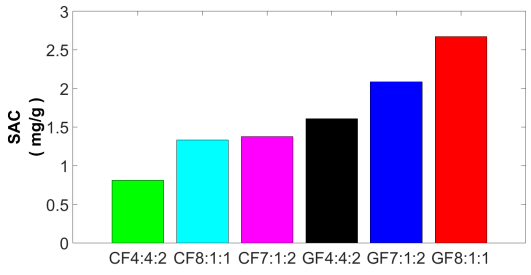

(b) SAC reached at the end of the 30 minute cycle, using 5 ml/min 19 mM NaCl feed and a charge potential of 1.2 V.

CF712 electrodes display very similar behaviour. More distinct results were to be expected, as the difference between the CF811 and CF712 electrodes should be similar to the difference between the GF811 and GF712 electrodes. Yet, a possible explanation is that the CF712 electrode is a little heavier than the CF811 electrode. The latter may point at more coating mass available to take part in the CDI process. Other explanations could be a difference in through-put or the fact that the CF811 electrode became compromised along its usage. Cutting the holes into the CF electrode had put stress on the edges of the electrode ensuring exfoliation and lose fibers. It is well possible this led to reduced desalination effect. In the appendix the effect of variability in through-put is shown. It is possible that, despite our best efforts here, the flow speed during the CF811 measurement the flow rate was somewhat larger, or the flow rate during the CF712 experiment was somewhat smaller.

The SAC values are determined by calculating the mean concentrations during the charge and discharge phases, utilizing a calculated reservoir concentration which equals the average measured concentration during the whole experiment. Knowing the difference in concentration of the reservoir (feed) and the effluent together with the through-put of the system the SAC of the electrodes can be determined. The resulting SAC values can be seen in Table 4.4. The charge efficiency is calculated using Equation 2.33, all determined charge efficiencies are conform literature, with charge efficiency reports between 35.5% and 43.1% [36].

Table 4.4: Results of the six electrodes manufactured of SAC, corrected SAC results using only projected electrode area masses, charge efficiency, Δc_{res}, the temperature during the measurement, preliminary measured electrode resistance and electrode thickness. SAC and λ are determined from a 30 minute cycle. Δc_{res} within Table 4.4 is a measure for how the calculated reservoir concentration deviates from the measured reservoir concentration. For all electrodes this deviation is around 1%, this can be a consequence of Faradaic reaction products or due to measurement error.

Electrode	**SAC (mg/g)**	**Area$_p$ SAC (mg/g)**	λ **(%)**	Δc_{res} **(mM)**	**T** ($^\circ C$)	**R** (Ω)	**h (mm)**	**m (g)**
GF811	2.80	4.40	41	0.18	20	92.5	0.61	4.27
GF712	2.24	3.52	45	0.13	20	87.5	0.55	4.34
GF442	1.66	2.61	38	- 0.10	19.2	70.23	0.45	3.53
CF811	1.43	2.25	39	0.20	19.2	6.6	0.53	5.54
CF712	1.47	2.31	47	0.36	18.9	7.43	0.54	5.86
CF442	0.84	1.32	40	- 0.05	20	35.8	0.56	6.25

The determined SAC values that are shown in Table 4.4 for both the glass fiber and carbon fiber electrodes can be correlated to their capacitances (and vice versa). More precisely, capacitance describes the electrical charge that can be stored in the solid electrode matrix, SAC describes the ion capacity that the electrode can adsorb. The SAC and capacitance each represent half of the EDL, and the two are related by the charge efficiency of the electrodes. Therefore, much of the same arguments in the discussion of the capacitance data applies here as well, such as the size of the charge that can be stored is heavily dependent on the amount of ACP within the electrode and carbon fiber electrodes show to have lower electrical resistance.

The largest SAC data is found for the GF electrodes, which is partly explained by the lower mass of the support structure. Upon taking a closer look at the values in Table 4.4, the order of high to low SAC for the GF electrodes is as expected. The larger the surface area of the electrode, the larger the SAC. The same rank order is found for the SAC data and capacitance data.

Surprisingly, the difference in SAC for CF811 and CF712 electrodes is not as expected. However, as we discussed earlier, this result may be due to parts of the electrode being compromised and the possibility of unequal flow rate. It can also be speculated that the CF811 coating, even though it is richer in AC, could have had less coating material, resulting in lower SAC and capacitance when these values are calculated w.r.t. the overall electrode mass including the glass fiber.

One can proceed by comparing the obtained SAC values to those found in literature. Specifically, here the results are compared to results of Kim & Yoon and Hou *et al.* [26, 35]. Kim & Yoon published a SAC of 6.2 mg/g, using an activated carbon power electrode with a surface area of 1095 m^2/g. The electrode was a circular disk of diameter 18 mm and thickness 300 μm. The coating composition existed of 86% ACP 7% CB and 7% PTFE. The desalination measurement was performed at 1.2 V, 10 mM NaCl, in single-pass applying 10 minutes charging. Kim & Yoon reported a capacitance of 63 F/g. In other work, Hou *et al.* published a SAC of 2.6 mg/g, using 90% ACP and 10% PVDF to form an activated carbon sheet electrode of 80 mm x 80 mm and 0.38 mm thickness. The BET surface area of the carbon used was 1124 m^2/g and the desalination measurement was completed at 2 mM NaCl with the feed being recycled. At the maximum SAC reached the

solution was for 96.7% desalinated. Hou *et al.* reported 55.7 F/g for their electrode.

As the manufactured electrodes are compared to the Kim & Yoon and Hou *et al.* electrodes, it can be seen that Hou *et al.* reports a value very similar to the SAC determined for the GF811 electrode, 2.6 mg/g vs. 2.8 mg/g. However, the desalination measurement of Hou is operated recycling all the feed and desalinating the entire solution, starting with a concentration of only 2 mM NaCl. The electrode of Hou *et al.* could have adsorbed more salt at a concentration of 20 mM NaCl. In regards to the Kim & Yoon electrode it can be seen that they report a SAC much larger than 2.8 mg/g. The high reported SAC of 6.2 mg/g can be explained by the somewhat larger surface area, different electrode composition and better electrode electrical conductivity. However, the large difference can most importantly be explained by the cell design, the cell used in this work ensures part of the electrode material does not partake in the electrosorption process. The active area adjusted SAC, which is close to 60% larger, of the GF811 electrode results in 4.40 mg/g and is more in line with the results of Kim & Yoon and Hou.

Figure 4.14 presents the relationship between the measured SAC and the predicted SAC out of the capacitance data acquired in the CV measurements. The predicted SAC values are determined according to Equation 2.32 [34]:

$$SAC_p = \frac{1000CUM_w}{4F}.$$

In the figure the SAC and capacitance, that are determined using only the projected area, are shown. As can be seen all red dots, which represent individual electrodes, are found to utilize a little more than 42% of the predicted SAC. The 42% is the charge efficiency that is determined from the measured current during the salt adsorption measurement. Surprisingly enough, the electrodes are not supposed to utilize more than 42% of the predicted SAC. The capacitance data is collected at 1.0 M NaCl and not 20 mM NaCl. The EDL is concentration dependent and so the measured capacitance at larger concentration is higher. Relating the predicted SAC using 1.0 M NaCl data to SAC at 20 mM data cannot only be related using the charge efficiency, and more margin is anticipated.

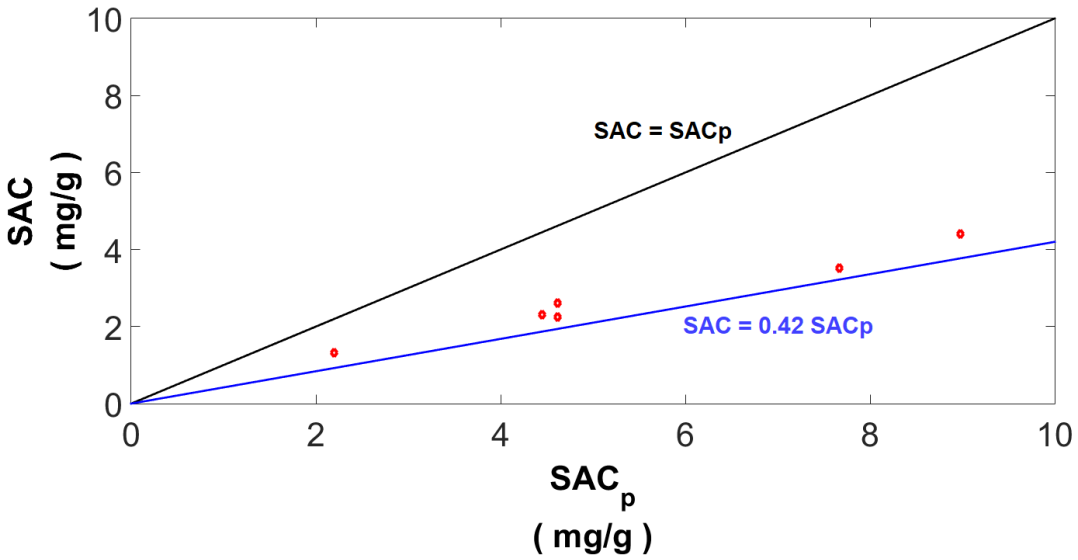

Figure 4.14: This graph depicts the relation between the measured SAC and the predicted SAC. All electrodes (red dots) are seemingly in line with the determined mean charge efficiency of 42%, however all overshoot. Here, the area adjusted SAC and the area adjusted capacitance data are utilized and plotted. The predicted SAC is determined from capacitance data acquired at 1.0 M NaCl.

4.5. Demonstrating MC-CDI Functionality

The electrodes build in this study are free-standing electrodes purposed for MC-CDI operation. The CDI process performance analysis and optimization of MC-CDI is however not part of this thesis. Anyhow, it is important to demonstrate that the electrodes are able to function in MC-CDI operation. To start, we analyze

the permeability of the middle electrode while these electrodes are disconnected from any power supply. To this extent, Figure 4.15a and Figure 4.15b show the results of circulating two different reservoirs of 500 ml with different concentration through the two channels in the MC-CDI cell. The flow rate maintained during the measurement is 5 ml/min. The two channels, and their respective reservoirs, are separated by one electrode with an area of 90 mm x 75 mm. The conductivity is measured at the outlet of each channel. In both figures it can be seen that the larger concentration decays exponentially, oppositely to the smaller concentration reservoir that increases in concentration. This result is in line with the situation of two reservoirs separated by a membrane that allows permeation of the solute. Both electrodes behave similarly and it can be concluded that the electrodes allow salt permeation in non-forcing conditions.

To quantify a measure of permeation a half-live time ($t_{1/2}$) can be determined for both electrodes. The half-life time is the time interval for the difference in concentration of the reservoirs to be halved. For the GF811 electrode the half-live time is 290 minutes. For the CF811 electrode $t_{1/2}$ is 310 minutes. The two half-life times do not differ much as could be interpreted from the graphs.

Figure 4.16a and Figure 4.16b show the results of actual MC-CDI operation. Here, both reservoirs contain the same concentration and are pumped through the cell under forcing conditions. A 4-stage MC-CDI protocol is applied utilizing potential fields and electrosorption to desalinate one channel into the other, which can be seen in Table 4.5. upon close analysis of the results it was found that the MC-CDI protocol was improperly implemented, here, some MC-CDI functionally still remained and thus the results supplied interesting insights still.

The observed concentrations look similar, albeit two major differences are observed. For the case of the GF811 electrode is used the concentration difference reaches a significant size much faster. It is possible that this difference originates from different reservoir concentrations, and therefore the concentration difference between the channel establishes a much larger difference faster. Another observation is that channel 2 in Figure 4.16b only shows one peak instead of the two peaks that are observed in Figure 4.16a for channel 1. The lost peak in Figure 4.16b coincides with the applied electrostatic potential reversal of the middle electrode. This is the electrode that separates the two channels. This peak is missing in the effluent of one channel, however, it is still visible in the effluent of the other channel. It may be speculated from this result that as the electrostatic potential reverses the CF electrode preferentially releases ions in one direction, whereas the GF electrode releases its ions to a greater extent in both directions. This can be explained by the dense fiber structure of the CF electrodes, which could hinder the permeability for ions. The CF electrode electrosorps ions on one side of the electrode and after the electrostatic potential reversal the are not attracted enough by the electrode on the far-side, and the ions are desorbed into the channel the ions originated from.

The electrodes build in this work should be intensively be researched in MC-CDI operation. From those results the electrode receipt and manufacturing method for MC-CDI electrodes can be optimized.

Table 4.5: 4-Stage MC-CDI protocol intended for use during MC-CDI operation. + and - indicate the electricity pole the electrode is connected to at each stage, the 0 indicates the electrode is disconnected.

Stage	**1**	**2**	**3**	**4**
Electrode A	+	0	-	0
Electrode B	-	+	+	-
Electrode C	0	-	0	+

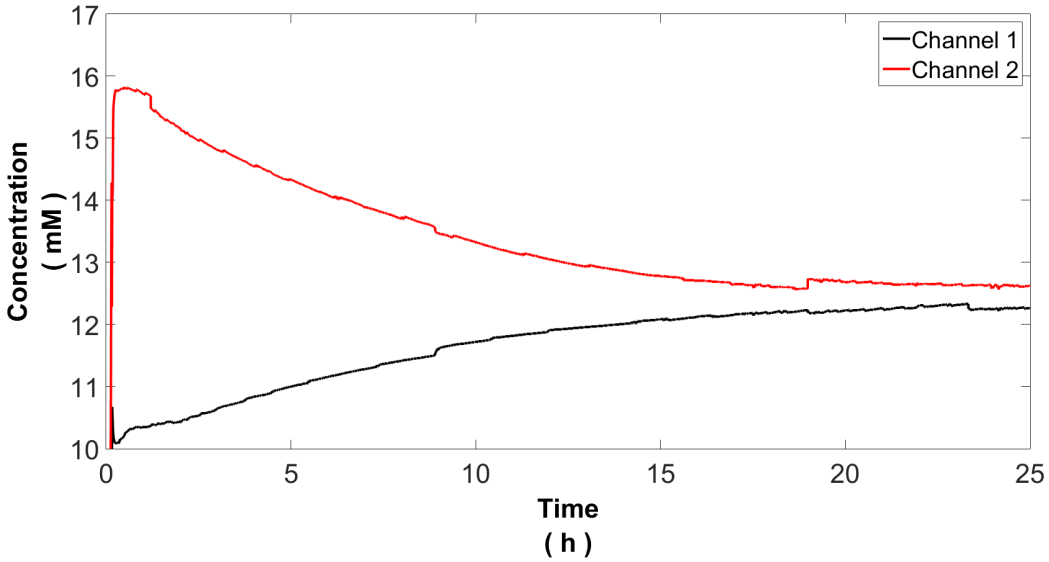

(a)

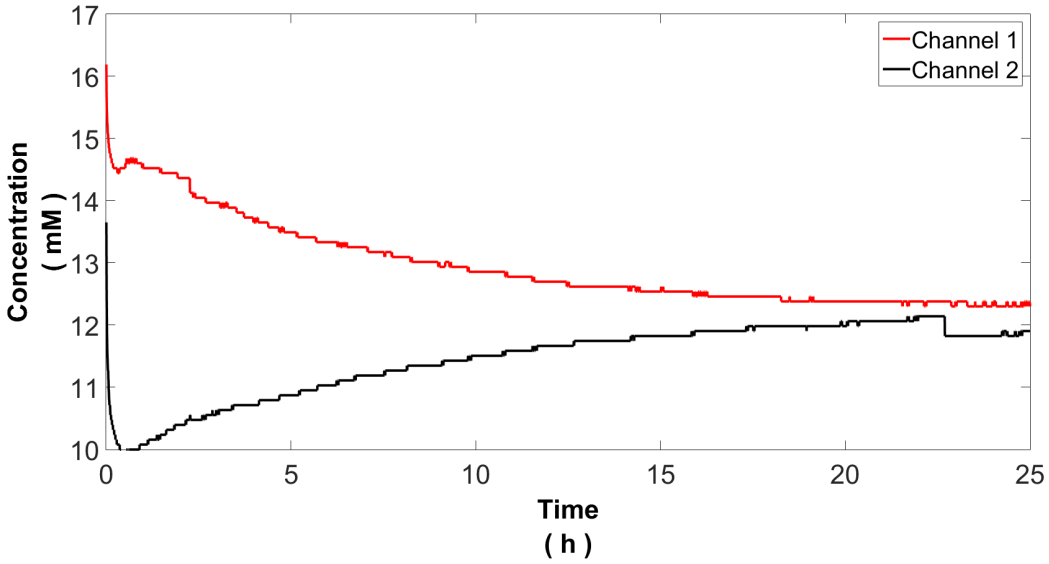

(b)

Figure 4.15: Conductivity data from each outlet of the MC-CDI cell installed with the GF811 electrode (a) and the CF811 electrode (b). Two different reservoirs are pumped through their respective channel in the MC-CDI cell at 5 ml/min, no potential field is applied.

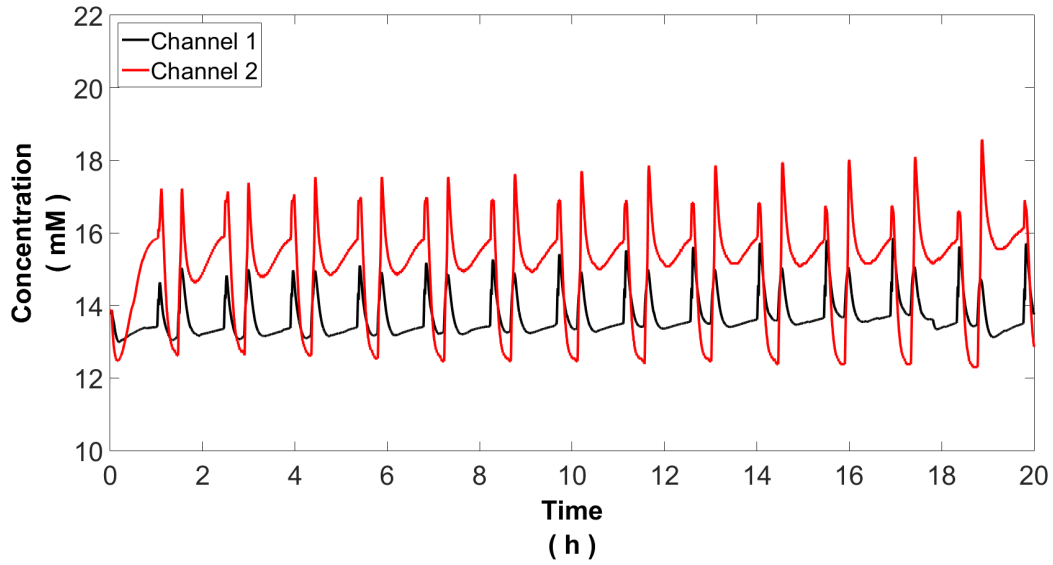

(a)

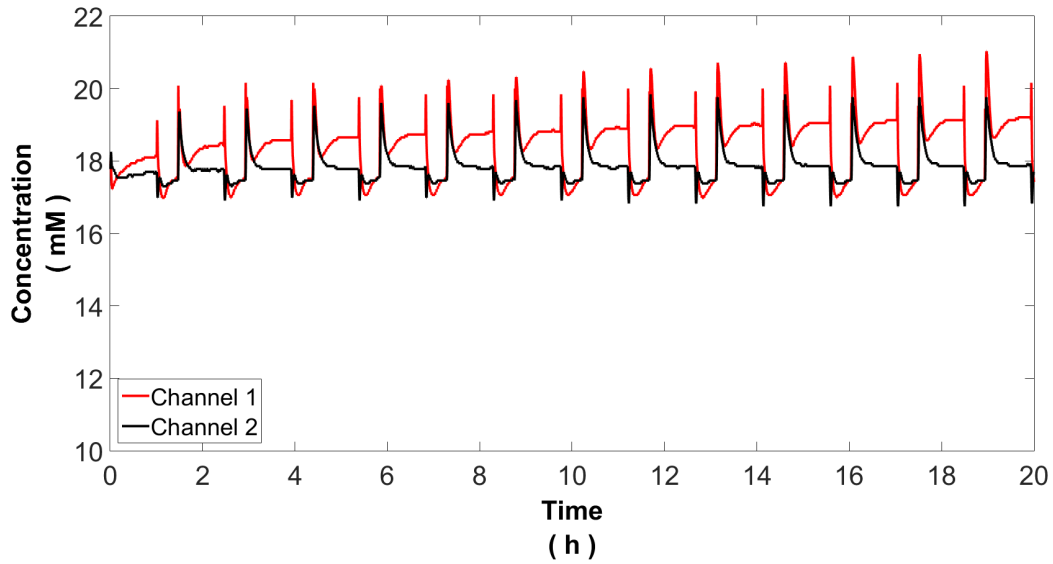

(b)

Figure 4.16: Conductivity data from each outlet of the MC-CDI cell installed with the GF811 electrode (a) and the CF811 electrode (b). Two different reservoirs are pumped through their respective channel in the MC-CDI cell at 5 ml/min, a MC-CDI protocol is applied to desalinate one channel into the other.

4.6. Modelling Electrosorption

The goal of modelling electrosorption is to gain insight in the effects of varying electrode properties. The two-electrode fb-CDI model is used to be able to compare results to literature and the completed salt adsorption measurements. The model includes coupled external electrical networks, charge conservation, and species conservation in bimodal pore structure electrodes. The two-dimensional porous electrode model for CDI is implemented in COMSOL Multiphysics using transport of diluted species and equation-based modelling interfaces.

The model is fitted to the GF442 electrode as this electrode is one of the manufactured electrodes that contains the smallest SAC. As the capacity of the electrode is smallest the equilibrium at the end of the adsorption phase is approached more closely compared to the other electrodes. The model can best be fitted to experimental data that reaches up to equilibrium to estimate the free parameters. The effluent concentration data from the salt adsorption measurement is used to fit the model to the experimental data: the nonelectrostatic adsorption potential, micropore capacitance and micropore porosity are determined by minimizing the error between experiments and model results. Figure 4.17 shows the experimental effluent concentration measured, along with the fitted model results. The model parameter settings can be seen in Table 4.6. For all parameter studies below, these are the default values.

The free parameters in this study are estimated to be: $\mu_{att} = 1.0$, $C_m = 73.15\ MF/m^3$, and $p_m = 0.2486$. The values reported by Hemmatifar *et al.* are $\mu_{att} = 1.5$, $C_m = 150\ MF/m^3$, and $p_m = 0.3$. Hemmatifar used a pair of activated carbon electrodes, these are assumed to be a more classical 8:1:1 composite electrode. The parameters estimated in this study can be deemed coherent as the content of activated carbon in the GF442 electrode is significantly lower and the replacing amount of Vulcan XC-72 is assumed to have lower nonelectrostatic adsorption, lower micropore capacitance and smaller micropore porosity.

Table 4.6: Parameter settings for the model fitted to the GF442 electrode.

Parameter	**Description**	**Value**	**unit**
μ_{att}	Nonelectrostatic adsorption parameter	1.0	
C_m	Micropore capacitance	73.15	MF/m^3
p_m	Micropore porosity	0.2486	
p_M	Macropore porosity	0.4514	
D	Diffusion coefficient in the gap	1.47e-9	m^2/s
D_e	Effective diffusion coefficient in macropores	7.35e-10	m^2/s
c_0	Influent salt concentration	18.81	mM
R_s	Electrical resistance	5.0	Ω
U	Mean flow velocity	1.11	cm/s
L_s	Gap thickness	1.0	mm
L	Electrode length	90	mm
L_e	Electrode thickness	0.5	mm
W	Electrode width	75	mm

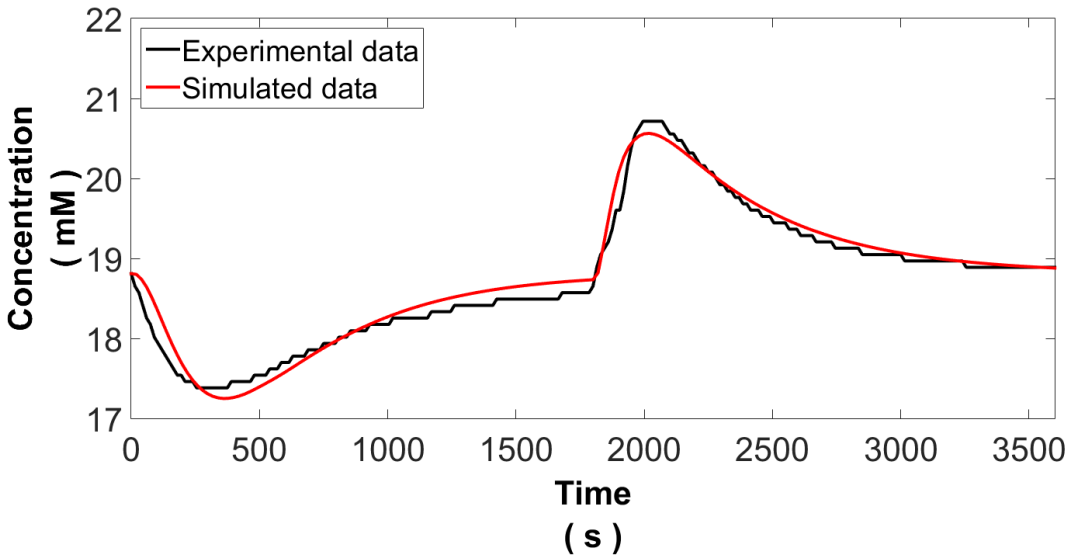

Figure 4.17: Experimental effluent concentration data from the GF422 salt adsorption measurement compared to the fitted model results. Model parameters can be seen in Table 4.6

Figure 4.18a and Figure 4.18b present the simulated concentration profile in the gap and the macropores of the top part of the symmetrical fb-CDI cell. The upper square represents the electrode domain, currently showing macropore concentration profiles plus contours, and the lower square is the gap domain. The inlet and outlet domains are not shown here. Note that the figure is not to scale and the scales for the x and y axis are not equal. The electrode is charged at 1.2 V at 5 ml/min flow rate. The electrode is charged for 1800 seconds and discharged for 1800 seconds at 0 V.

20 seconds after the electrostatic potential difference is applied, a near-gap depletion zone can be observed. As time goes on, the depletion zone grows in size propagating upwards. The initial rapid adsorption of ions is related to the resistive-capacitive time scale. After 200 seconds the charging of the micropores is characterized by slow, diffusion-limited transport of ions from the gap into the electrode. At the end of the charge phase it can be seen that the electrode is close to being saturated, and the electrolyte within the electrode returns to close to its initial concentration.

Figure 4.18b displays the discharging of the electrode at 0 V. Note the rapid increase in concentration in the near-gap region, which is due to desorbing of the ions. After 200 seconds of discharging the concentration in the macropores overshoots the colour range, reaching a concentration larger than 29 mM. The rapid desorption is then, analogous to the charging phase, followed by a slow diffusion-limited transport of ions out of the electrode.

Whilst Figure 4.18a shows the salinity in the macropores and flow channel, Figure 4.19a gives an insight into the actual salt absorbed inside the electrode. Note that for this reason the flow-channel region is left white. Looking at the charging process of the micropores, the micropores closest to the gap charge fastest, and as time goes on more and more micropores charge.

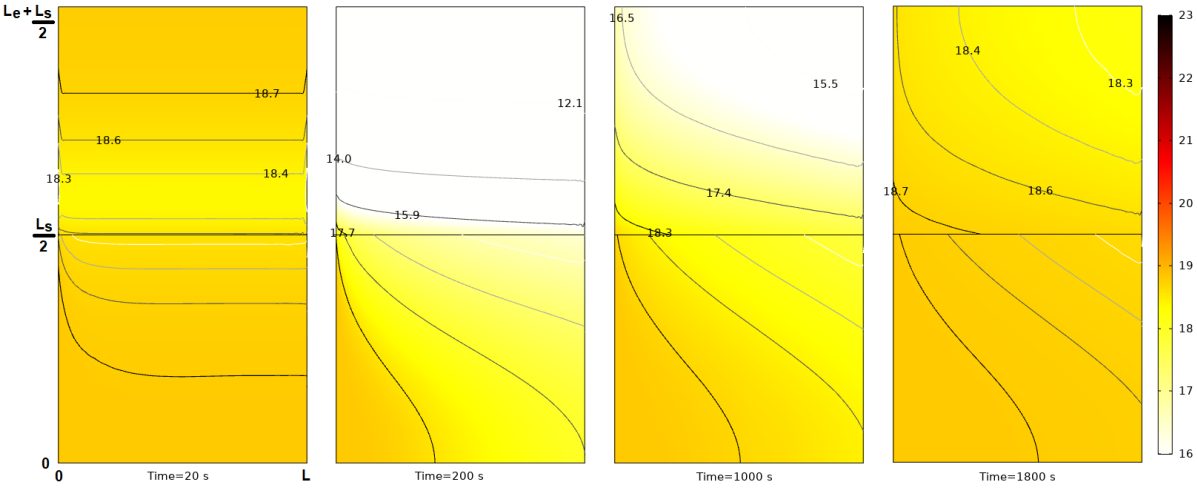

(a)

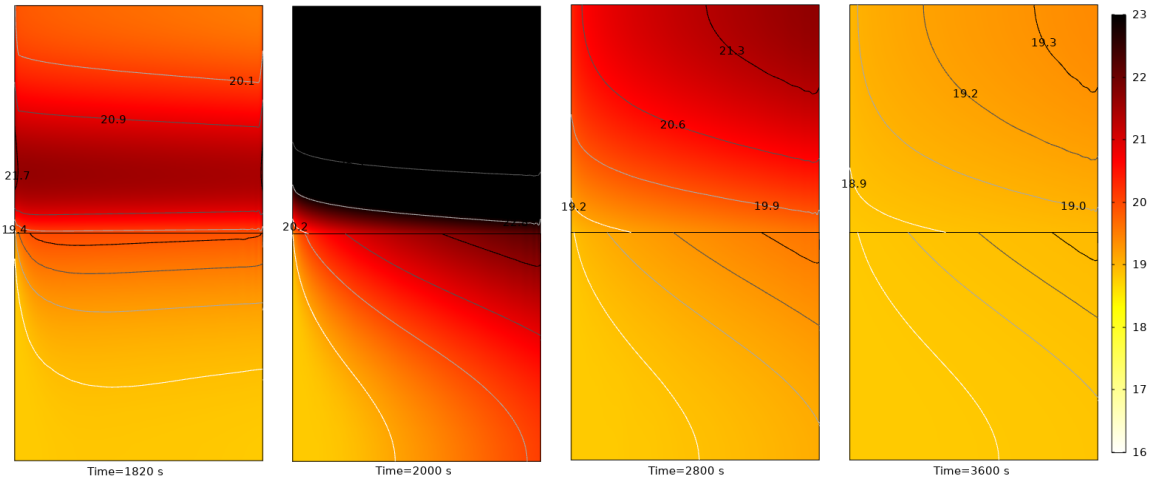

(b)

Figure 4.18: (a) Simulated ion concentration fields (mM) in the gap (lower square domain) and macropores (upper square domain) for the symmetric top half of the cell (not to scale) during charging and (b) discharging. The color coding represent the local ion concentration. During charging, a depletion region forms near the electrode-gap interface, which rapidly propagates upward. The rapid charging is followed by diffusion-limited uptake of new ions from the gap. At discharge the adsorbed ions are rapidly repelled from the micropores, starting in the near-gap region. Discharge then slows down due to diffusion-limited transport of ions out of the electrode.

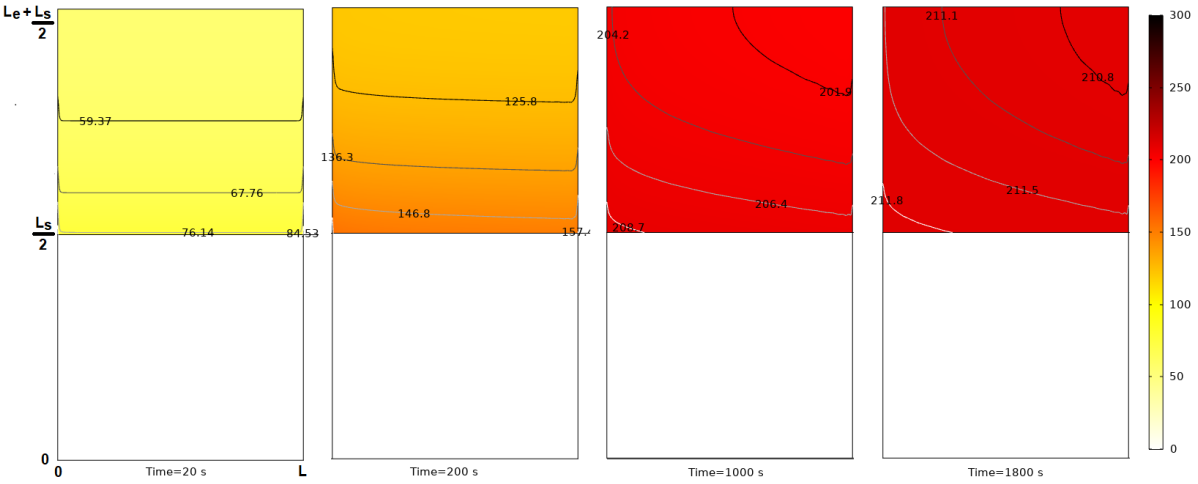

(a)

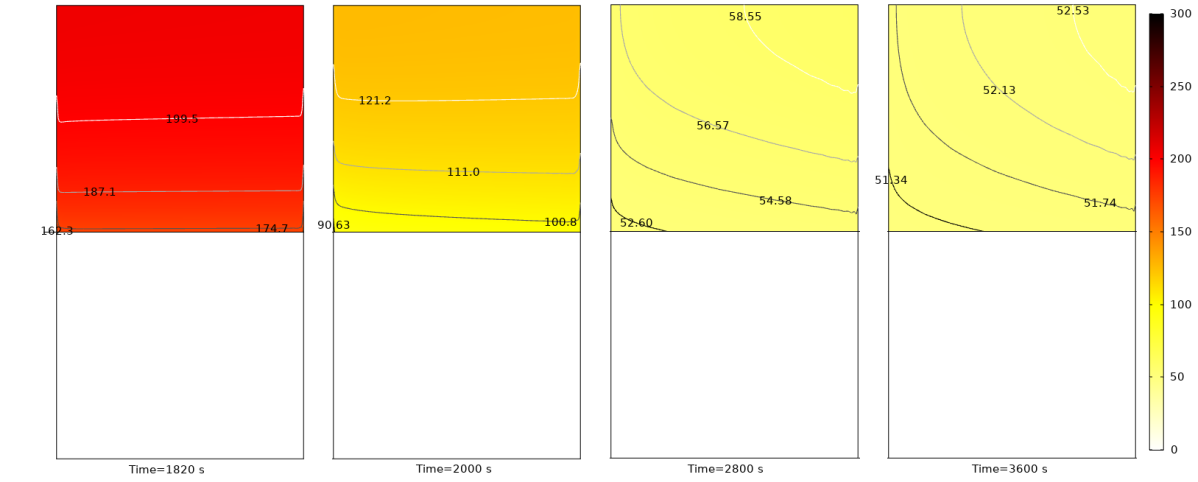

(b)

Figure 4.19: Simulated ion concentration profile (mM) in the micropores of the upper electrode (not to scale) for charging (a) with 18.81 mM inlet concentration and (b) discharging. The micropores in the near-gap region charge first, and as time goes on more and more micropores are charged.

As was mentioned earlier in this thesis, it is important for the electrodes to be characterized by a low electronic resistance, as this will enable faster charging of the electrodes. In Figure 4.20 the effect of varying resistances in simulated cells is shown. Note that all electrical resistances in the model are lumped together in the series resistance R_s. This includes the electrical resistance inside the solid electrode matrix. As shown before in the cyclic voltammetry measurements this resistance slows down charging. In the cyclic voltammetry measurements this was observed in the dampening effect of the resistance on the current response. Here, in the effluent of the fb-CDI cell, the same dampening effect can be observed. At higher resistance to charging, the ions are adsorbed more slowly, and the desalination effect is more limited.

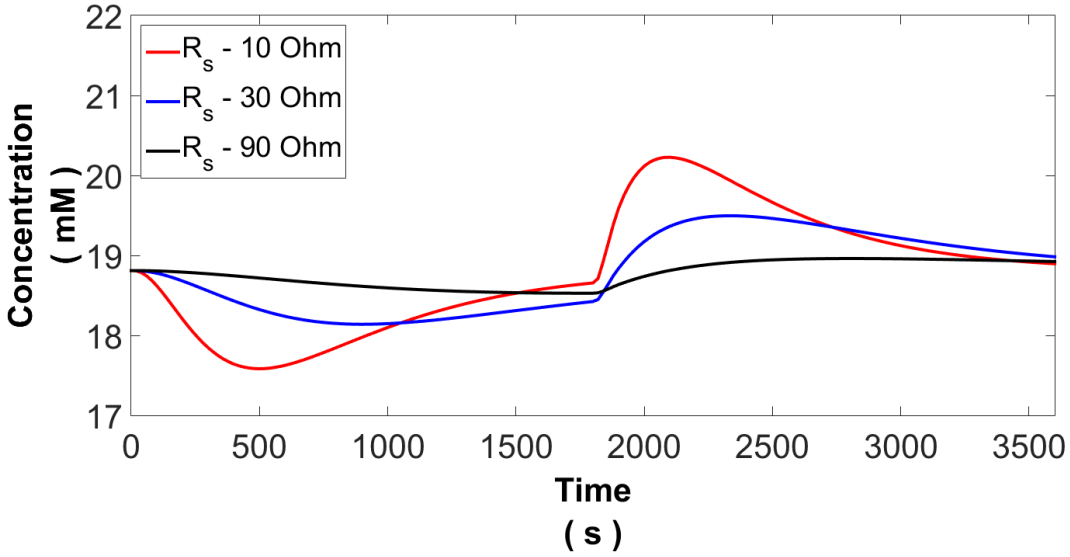

Figure 4.20: Parameter study with varied series resistance, displaying effluent concentration during one hour adsorption/desorption cycle. Model parameters can be viewed in Table 4.6.

Electrodes can differ in their volume available for ion adsorption. This can be due to difference in composition, as shown by the experiments, but also by employing a different ACPs. Figure 4.21 presents the effect of different electrode materials containing more or less volume that takes part in the electrosorption process. This can be studied by changing the micropore porosity within the model. As expected, it can be observed that upon increasing p_m the adsorption capacity increases, as can be observed from the increasing area between the inlet concentration and the plotted effluent concentration. A more interesting observation can be made by examining the desorption peaks. From $p_m = 0.2$ to $p_m = 0.3$ the desoprtion peak, i.e. the maximum concentration during the desorption process, initially increases with pm. However, this trend is reversed when pm reaches 0.4, which may be a residual effect of the lower concentration at the end of the absorbtion phase that precees the desorption. It can thus be observed that larger pm tends to slow down the absorption/desorption process. An additional effect that may play an important role here is that the surge in concentration is also restricted by the lowering of the available macropores. As the amount of micropores is largest, the amount of macropores is smallest, following from $p_m + p_M = 0.7$. As the amount of macropores becomes smaller, the concentration increase in the macropores right after desorption becomes largest. The increasing concentration in the electrode becomes a increasing resistance for discharging of the micropores.

As was mentioned earlier, the electrode thickness was assumed important for the electrosorption kinetics of the process. Figure 4.22 shows the effect of different electrode thickness within the fb-CDI cell. It can clearly be seen that the thicker electrodes contain more capacity. It can also be observed that the thinner electrodes not only saturates faster, in addition the charging of the electrode proceeds faster as well. The latter has again to do with the charging resistance of the electrodes. The lumped charging resistance is the same for all electrodes. In the model the resistance is independent of the thickness of the electrode. Comparing the electrodes with different thicknesses, initially as the electrostatic potential is applied, all electrode material is trying to involve its self in the electrosorption process. This results in a largest current for the electrode with the most electrode material, which is the electrode with the largest thickness. As the current increases, the voltage drop over the internal resistances increases as well. Therefore, due to the smaller currents, the micropores of the electrode with the least amount of electrode material are least impeded in charging themselves,

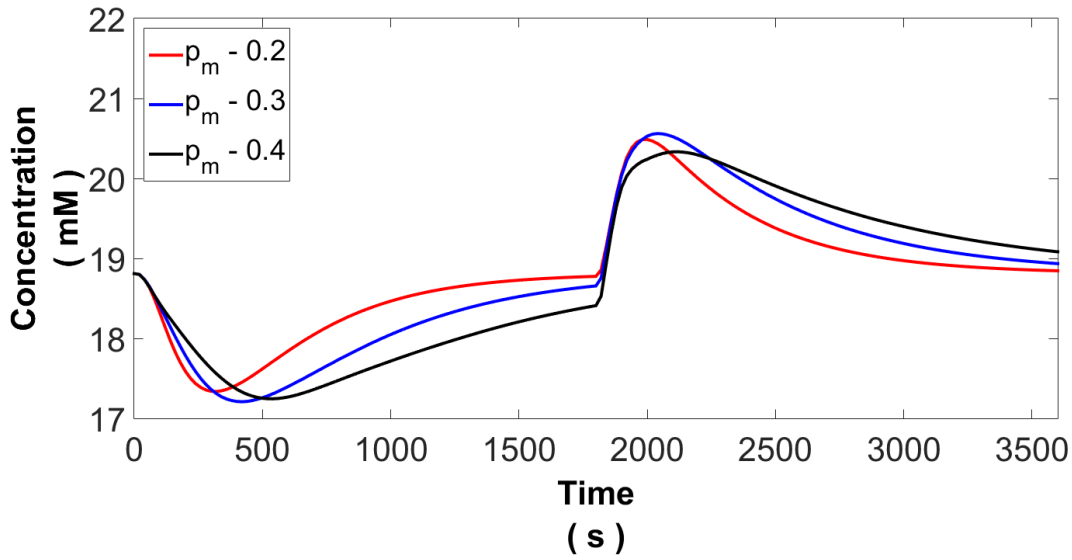

Figure 4.21: Parameter study with varied micropore porosity, displaying effluent concentration during one hour adsorption/desorption cycle. Model parameters can be viewed in Table 4.6.

resulting in a faster dropping concentration drop in the effluent of the cell. Figure 4.22 also shows that it is easier for the thinnest electrode to transport the adsorbed ions back into the gap, as its diffusion timescale is smallest.

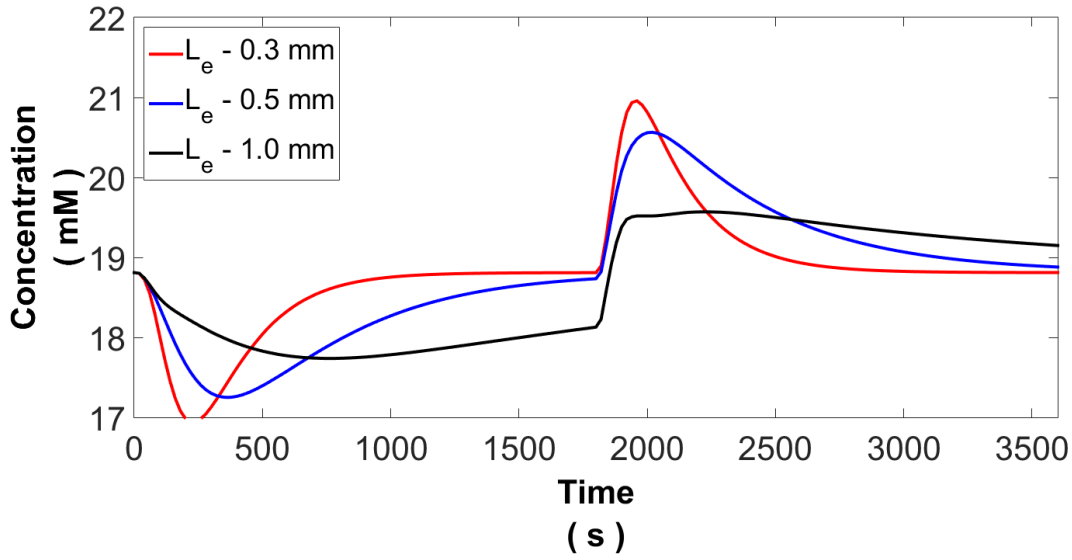

Figure 4.22: Parameter study with varied electrode thickness, displaying effluent concentration during one hour adsorption/desorption cycle. Model parameters can be viewed in Table 4.6.

It could prove insightful to try and recreate the salt adsorption measurement curves for the GF811 and GF712 out of the fitted GF442 model. The GF442 model was chosen as a reference because of its smallest adsorption capacity. Taking the fitted data as a starting point, the model can be adjusted and altered, accordingly to the observations made in the electrical conductivity and micropore porosity parameter studies. Note that these curves are not fitted to their respective experimental data, but are iterated to sensible values for p_m, p_M, C_m and R_s.

Figure 4.23a shows the experimental data of the effluent concentration measurements during the salt adsorption measurements of the GF electrodes. Out of the capacitance and SAC data it is know that the capacity of the GF811 electrodes is close to being twice that of the GF442 electrode. Therefore, the micropore porosity pm is doubled and the resulting change in the simulated concentration curves is analyzed. It was found that by doubling the micropore porosity the macropore volume had become too small to provide a fitting adsorbtion/desorption cycle. It turns out that a good fit can be obtained by not only changing p_m, but also an updated value for the micropore capacitance and total porosity is needed. The total porosity of the GF811 and GF712 electrode was increased to $p = 0.8$ instead of $p = 0.7$, and the micropore capacitance is increased to $1.35e8\ F/m^3$. The electrical resistance is only changed form 5.0 Ω to 6.0 Ω as the initial concentration drop, seen in the experimental data, is very similar for both electrodes. By applying these alterations to the fitted GF442 parameters, it is very well possible to recreate similar effluent concentration data for the GF811 electrode. From these findings it is confirmed that the GF811 electrode has increased salt adsorption capacity due to increased porosity, larger micropore volume and larger volumetric micropore capacitance.

To match the GF712 electrode salt adsorption measurement data out of the GF442 fitted model, the resistance needs to be increased significantly to 10 Ω, which is an increase that can be expected as the carbon black content is significantly lower, whilst the binder content is not decreased, as is the case for GF811. The micropore porosity of the GF712 is assumed to be somewhat smaller than that of the GF811 electrode, set to $p_m = 0.30$. Table 4.7 shows the alterations made to the GF442 fitted model to recreate the GF811 and GF712 electrode salt adsorption measurement data. By trying to match the experimental GF712 curve, it is found again that the micropore capacitance needs to be increased to ensure the GF712 curve dips below the GF811 curve at the end of the adsorption phase. In retrorespect, this may point at the fact that the initial fitted capacitance of the GF442 model may have been ambiguous, and another parameter set, including a different capacitance, could have given a satisfying result as well. In this study the three free parameters are all estimated in one optimization study. To delivered a better fit the parameters should be estimated in a way that resulting estimated parameters are most confined. To this extent, Hemmatifar *et al.* proposed a method involving equilibrium data at the end of the adsorption phase [24]. He investigated the equilibrium solution at infinitely long time after applying the electrostatic potential. Here, the solution is solely governed by the EDL model used, voltage applied, and inlet concentration. From this solution the three free parameters can be reduced to just two independent parameter groups, $P_m C_m$ and $p_m \exp(\mu_{att})$. If experimental equilibrium conditions are utilized, together with the dynamic salt adsorption measurement data, the free parameters could be estimated more deterministic. Constituting the best fit is not the scope of this work, as understanding the effect of varying parameters is. Nonetheless, as the model is expanded to MC-CDI simulations in the future the best fit becomes more important, as in MC-CDI the spatial distribution of the salt becomes more critical.

Table 4.7: Original fit parameters for the GF442 experimental data, and the updated parameters that will produce good fits for the other electrodes.

Parameter	**GF442**	**GF712**	**GF811**
C_m	7.315e7	1.5e8	1.35e8
p_m	0.2486	0.30	0.32
p_M	0.4514	0.50	0.48
R_s	5.0	10	6.0

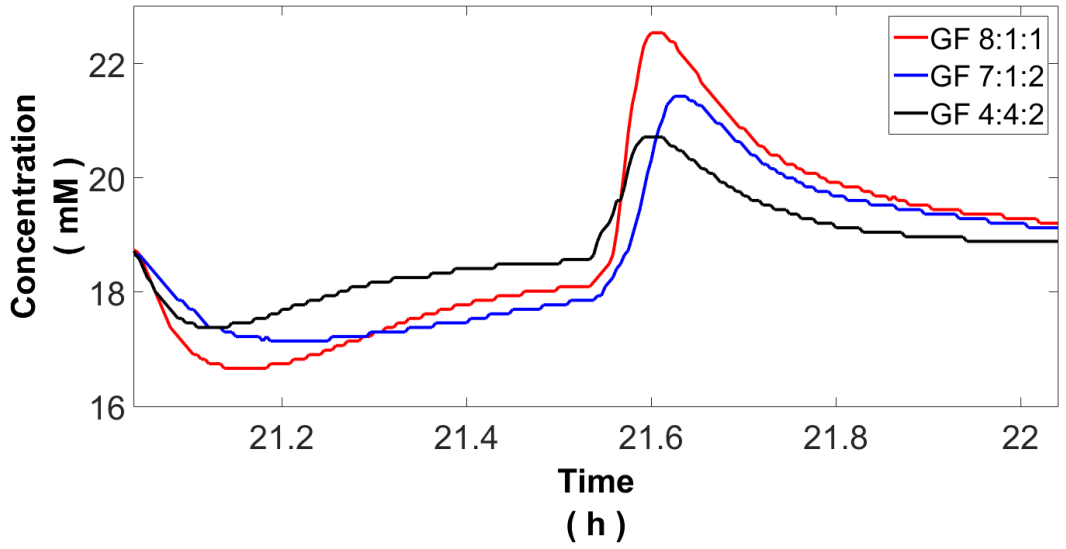

(a)

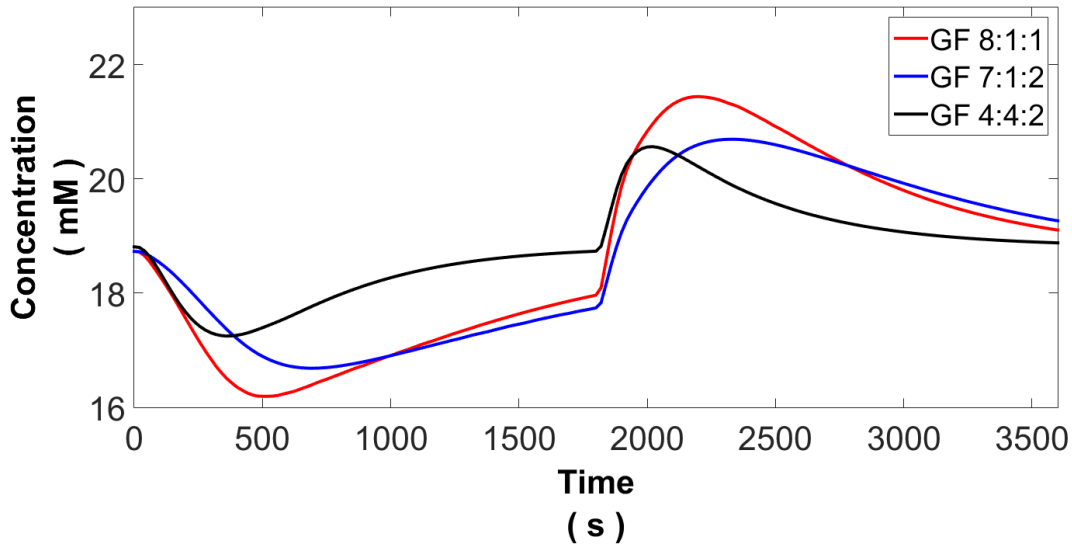

(b)

Figure 4.23: (a) Salt adsorption measurement data for the electrodes: GF811, GF712 and GF442. (b) Simulated CDI model data, model parameters used besides the default parameters can be viewed in Table 4.7.

5

Conclusions & Recommendations

In light of growing water scarcity problems, solutions to expand the drinking water supply are sought after. Desalination presents itself as a sensible option, as it opens up access to the vast salt water resources on Earth. Capacitive deionization (CDI) is a novel desalination technology that is based on separating salt ions from aqueous solutions in an electrical double layer, and is currently widely researched for its advantageous desalination of brackish water.

In this project free-standing activated carbon electrodes are manufactured for application in multi-channel CDI (MC-CDI). In MC-CDI three or more electrodes are utilized in order to incorporate two or more channels in the CDI cell. During MC-CDI operation the electrodes are polarized, following a thought-through scheme, in order to desalinate one channel into another channel. For MC-CDI to function properly the electrodes used need to be permeable to transport the ions through the electrode, this is not necessary for conventional CDI, thus current available electrodes are not tailored to, or not usable at all, in MC-CDI.

During this project six different types of electrodes are successfully manufactured, purposed for MC-CDI. Glass fiber paper and carbon fiber are dip coated, resulting in smooth permeable electrodes. The coating is prepared using activated carbon powder (ACP), carbon black and PVDF binder. ACP provides large surface area for ion adsorption, the ACP used is a typical microporous activated carbon with a specific surface area of 930 m^2/g. Carbon black is added to increase the electrical conductivity of the coating and the binder provides mechanical stability to the coating film. The six different electrodes consist of three different coating compositions coated onto the glass fiber paper and carbon fiber. The three coatings can be differentiated in a high ACP coating, a high binder coating and a high carbon black coating. It is hypothesized, that a coating high in carbon black can function more efficiently in MC-CDI, as the electrosorption process takes place on the outer surface area in larger amounts. Dip coating the electrodes allows for swift application of the coating and the applied coating mass can easily be controlled by applying multiple layers.

The electrodes are evaluated using cyclic voltammetry and salt adsorption measurements. The electrodes with the largest amount of ACP display the largest capacitance and salt adsorption capacity (SAC). The best gravimetric performing electrode is the glass fiber paper electrode with high ACP coating, which can be characterized by a capacitance of 31.44 F/g and a SAC of 2.80 mg/g. To compare the experimentally determined capacitance and SAC with literature, the fact that part of the electrodes is covered by the rubber gasket is taken into account, this part is excluded to contribute to the electrosorption process. The active area adjusted capacitance and SAC for the glass fiber paper electrode with high ACP coating result in 49.37 F/g and 4.40 mg/g, and is in line with literature. Altering the coating composition by replacing half of the ACP with carbon black, as in the high carbon black electrode, it can be seen that the electrical conductivity is improved at the cost of reducing the capacitance and SAC by around half. It is shown that increasing the binder mass in the coating results in mechanically more stable electrodes, at the cost of blocking surface area from ion adsorption. The carbon fiber electrodes have superior electrical conductivity compared to the glass fiber electrodes, however, the conductivity of the glass fiber electrodes does not under-perform dramatically and a non-conductive support structure can very well be used in CDI electrodes. The carbon fiber electrodes display more limited MC-CDI functionality, as the carbon fiber structure results in a more dense separation between the channels, potentially resulting in less efficient MC-CDI operation. It is also shown that Faradaic reactions take place during CDI operation in the form of carbon oxidation.

Alongside the manufacturing and evaluation of the electrodes, two-dimensional electrosorption simulations are performed to explore the effect of electrode resistance, micropore porosity and electrode thickness. This model included coupled external electrical networks, charge conservation, and species conservation in bimodal pore structure electrodes. The model includes three free parameters: non-electrostatic adsorption of ions into micropores, volumetric adsorption capacitance of micropores, and porosity of micropores. The model is applied to conventional flow-by CDI in order to best compare results to literature and the salt adsorption measurements. The model is fitted to dynamic effluent salt concentration data. Electrosorption simulations showed that the process takes place in two distinct phases: fast initial micropore charging, followed by slow diffusion-limited uptake of salt from the gap. Spatiotemporal concentration profiles are presented of the micropores, macropores and gap. Increasing the electrical resistance results in an impeding effect on electrosorption. Increasing the micropore porosity results in larger SAC. Thicker electrodes can adsorb more salt, however, the adsorption kinetics are more limited by the increase of the diffusion time scale. From these results, thin highly electrical conductive electrodes with large SAC can be derived to be preferable in MC-CDI operation.

Based on the findings of this thesis, it may be expected that further increase in performance can be reached by developing electrode support materials that combine the structural properties of glass fiber paper with the conductive properties of carbon fibers. These electrodes should be extensively investigated in multi-channel CDI operation in order to determine the performance in MC-CDI operation.

The electrical response of the CDI cell can be understood by impedance spectroscopy (EIS) and determining the equivalent electrical circuit, as is described in Appendix A. Future studies into this topic could help to accurately determine electrical resistances and provide another handle to optimize the electrode recipe.

To better fit the free parameters to the experimental data, experimental equilibrium data should be obtained at very long charging times. With this data the fitting procedure as by Hemmatifar *et al.* can be utilized [24]. By calibrating the model using the dynamic effluent concentration data, in combination with equilibrium adsorption data, the free parameters can be estimated more deterministic.

In conclusion the findings in this work supplied a method of manufacturing activated carbon electrodes and substantiated a clear insight into the ideal MC-CDI electrode. MC-CDI can be an elegant addition to the family of existing CDI architectures and potentially help alleviate water shortages around the world.

A

Resistances in Capacitive Deionization

A.0.1. Equivalent Electrical Circuit Modelling

The different physical processes in the CDI cell are hard to perceive and distinguish from each other. Equivalent electrical circuit modelling can be used to provide information by simplifying the system into elementary circuit elements. CDI technology is similar to that of supercapacitors, and the use of electrode impedance models is common in both technologies. A well know equivalent simplyfied electrical circuit is the Randles cell, shown in Figure A.1. The CDI cell is modelled using R_s in series with capacitor (C), in the Randles cell an additional resistance (R_p) is put in parallel with C in order to account for the flow of parasitic current. The effective values of these components can be fit to experimental data. The desalination performance of the cell can then be interpreted based on these values.

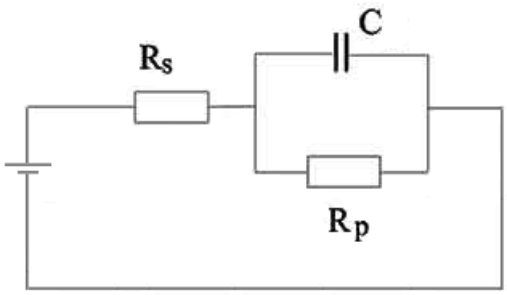

Figure A.1: Electrical circuit of the Randles cell

It is possible to derive a great deal of data from electrochemical impedance spectroscopy (EIS) using this Randles cell. Figure A.2 shows a two-electrode four-wire setup, utilizing an more complicated equivalent electrical circuit, to determine resistances within the CDI cell. EIS uses a sinusoidal voltage input signal over a range of frequencies to determine the phase angle between the input signal and the current as the output signal. The impedance is determined from the output amplitude and phase angle for all same frequencies. With the phase angle and the impedance's a Nyquist can be plotted. From this plot the resistances can be easily extracted without complicated fitting, see Figure A.2 (d).

The impedance of the CDI cell from Figure A.2, can be described by the following equations,

$$Z_{2w} = Z_{EEI} + Z_{4w} \tag{A.1}$$

$$Z_{EEI} = R_{EER,s} + \frac{R_{contact}}{1 + i\omega R_{contact} C_{contact}} \tag{A.2}$$

$$Z_{4w} = R_{IER} + R_{sp} + 2\sqrt{R_{mA} Z_w} coth\left(\sqrt{\frac{R_{mA}}{Z_w}}\right) \tag{A.3}$$

$$Z_w = \left(i\omega C_w + \frac{1}{R_{ct} + Z_{st}}\right)^{-1} \tag{A.4}$$

$$Z_{st} = \frac{R_{st}}{(i\omega\tau_{st})^n} coth[(i\omega\tau_{st})^n], \tag{A.5}$$

$$\tag{A.6}$$

where Z_{2w} and Z_{4w} are the total device impedance measured in two-wire and four-wire measurement modes, Z_{EEI} is the external electronic impedance, $R_{EER,s}$ is the series resistance of the external electronic impedance, $R_{contact}$ is the resistance of the contact between the current collectors and electrodes, $C_{contact}$ is the contact capacitance of the contact, ω is the angular frequency of the applied voltage sine wave, R_{IER} is the internal electronic resistance, R_{sp} is the ionic resistance as in Equation 2.37, R_{mA} is the electrode macropore ionic resistance, Z_w is the macropore wall impedance, Z_{st} is the storage pore impedance, R_{st} is the storage pore resistance, τ_{st} is the storage pore characteristic time, and n is the anomalous diffusion order parameter.

By examining the real-component location of the impedance in Figure A.2, a simple interpretation of the CDI cell can be obtained with resistances that are formulated as

$$R_{4w} = R_{IER} + R_{sp} + 2R_{el} \tag{A.7}$$

$$R_{el} = \frac{l_{el}\tau_{mA}}{3Ap_{mA}} \frac{\kappa + \sigma}{\kappa\sigma} \approx \frac{l_{el}\tau_{mA}}{3Ap_{mA}} \frac{1}{\kappa}, \tag{A.8}$$

where R_{el} is the ionic resistance of one electrode, l_{el} is the thickness of an electrode, τ_{mA} is the tortuosity of the macropore structure, A is the electrode face area, p_{mA} is the electrode macropore porosity and σ is the electrode conductivity.

Adopting the four-wire setup and employing EIS using frequencies from 700 kHz to 40 mHz can help tremendously in identifying CDI functionality.

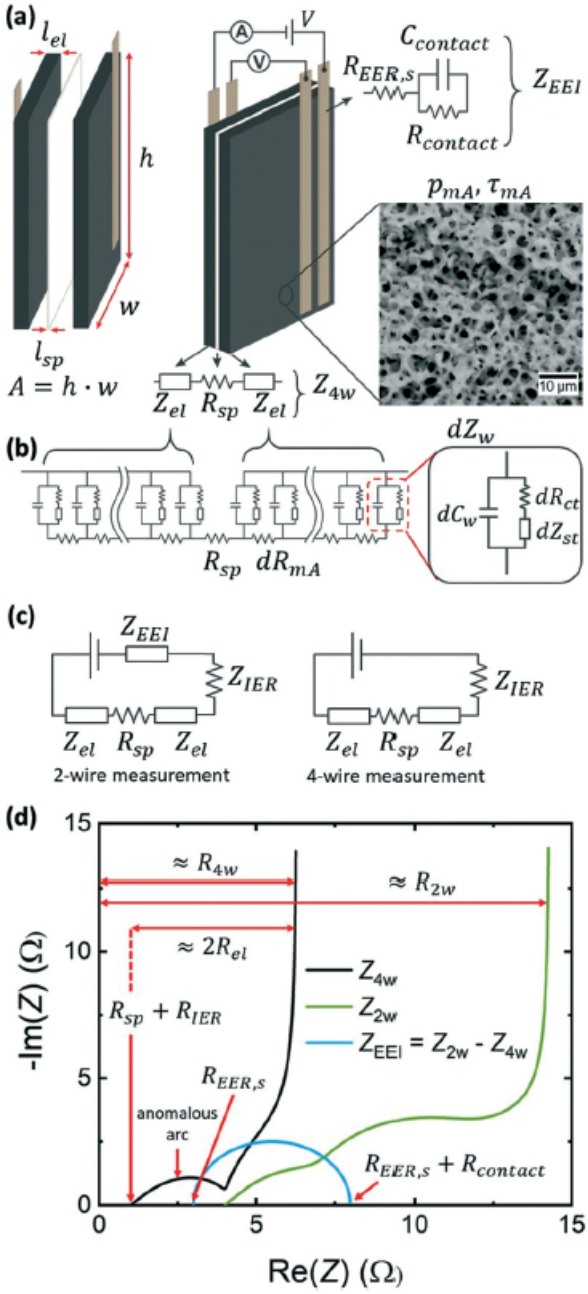

Figure A.2: (a) An individual CDI cell with marked dimensional variables as well as a full cell in a four-wire measurement setup with impedances indicated from Equation A.2 and a SEM image of the electrode material. The activated HCAM material has macropore porosity $p_m A$ and tortuosity τ_{mA}. (b) The nested transmission line circuit model described by Equations A.2 to A.5. (c) The equivalent circuits for the two-wire and four-wire measurement modes of a cell (Equation A.1 and A.3). (d) Representative EIS spectra calculated from Equations A.1 to A.5 with $R_{sp} + R_{EER} = 1\Omega$, $R_{st} = 0.15\Omega$, $C_{st} = 4.5F$, $R_{mA} = 7\Omega$, $R_{ct} = 0.3\Omega$, $C_w = 0.2F$, $n = 0.2$, $R_{EER,s} = 3\Omega$, $R_{contact}5\Omega$, and $C_{contact} = 0.15F$. These values were chosen to present fits of measured spectra. Resistance designations follow from Equations A.7 to A.8.

B

Effect of Flow Rate and Voltage

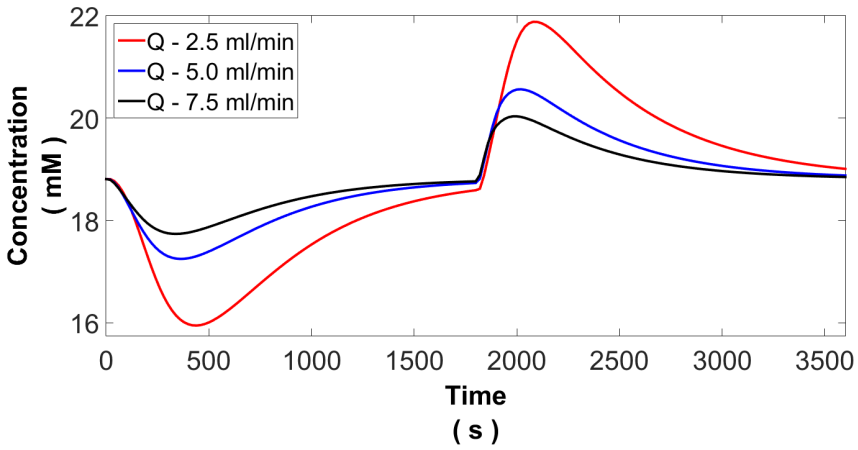

Figure B.1: Effect of flow rate on effluent concentration.

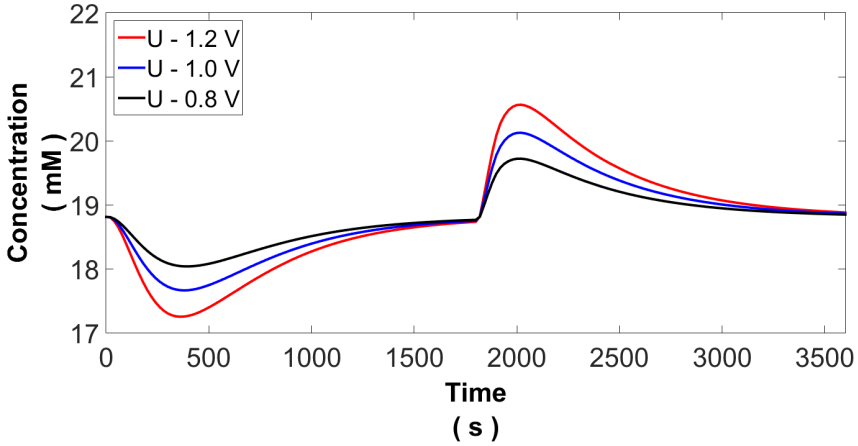

Figure B.2: Effect of applied voltage on effluent concentration.

Bibliography

[1] Md Ashique Ahmed and Sanjay Tewari. Effect of pretreatment of carbon based electrodes in their adsorption performance in capacitive deionization. *World Environmental and Water Resources Congress 2017: International Perspectives, History and Heritage, Emerging Technologies, and Student Papers - Selected Papers from the World Environmental and Water Resources Congress 2017*, (August 2018):221–227, 2017. doi: 10.1061/9780784480595.021.

[2] Md Ashique Ahmed and Sanjay Tewari. Capacitive deionization: Processes, materials and state of the technology. *Journal of Electroanalytical Chemistry*, 813(February):178–192, 2018. ISSN 15726657. doi: 10.1016/j.jelechem.2018.02.024. URL https://doi.org/10.1016/j.jelechem.2018.02.024.

[3] Md Ashique Ahmed and Sanjay Tewari. Capacitive deionization: Processes, materials and state of the technology. *Journal of Electroanalytical Chemistry*, 813(February):178–192, 2018. ISSN 15726657. doi: 10.1016/j.jelechem.2018.02.024. URL https://doi.org/10.1016/j.jelechem.2018.02.024.

[4] Marc A. Anderson, Ana L. Cudero, and Jesus Palma. Capacitive deionization as an electrochemical means of saving energy and delivering clean water. Comparison to present desalination practices: Will it compete? *Electrochimica Acta*, 55(12):3845–3856, 2010. ISSN 00134686. doi: 10.1016/j.electacta.2010.02.012. URL http://dx.doi.org/10.1016/j.electacta.2010.02.012.

[5] Eran Avraham, Malachi Noked, Izaak Cohen, Abraham Soffer, and Doron Aurbach. The Dependence of the Desalination Performance in Capacitive Deionization Processes on the Electrodes PZC. *Journal of The Electrochemical Society*, 158(12):P168, 2011. ISSN 00134651. doi: 10.1149/2.078112jes.

[6] Lydia R. Boktor. Towards the recovery of phosphate using CDI. Technical report, Technical University Delft, 2014.

[7] Yaniv Bouhadana, Eran Avraham, Abraham Soffer, and Doron Aurbach. Several Basic and Practical Aspects Related to Electrochemical Deionzation of Water. *Wiley InterScience*, 2009. doi: 10.1002/aic.12005.

[8] Thomas C. Brown, Vinod Mahat, and Jorge A. Ramirez. Adaptation to Future Water Shortages in the United States Caused by Population Growth and Climate Change. *Earth's Future*, 7(3):219–234, 2019. ISSN 23284277. doi: 10.1029/2018EF001091.

[9] Stephen Brunauer, P. H. Emmett, and Edward Teller. Adsorption of Gases in Multimolecular Layers. *Journal of the American Chemical Society*, 60(2):309–319, 1938. ISSN 15205126. doi: 10.1021/ja01269a023.

[10] Li Min Chang, Xiao Yue Duan, and Wei Liu. Preparation and electrosorption desalination performance of activated carbon electrode with titania. *Desalination*, 270(1-3):285–290, 2011. ISSN 00119164. doi: 10.1016/j.desal.2011.01.008. URL http://dx.doi.org/10.1016/j.desal.2011.01.008.

[11] Zhaolin Chen, Cunyi Song, Xiaowei Sun, Hongfei Guo, and Guangdong Zhu. Kinetic and isotherm studies on the electrosorption of NaCl from aqueous solutions by activated carbon electrodes. *Desalination*, 267(2-3):239–243, 2011. ISSN 00119164. doi: 10.1016/j.desal.2010.09.033. URL http://dx.doi.org/10.1016/j.desal.2010.09.033.

[12] Yutuo Cheng, Zhiqi Hao, Changrun Hao, Yu Deng, Xingying Li, Kexun Li, and Yubo Zhao. A review of modification of carbon electrode material in capacitive deionization. *RSC Advances*, 9(42):24401–24419, 2019. ISSN 20462069. doi: 10.1039/c9ra04426d.

[13] Tatyana Chernova, Fiona A. Murphy, Sara Galavotti, Xiao Ming Sun, Ian R. Powley, Stefano Grosso, Anja Schinwald, Joaquin Zacarias-Cabeza, Kate M. Dudek, David Dinsdale, John Le Quesne, Jonathan Bennett, Apostolos Nakas, Peter Greaves, Craig A. Poland, Ken Donaldson, Martin Bushell, Anne E. Willis, and Marion MacFarlane. Long-Fiber Carbon Nanotubes Replicate Asbestos-Induced Mesothelioma with Disruption of the Tumor Suppressor Gene Cdkn2a (Ink4a/Arf). *Current Biology*, 27(21):3302–3314.e6,

2017. ISSN 09609822. doi: 10.1016/j.cub.2017.09.007. URL https://doi.org/10.1016/j.cub.2017.09.007.

[14] Jae Hwan Choi. Fabrication of a carbon electrode using activated carbon powder and application to the capacitive deionization process. *Separation and Purification Technology*, 70(3):362–366, 2010. ISSN 13835866. doi: 10.1016/j.seppur.2009.10.023.

[15] Jae Hwan Choi. Fabrication of a carbon electrode using activated carbon powder and application to the capacitive deionization process. *Separation and Purification Technology*, 70(3):362–366, 2010. ISSN 13835866. doi: 10.1016/j.seppur.2009.10.023.

[16] Izaak Cohen, Eran Avraham, Yaniv Bouhadana, Abraham Soffer, and Doron Aurbach. Long term stability of capacitive de-ionization processes for water desalination : The challenge of positive electrodes corrosion. *Electrochimica Acta*, 106:91–100, 2013. ISSN 0013-4686. doi: 10.1016/j.electacta.2013.05.029. URL http://dx.doi.org/10.1016/j.electacta.2013.05.029.

[17] J.C. Crittenden, R. R. Trussell, D. W. Hand, K. J. Howe, and G. Tchobanoglous. MWH's Water Treatment: Principles and Design. In *Introduction*, pages 1–16. John Wiley & Sons, Inc., Hoboken, NJ, 3rd edition, 2012.

[18] Edward C. Dillon, John H. Wilton, Jared C. Barlow, and William A. Watson. Large surface area activated charcoal and the inhibition of aspirin absorption. *Annals of Emergency Medicine*, 18(5):547–552, 1989. ISSN 01960644. doi: 10.1016/S0196-0644(89)80841-8.

[19] Juan Galle-Juarez and Karl Graff. *Power Ultrasonics*. Woodhead Publishing, 1st edition, 2014. ISBN 9781782420286.

[20] Li Guan, Linpo Yu, and George Z. Chen. Capacitive and non-capacitive faradaic charge storage. *Electrochimica Acta*, 206(June):464–478, 2016. ISSN 00134686. doi: 10.1016/j.electacta.2016.01.213.

[21] Linchen Han, K. G. Karthikeyan, Marc A. Anderson, and Kelvin B. Gregory. Exploring the impact of pore size distribution on the performance of carbon electrodes for capacitive deionization. *Journal of Colloid and Interface Science*, 430:93–99, 2014. ISSN 10957103. doi: 10.1016/j.jcis.2014.05.015. URL http://dx.doi.org/10.1016/j.jcis.2014.05.015.

[22] Steven A. Hawks, Ashwin Ramachandran, Slawomir Porada, Patrick G. Campbell, Matthew E. Suss, P. M. Biesheuvel, Juan G. Santiago, and Michael Stadermann. Performance metrics for the objective assessment of capacitive deionization systems. *Water Research*, 152:126–137, 2019. ISSN 18792448. doi: 10.1016/j.watres.2018.10.074. URL https://doi.org/10.1016/j.watres.2018.10.074.

[23] Zoha Heidarinejad, Mohammad Hadi Dehghani, Mohsen Heidari, Gholamali Javedan, Imran Ali, and Mika Sillanpää. Methods for preparation and activation of activated carbon: a review. *Environmental Chemistry Letters*, 18(2):393–415, 2020. ISSN 16103661. doi: 10.1007/s10311-019-00955-0. URL https://doi.org/10.1007/s10311-019-00955-0.

[24] Ali Hemmatifar, Michael Stadermann, and Juan G Santiago. Two-Dimensional Porous Electrode Model for Capacitive Deionization. *The Journal Of Physical Chemistry*, 2015. doi: 10.1021/acs.jpcc.5b05847.

[25] Ali Hemmatifar, Ashwin Ramachandran, Kang Liu, Diego I. Oyarzun, Martin Z. Bazant, and Juan G. Santiago. Thermodynamics of Ion Separation by Electrosorption. *Environmental Science and Technology*, 52(17):10196–10204, 2018. ISSN 15205851. doi: 10.1021/acs.est.8b02959.

[26] Chia Hung Hou, Jing Fang Huang, Hong Ren Lin, and Bo Yan Wang. Preparation of activated carbon sheet electrode assisted electrosorption process. *Journal of the Taiwan Institute of Chemical Engineers*, 43(3):473–479, 2012. ISSN 18761070. doi: 10.1016/j.jtice.2011.12.003. URL http://dx.doi.org/10.1016/j.jtice.2011.12.003.

[27] Chia Hung Hou, Nei Ling Liu, Hsin Lan Hsu, and Walter Den. Development of multi-walled carbon nanotube/poly(vinyl alcohol) composite as electrode for capacitive deionization. *Separation and Purification Technology*, 130:7–14, 2014. ISSN 13835866. doi: 10.1016/j.seppur.2014.04.004. URL http://dx.doi.org/10.1016/j.seppur.2014.04.004.

[28] Zheng-hong Huang, Ming Wang, Lei Wang, and Feiyu Kang. Relation between the Charge Efficiency of Activated Carbon Fiber and Its Desalination Performance. 2012. doi: 10.1021/la204690s.

[29] Zheng Hong Huang, Zhiyu Yang, Feiyu Kang, and Michio Inagaki. Carbon electrodes for capacitive deionization. *Journal of Materials Chemistry A*, 5(2):470–496, 2017. ISSN 20507496. doi: 10.1039/c6ta06733f. URL http://dx.doi.org/10.1039/C6TA06733F.

[30] Baoping Jia and Wei Zhang. Preparation and Application of Electrodes in Capacitive Deionization (CDI): a State-of-Art Review. *Nanoscale Research Letters*, 2016. ISSN 1931-7573. doi: 10.1186/s11671-016-1284-1. URL http://dx.doi.org/10.1186/s11671-016-1284-1.

[31] Hae-hyun Jung, Sung-woo Hwang, Sang-hoon Hyun, and Kang-ho Lee. Capacitive deionization characteristics of nanostructured carbon aerogel electrodes synthesized via ambient drying. 216:377–385, 2007. doi: 10.1016/j.desal.2006.11.023.

[32] Aries Keck. When It Comes to Water, You Have to Think Global, 2020. URL https://www.nasa.gov/feature/when-it-comes-to-water-you-have-to-think-global.

[33] Jin Young Kim, Kun Cho, Seul A. Ryu, So Youn Kim, and Byung Mook Weon. Crack formation and prevention in colloidal drops. *Scientific Reports*, 5:1–9, 2015. ISSN 20452322. doi: 10.1038/srep13166.

[34] Taeyoung Kim and Jeyong Yoon. Relationship between capacitance of activated carbon composite electrodes measured at a low electrolyte concentration and their desalination performance in capacitive deionization. *Journal of Electroanalytical Chemistry*, 704:169–174, 2013. ISSN 15726657. doi: 10.1016/j.jelechem.2013.07.003. URL http://dx.doi.org/10.1016/j.jelechem.2013.07.003.

[35] Taeyoung Kim and Jeyong Yoon. Relationship between capacitance of activated carbon composite electrodes measured at a low electrolyte concentration and their desalination performance in capacitive deionization. *Journal of Electroanalytical Chemistry*, 704:169–174, 2013. ISSN 15726657. doi: 10.1016/j.jelechem.2013.07.003. URL http://dx.doi.org/10.1016/j.jelechem.2013.07.003.

[36] Yu Jin Kim and Jae Hwan Choi. Enhanced desalination efficiency in capacitive deionization with an ion-selective membrane. *Separation and Purification Technology*, 71(1):70–75, 2010. ISSN 13835866. doi: 10.1016/j.seppur.2009.10.026.

[37] Alexander Kraytsberg and Yair Ein-Eli. Conveying Advanced Li-ion Battery Materials into Practice The Impact of Electrode Slurry Preparation Skills. *Advanced Energy Materials*, 6(21), 2016. ISSN 16146840. doi: 10.1002/aenm.201600655.

[38] Asvin S. Kumar, Damodhar Ghime, and Prabir Ghosh. Poly(Vinyl Alcohol)-Bonded Carbon Electrodes for Desalination of Brackish Water Using Capacitive Deionization. *Journal of The Institution of Engineers (India): Series E*, 101(2):125–131, 2020. ISSN 22502491. doi: 10.1007/s40034-020-00165-2. URL https://doi.org/10.1007/s40034-020-00165-2.

[39] Bin Lee, Namsoo Park, Kyung Suk Kang, Ho Jin Ryu, and Soon Hyung Hong. Enhanced Capacitive Deionization by Dispersion of CNTs in Activated Carbon Electrode. *ACS Sustainable Chemistry and Engineering*, 6(2):1572–1579, 2018. ISSN 21680485. doi: 10.1021/acssuschemeng.7b01750.

[40] Jaehan Lee, Seoni Kim, Nayeong Kim, Choonsoo Kim, and Jeyong Yoon. Enhancing the desalination performance of capacitive deionization using a layered double hydroxide coated activated carbon electrode. *Applied Sciences (Switzerland)*, 10(1):12–15, 2020. ISSN 20763417. doi: 10.3390/app10010403.

[41] Mingquan Liu, Min Xu, Yifei Xue, Wei Ni, Silu Huo, Linlin Wu, Zhiyu Yang, and Yi Ming Yan. Efficient Capacitive Deionization Using Natural Basswood-Derived, Freestanding, Hierarchically Porous Carbon Electrodes. *ACS Applied Materials and Interfaces*, 10(37):31260–31270, 2018. ISSN 19448252. doi: 10.1021/acsami.8b08232.

[42] Qian Liu, Yue Wang, Yujie Zhang, Shichang Xu, and Jixiao Wang. Effect of dopants on the adsorbing performance of polypyrrole/graphite electrodes for capacitive deionization process. *Synthetic Metals*, 162(7-8):655–661, 2012. ISSN 03796779. doi: 10.1016/j.synthmet.2012.01.015. URL http://dx.doi.org/10.1016/j.synthmet.2012.01.015.

[43] Guoqian Lu, Guowen Wang, Peng Hui Wang, Zhiyu Yang, Huan Yan, Wei Ni, Lin Zhang, and Yi Ming Yan. Enhanced capacitive deionization performance with carbon electrodes prepared with a modified evaporation casting method. *Desalination*, 386:32–38, 2016. ISSN 00119164. doi: 10.1016/j.desal.2016.02.008. URL http://dx.doi.org/10.1016/j.desal.2016.02.008.

[44] Mohamed Mossad and Linda Zou. Study of fouling and scaling in capacitive deionisation by using dissolved organic and inorganic salts. *Journal of Hazardous Materials*, 244-245:387–393, 2013. ISSN 03043894. doi: 10.1016/j.jhazmat.2012.11.062. URL http://dx.doi.org/10.1016/j.jhazmat.2012.11.062.

[45] Mohamed Mossad, Wei Zhang, and Linda Zou. Using capacitive deionisation for inland brackish groundwater desalination in a remote location. *Desalination*, 308(October 2011):154–160, 2013. ISSN 00119164. doi: 10.1016/j.desal.2012.05.021. URL http://dx.doi.org/10.1016/j.desal.2012.05.021.

[46] Jean Philippe Nicot and Ian J. Duncan. Review: Common attributes of hydraulically fractured oil and gas production and CO2 geological sequestration. *Greenhouse Gases: Science and Technology*, 2(5):352–368, 2012. ISSN 21523878. doi: 10.1002/ghg.

[47] NOS Niews. Niet eerder zo droog in deze tijd van het jaar, watertekort dreigt, 2020. URL https://nos.nl/artikel/2335308-niet-eerder-zo-droog-in-deze-tijd-van-het-jaar-watertekort-dreigt.html.

[48] Taikan Oki and Shinjiro Kanae. Global hydrological cycles and world water resources. *Science*, 313(5790):1068–1072, 2006. ISSN 00368075. doi: 10.1126/science.1128845.

[49] Charlie O'Mahony, Ehtsham Ul Haq, Christophe Sillien, and Syed A.M. Tofail. Rheological issues in carbon-based inks for additive manufacturing, 2019. ISSN 2072666X.

[50] Craig A. Poland, Rodger Duffin, Ian Kinloch, Andrew Maynard, William A.H. Wallace, Anthony Seaton, Vicki Stone, Simon Brown, William MacNee, and Ken Donaldson. Carbon nanotubes introduced into the abdominal cavity of mice show asbestos-like pathogenicity in a pilot study. *Nature Nanotechnology*, 3(7):423–428, 2008. ISSN 17483395. doi: 10.1038/nnano.2008.111.

[51] S. Porada, M. Bryjak, A. Van Der Wal, and P. M. Biesheuvel. Effect of electrode thickness variation on operation of capacitive deionization. *Electrochimica Acta*, 75:148–156, 2012. ISSN 00134686. doi: 10.1016/j.electacta.2012.04.083.

[52] S. Porada, L. Borchardt, M. Oschatz, M. Bryjak, J. S. Atchison, K. J. Keesman, S. Kaskel, P. M. Biesheuvel, and V. Presser. Direct prediction of the desalination performance of porous carbon electrodes for capacitive deionization. *Energy and Environmental Science*, 6(12):3700–3712, 2013. ISSN 17545692. doi: 10.1039/c3ee42209g.

[53] S. Porada, R. Zhao, A. Van Der Wal, V. Presser, and P. M. Biesheuvel. Review on the science and technology of water desalination by capacitive deionization. *Progress in Materials Science*, 58(8):1388–1442, 2013. ISSN 00796425. doi: 10.1016/j.pmatsci.2013.03.005. URL http://dx.doi.org/10.1016/j.pmatsci.2013.03.005.

[54] Min Woong Ryoo and Gon Seo. Improvement in capacitive deionization function of activated carbon cloth by titania modification. *Water Research*, 37(7):1527–1534, 2003. ISSN 00431354. doi: 10.1016/S0043-1354(02)00531-6.

[55] Soshi Shiraishi. *Electrochemical Performance*. Tsinghua University Press Limited, 2016. ISBN 9780128052563. doi: 10.1016/b978-0-12-805256-3.00010-6. URL http://dx.doi.org/10.1016/B978-0-12-805256-3.00010-6.

[56] K. S. Spiegler and Y. M. El-Sayed. The energetics of desalination processes. *Desalination*, 134(1-3):109–128, 2001. ISSN 00119164. doi: 10.1016/S0011-9164(01)00121-7.

[57] Zhuyin Sui, Qinghan Meng, Xuetong Zhang, Rui Ma, and Bing Cao. Green synthesis of carbon nanotube-graphene hybrid aerogels and their use as versatile agent for water purification. *J. Mater. Chem.*, 22:8767–8771, 2012. doi: 10.1039/c2jm0005e.

[58] M. E. Suss, S. Porada, X. Sun, P. M. Biesheuvel, J. Yoon, and V. Presser. Water desalination via capacitive deionization: What is it and what can we expect from it? *Energy and Environmental Science*, 8(8):2296–2319, 2015. ISSN 17545706. doi: 10.1039/c5ee00519a.

[59] Matthew E. Suss, Theodore F. Baumann, William L. Bourcier, Christopher M. Spadaccini, Klint A. Rose, Juan G. Santiago, and Michael Stadermann. Capacitive desalination with flow-through electrodes. *Energy and Environmental Science*, 5(11):9511–9519, 2012. ISSN 17545692. doi: 10.1039/c2ee21498a.

[60] United Nations. Clean water and sanitation: Why it Matters, 2016.

[61] Nikolay Voutchkov. Desalination Engineering, Planning and Design. In *Desalination Engineering: An Overview*, chapter 1, pages 1–16. The McGraw-Hill Companies, Inc., 2013. ISBN 978-0-07-177715-5.

[62] Li Wang and Shihong Lin. Membrane Capacitive Deionization with Constant Current vs Constant Voltage Charging: Which Is Better? *Environmental Science and Technology*, 52(7):4051–4060, 2018. ISSN 15205851. doi: 10.1021/acs.est.7b06064.

[63] Shuo Wang, Da Zhi Wang, Li Jun Ji, Qianming Gong, Yue Feng Zhu, and Ji Liang. Equilibrium and kinetic studies on the removal of NaCl from aqueous solutions by electrosorption on carbon nanotube electrodes. *Separation and Purification Technology*, 58(1):12–16, 2007. ISSN 13835866. doi: 10.1016/j.seppur.2007.07.005.

[64] Lawrence Weinstein and Ranjan Dash. Capacitive Deionization: Challenges and Opportunities. *Desalination & Water Reuse*, pages 34–37, 2013.

[65] WHO. *Guidelines for Drinking-water Quality*. 4th edition, 2016. ISBN 9789241549950.

[66] Jessie Yeung, Swati Gupta, and Michael Guy. India has just five years to solve its water crisis, experts fear. Otherwise hundreds of millions of lives will be in danger, 2019. URL `https://edition.cnn.com/2019/06/27/india/india-water-crisis-intl-hnk/index.html`.

[67] Tung-yu Ying, Kun-lin Yang, Sotira Yiacoumi, and Costas Tsouris. Electrosorption of Ions from Aqueous Solutions by Nanostructured Carbon Aerogel. 27(2002):18–27, 2008. doi: 10.1006/jcis.2002.8314.

[68] Changyong Zhang, Di He, Jinxing Ma, Wangwang Tang, and T. David Waite. Faradaic reactions in capacitive deionization (CDI) - problems and possibilities: A review. *Water Research*, 128:314–330, 2018. ISSN 18792448. doi: 10.1016/j.watres.2017.10.024.

[69] Yingjie Zhang, Jia Guo, and Ting Li. Research progress on binder of activated carbon electrode. *Advanced Materials Research*, 549:780–784, 2012. ISSN 10226680. doi: 10.4028/www.scientific.net/AMR.549.780.

[70] Honghe Zheng, Li Zhang, Gao Liu, Xiangyun Song, and Vincent S. Battaglia. Correlationship between electrode mechanics and long-term cycling performance for graphite anode in lithium ion cells. *Journal of Power Sources*, 217:530–537, 2012. ISSN 03787753. doi: 10.1016/j.jpowsour.2012.06.045. URL `http://dx.doi.org/10.1016/j.jpowsour.2012.06.045`.

[71] Zhentao Zhu, Shuihua Tang, Jiawei Yuan, Xiaolong Qin, Yuxiao Deng, Renjie Qu, and Geir Martin Haarberg. Effects of various binders on supercapacitor performances. *International Journal of Electrochemical Science*, 11(10):8270–8279, 2016. ISSN 14523981. doi: 10.20964/2016.10.04.

[72] Linda Zou, Lixia Li, Huaihe Song, and Gayle Morris. Using mesoporous carbon electrodes for brackish water desalination. *Water Research*, 42(8-9):2340–2348, 2008. ISSN 00431354. doi: 10.1016/j.watres.2007.12.022.

[73] Linda Zou, Gayle Morris, and Daoduo Qi. Using activated carbon electrode in electrosorptive deionisation of brackish water. *Desalination*, 225(1-3):329–340, 2008. ISSN 00119164. doi: 10.1016/j.desal.2007.07.014.